HOKKAIDO UNIVERSITY

Title	Study on Thermal Stability of Thermoelectric Ba1/3CoO2 Thin Films
Author(s)	姜, 炅完
Degree Grantor	北海道大学
Degree Name	博士(工学)
Dissertation Number	甲第17044号
Issue Date	2026-06-30
DOI	https://doi.org/10.14943/doctoral.k17044
Doc URL	https://hdl.handle.net/2115/100097
Type	doctoral thesis
File Information	Kungwan_Kang.pdf, 全文

Hokkaido University Collection of Scholarly and Academic Papers : HUSCAP

Study on Thermal Stability of Thermoelectric $Ba_{1/3}CoO_2$ Thin Films

熱電 $Ba_{1/3}CoO_2$ 薄膜の熱安定性に関する研究

KUNGWAN KANG

Graduate School of Information Science and Technology

Hokkaido University

June. 2026

Table of Contents

Chapter 1. General introduction 1

1.1. Background of thermoelectric energy conversion 1

1.2. Development and challenges of thermoelectric materials 8

1.2.1. Oxide thermoelectric 10

1.3. Layered cobalt oxides 12

1.3.1. Epitaxial A_xCoO_2 (A_x = $Na_{3/4}$, $Ca_{1/3}$, $Sr_{1/3}$ and $Ba_{1/3}$) thin films 15

1.3.2. Epitaxial $Ba_{1/3}CoO_2$ thin films 18

1.3.3. Practical consideration for $Ba_{1/3}CoO_2$ 22

1.4. Objective of This Study 25

References 28

Chapter 2. Experimental procedures 37

2.1. Thin film fabrication 37

2.1.1. Pulsed Laser Deposition (PLD) 38

2.1.2. Direct Current (DC) Sputtering 41

2.2. Crystallographic analysis 42

2.2.1. X-ray diffraction (XRD) 42

2.2.2. Scanning Transmission Electron Microscopy (STEM) 45

2.2.3. Electron Energy Loss Spectroscopy (EELS) 48

2.3. Electrical transport properties 50

2.3.1. Electrical conductivity 50

2.3.2. Thermopower 52

2.4. Thermal conductivity 53

2.4.1. AC calorimetric measurement 53

2.4.2. Time-domain thermoreflectance (TDTR) 55

References 58

Chapter 3. Freestanding $Ba_{1/3}CoO_2$ Single-Crystalline Films: Fabrication and Thermoelectric Properties 59

3.1. Objective of this chapter 59

3.2. Experimental 60

3.3. Result and discussion 64

3.4. Conclusion 74

References 76

Chapter 4. High-Temperature Decomposition Behavior and Its Impact on Electron Transport in $Ba_{1/3}CoO_2$ 78

4.1. Objective of this chapter 78

4.2. Experimental 82

4.3. Result and discussion 83

4.4. Conclusion 106

Reference 107

Chapter 5. Summary 110

Acknowledgement 112

List of Publications 115

Publications related to this thesis 115

Other publications 115

List of Presentations 116

List of Awards 120

Chapter 1. General introduction

1.1. Background of thermoelectric energy conversion

Securing sustainable and reliable energy sources has been a persistent challenge since the Industrial Revolution. Although global energy consumption has increased dramatically with industrialization, a significant portion of primary energy, often exceeding two-thirds, is ultimately dissipated as waste heat during power generation, transportation, and industrial processing. The ability to directly convert this unused thermal energy into electricity would therefore provide an attractive route to improving overall energy efficiency and reducing greenhouse gas emissions. Thermoelectric (TE) materials, which enable solid-state heat-to-electricity conversion without moving parts, have emerged as one of the most promising candidates for waste-heat recovery and distributed power generation.[1-2] Their operation is based on three fundamental thermoelectric effects: the Seebeck, Peltier, and Thomson effects. Among these, the Seebeck effect serves as the primary mechanism for power generation.

The Seebeck effect was first reported by T. J. Seebeck in 1821[3], who observed that a conductor with two ends maintained at different temperatures develops an electric potential difference. When a temperature gradient is applied across a material, charge carriers at the hot side gain higher thermal energy and diffuse toward the cold side. As

shown in **Figure. 1-1**, holes in the p-type leg migrate upward (from hot to cold), while electrons in the n-type leg show the opposite drift direction. This carrier diffusion generates an electrochemical potential difference between the two ends of the material. When an external circuit is connected, this potential drives an electric current, enabling the direct conversion of heat into electrical power. The proportionality between the induced voltage (ΔV) and temperature difference (ΔT) defines the thermopower (≡ Seebeck coefficient),

$$S = \frac{\Delta V}{\Delta T} \tag{1.1}$$

and has the unit of V/K (often expressed in μV/K). Although the Seebeck effect is the primary mechanism for thermoelectric power generation, it is intimately related to two

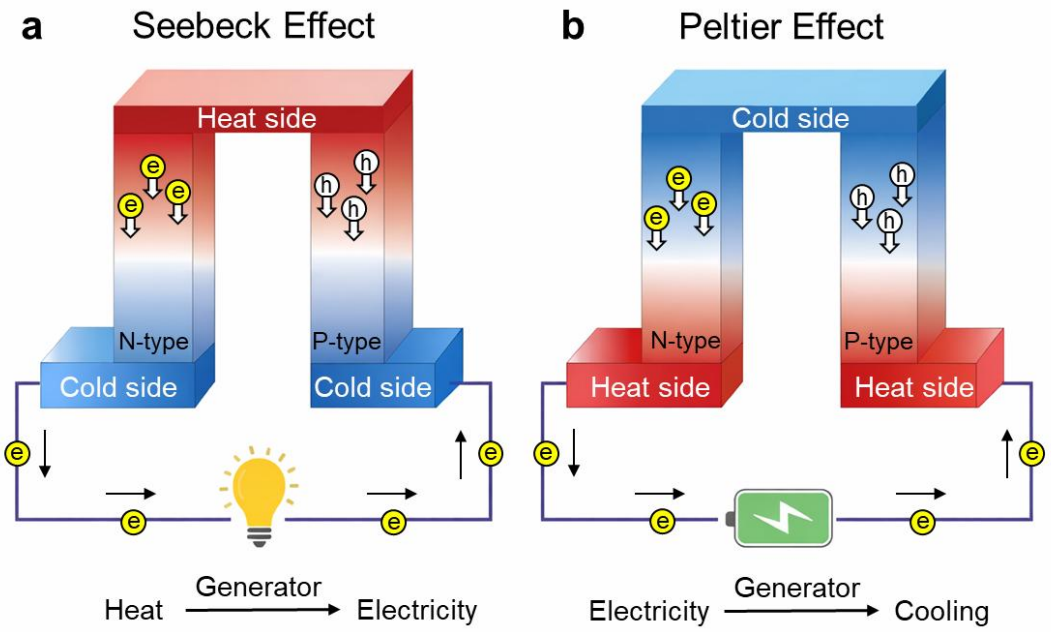

Figure 1-1. Schematic illustrations of (a) Seebeck effect and (b) Pielter effect.

additional thermoelectric transport phenomena: the Peltier effect and the Thomson effect. Together, these three effects describe the complete coupling between heat and charge transport in conductive materials.

In 1834, J. C. A. Peltier discovered that when an electric current passes through a junction between two different conductors, heat is either absorbed or released at the junction. This phenomenon, known as the Peltier effect, is essentially the reverse process of the Seebeck effect. The heat absorbed or emitted at a junction per unit electric current is quantified by the Peltier coefficient Π:

$$\Pi = \frac{q}{I} \tag{1.2}$$

where q is the heating or cooling rate and I is the applied current. Physically, Π corresponds to the amount of heat carried per unit charge as carriers cross a material boundary. In the context of **Figure. 1-1**, reversing the current direction causes electrons and holes to move in the opposite directions compared with the Seebeck configuration, resulting in active heating at one junction and cooling at the other principle widely used in solid-state thermoelectric coolers. Importantly, the Seebeck and Peltier coefficients are not independent. Thermodynamics imposes the Kelvin relation:

$$\Pi = S \cdot T \tag{1.3}$$

which indicates that a material with a large S also exhibits a large Peltier heat transport at temperature T. Thus, the two effects are different manifestations of the same underlying coupling between charge and heat flow.

Although the Seebeck effect and the Peltier effect can both be defined within a single material, they were historically observed in circuits composed of two different conductors. However, even in a homogeneous semiconductor or metal, if an electric current flows through a region where a temperature gradient exists, additional heat absorption or release occurs continuously along the conduction path. This arises because the S is temperature dependent, and therefore the local Peltier effect varies continuously along the material. This phenomenon was first identified by William Thomson in 1854 and is now referred to as the Thomson effect. The heating or cooling rate associated with the Thomson effect can be expressed as

$$q = \tau_T \cdot I \cdot \Delta T \tag{1.4}$$

where τ_{T} is the Thomson coefficient, I is the electric current, and ΔT is the temperature difference along the current path.

The maximum power conversion efficiency of a thermoelectric generator operating between a hot-side temperature T_H and cold-side temperature T_L is expressed as

$$\eta_{max} = \frac{T_{\mathrm{H}} - T_{\mathrm{L}}}{T_{\mathrm{H}}} \cdot \frac{\sqrt{1 + ZT_{avg}} - 1}{\sqrt{1 + ZT_{avg}} + T_L/T_H} \tag{1.5}$$

where ZT_{avg} is the dimensionless thermoelectric figure of merit averaged over the operating temperature range. This expression indicates that the efficiency increases monotonically with both the temperature difference and the material's intrinsic ZT. For a given application, thermal stability constraints usually fix the operating temperature window, so maximizing ZT becomes the primary design objective.

The figure of merit *ZT* is defined as

$$ZT = \frac{S^2 \cdot \sigma \cdot T}{\kappa} \tag{1.6}$$

where *S* is the thermopower, σ is the electrical conductivity, *T* is the absolute temperature, and κ is the total thermal conductivity. The numerator $S^2\sigma$ is known as the power factor (PF). A high PF indicates that the material can produce a large voltage (large *S*) while maintaining high electrical current (large σ). Meanwhile, low thermal conductivity is required to maintain a strong temperature gradient across the material. Thus, high-performance thermoelectric materials must simultaneously achieve large *S*, high σ, and low κ, a combination that is difficult to realize because of the intrinsic coupling among transport parameters. For degenerate semiconductors and metals, the *S* can be approximated by the Mott equation[4]

$$S = \frac{\pi^2 \cdot {k_B}^2 T}{3e}\left[\frac{d\ln[\sigma(E)]}{dE}\right]_{E=E_F} = \frac{\pi^2}{3}\frac{{k_B}^2 T}{e}\left\{\frac{1}{n}\cdot\frac{dn(E)}{dE} + \frac{1}{\mu}\cdot\frac{d\mu(E)}{dE}\right\}_{E=E_F} \tag{1.7}$$

where k_B is the Boltzmann constant, *e* is the electron charge, *n* is the carrier concentration, E_F is the Fermi energy, and μ is the carrier mobility. Because σ(E) is proportional to n(E)·μ(E), Eq. (1.7) indicates that the magnitude of *S* is determined by the energy dependence of the electronic structure near the Fermi level. Features such as band curvature, density of states (DOS), and scattering mechanisms govern how rapidly σ(E) changes with energy. Sharp variations in the DOS, narrow electronic bands, or resonance levels can therefore lead to enhanced thermopower.

The Mott relation also provides a microscopic basis for understanding how transport properties evolve with carrier concentration. As n increases, the Fermi level shifts deeper into the electronic band where the DOS becomes less energy dependent. This reduces the slope term in Eq. (1.7) and consequently decreases S. In contrast, electrical conductivity increases because $\sigma = n \cdot e \cdot \mu$. These competing tendencies give rise to the well-known S–σ trade-off, which limits simultaneous enhancement of thermopower and conductivity in many thermoelectric systems.

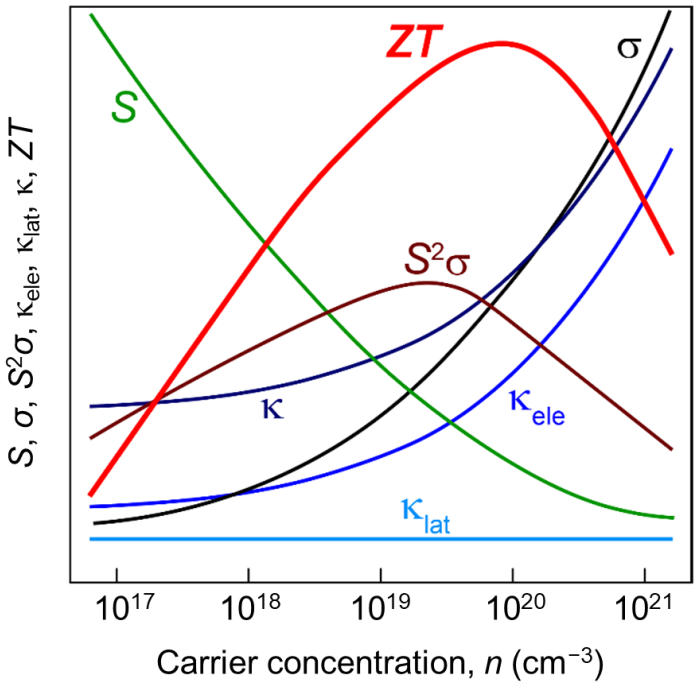

Figure 1-2. Schematic of relationship between ZT, thermopower (S), electrical conductivity (σ), power factor ($S^2 \cdot \sigma$) and thermal conductivity [κ, sum of electron thermal conductivity (κ_{ele}) and lattice thermal conductivity (κ_{lat})].

The macroscopic consequences of this trade-off are illustrated in **Figure. 1-2.** The thermopower decreases monotonically with increasing carrier concentration, whereas the

electrical conductivity increases. As a result, the power factor $S^2\sigma$exhibits a maximum at an intermediate carrier concentration where neither S nor σ dominates the transport behavior. Thermal conductivity κ also varies with carrier concentration n and consists of two distinct components: the lattice thermal conductivity κ_{lat}, which originates from phonon transport, and the electronic thermal conductivity κ_{ele}, which arises from charge carrier heat transport. While κ_{lat} is primarily governed by phonon scattering processes and is only weakly dependent on n, κ_{ele} increases with carrier concentration according to the Wiedemann–Franz law[5].

$$\kappa_{ele} = L \cdot \sigma \cdot T = L \cdot n \cdot e \cdot \mu \cdot T \quad (1.8)$$

As n increases, the rise in κ_{ele} partially offsets any benefit gained from the enhanced electrical conductivity, and this interplay has a direct influence on the achievable thermoelectric performance. By combining the contributions of κ_{lat} and κ_{ele}, the figure of merit ZT reaches its maximum near the carrier concentration that optimizes the power factor while ensuring that the increase in κ_{ele} remains limited. For many thermoelectric materials, this optimum falls within the range of 10^{19} to 10^{21} cm^{-3}, although the precise value depends on the electronic structure and phonon scattering characteristics of the specific system.

Because ZT is inversely proportional to κ, reducing thermal conductivity is critically important for enhancing thermoelectric performance. In particular, κ_{lat} represents the dominant portion of κ in many semiconducting thermoelectrics and is relatively

insensitive to carrier concentration. As a result, most modern thermoelectric research focuses on strategies that simultaneously increase the power factor and suppress κ_{lat} through phonon engineering, defect introduction, nanostructuring, and other lattice-level design approaches.

1.2. Development and challenges of thermoelectric materials

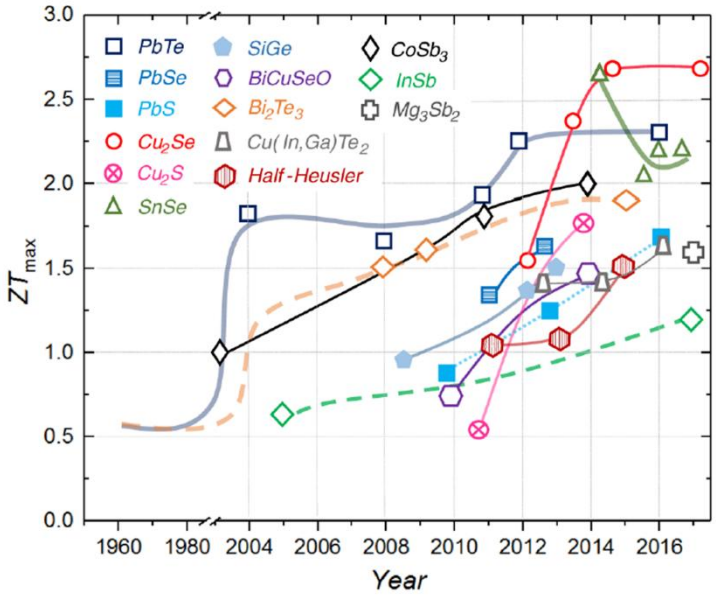

Figure 1-3. Historical evolution of the maximum figure of merit (ZT_{max}) reported for representative thermoelectric material families[6]. PbTe[7-11], PbSe[12-13], PbS[14-16], Cu_2Se[17-20], Cu_2S[21-22], SnSe[23-26], Mg_3Sb_2[27], SiGe, BiCuSeO[28-29], Bi_2Te_3[30-32], $Cu(In,Ga)Te_2$[33-35], $CoSb_3$[36-38], InSb[39-40], and half-Heusler compounds[41-43].

Thermoelectric materials have attracted sustained interest due to their potential for converting waste heat into useful electrical energy. Practical thermoelectric devices have traditionally relied on well-established compounds such as Bi_2Te_3 and PbTe, whose typical *ZT* values are close to 1[44-45]. A *ZT* of approximately 1 has long been regarded as

the minimum threshold for viable commercial applications.[45] Considerable research efforts have therefore focused on enhancing thermoelectric performance, and the progress achieved over the past several decades is summarized in **Figure. 1-3**.[6]

Conventional Bi_2Te_3 and PbTe-based compounds continue to play a central role in thermoelectric research because they provide reliable benchmarks for understanding charge and heat transport mechanisms.[7-11,30-32] However, the low abundance and high toxicity of elements such as Pb and Te have raised increasing concerns regarding environmental impact, long-term safety, and scalability. As a result, there is a growing demand for thermoelectric materials that exhibit comparable or superior performance while being composed of earth-abundant and non-toxic elements.

In response to these challenges, many alternative material systems have been investigated, including MgAgSb-based alloys[46], skutterudites[37,47], and various Cu/Sn chalcogenides[17,22-26,48]. Among these, single-crystalline SnSe has drawn significant attention due to its record-high *ZT* values of approximately 2.6 for p-type and 2.8 for n-type compositions[23,49], which are attributed to its extremely low lattice thermal conductivity and highly anisotropic layered structure.

Despite these breakthroughs, most thermoelectric devices are intended for use at elevated temperatures (≥ 500 °C), where many high-performance chalcogenides encounter critical

limitations. These materials often suffer from decomposition, volatilization, or melting under high-temperature operating conditions, which compromises device stability and reliability. Consequently, the long-term practical applicability of many high-*ZT* chalcogenides remains a subject of ongoing debate. These limitations highlight the need to explore alternative thermoelectric materials that can maintain structural and chemical stability while offering competitive performance. In this context, we direct our attention to rare-earth-free oxide thermoelectric materials, which are intrinsically stable under oxidizing and high-temperature environments and therefore represent a promising platform for reliable thermoelectric energy conversion.

1.2.1. Oxide thermoelectric

The limitations of conventional chalcogenide-based thermoelectrics, particularly their instability under oxidizing and high-temperature environments, have prompted the exploration of alternative material systems capable of sustaining long-term operation. Oxide thermoelectric materials have therefore attracted increasing attention due to their intrinsic thermal robustness, chemical stability in air, and the use of abundant and environmentally benign elements.[50-52] These characteristics make oxides a promising platform for thermoelectric applications in harsh industrial environments where conventional chalcogenides tend to degrade.

Oxides emerged as a promising class of thermoelectric materials owing to their intrinsic robustness, thermal and chemical stability in air, and absence of toxic or scarce elements.

Research on oxide thermoelectrics has a long history. During the first research boom in the 1950s–1970s, thermoelectric measurements of simple conducting oxides such as CdO[53], ZnO[54], In_2O_3[55], $SrTiO_3$[56], TiO_2[57], and Cu_2O[58] were performed to understand their electronic properties. A second surge of interest occurred in the late 1980s, associated with the discovery of high T_c superconducting oxide, where thermopower measurements were widely used to probe charge dynamics.[59-62] The modern era of oxide thermoelectrics began with seminal reports in the mid-1990s demonstrating unexpectedly large thermopower and reasonable electrical conductivity in $CaMnO_3$[63], Al-doped ZnO[64], and particularly Na_xCoO_2[65]. These discoveries triggered a global effort to identify high-*ZT* oxides capable of operating reliably at elevated temperatures.

Despite these advances, the thermoelectric performance of oxides generally lags behind that of state-of-the-art chalcogenides. Their relatively large lattice thermal conductivity, strong ionicity, and wide electronic band gaps impose fundamental constraints on both the power factor and the achievable *ZT*. Nevertheless, several oxide families, including layered cobalt oxides, $Ca_3Co_4O_9$ misfit layered compounds[66-67], and electron-doped $SrTiO_3$[68-70], have demonstrated *ZT* values approaching or exceeding 0.5 at high temperatures. Among them, layered cobalt oxides have been recognized as particularly promising due to their unusual electronic structure that supports simultaneously high electrical conductivity and large thermopower.

1.3. Layered cobalt oxides

Layered cobalt oxides represent one of the most promising families of p-type thermoelectric oxides because they combine unusually large thermopower with relatively high electrical conductivity.[71] The significant breakthrough in this field began with the report by Terasaki et al., who demonstrated that single-crystalline $Na_{3/4}CoO_2$ exhibits an exceptionally large thermopower of approximately 100 μV K^{-1} at 300 K together with a low resistivity of 0.2 mΩ·cm.[65] Soon after, Masset et al. showed that $Ca_3Co_4O_9$ has similar thermoelectric characteristics, further establishing layered cobaltites as key materials in oxide thermoelectrics.[66]

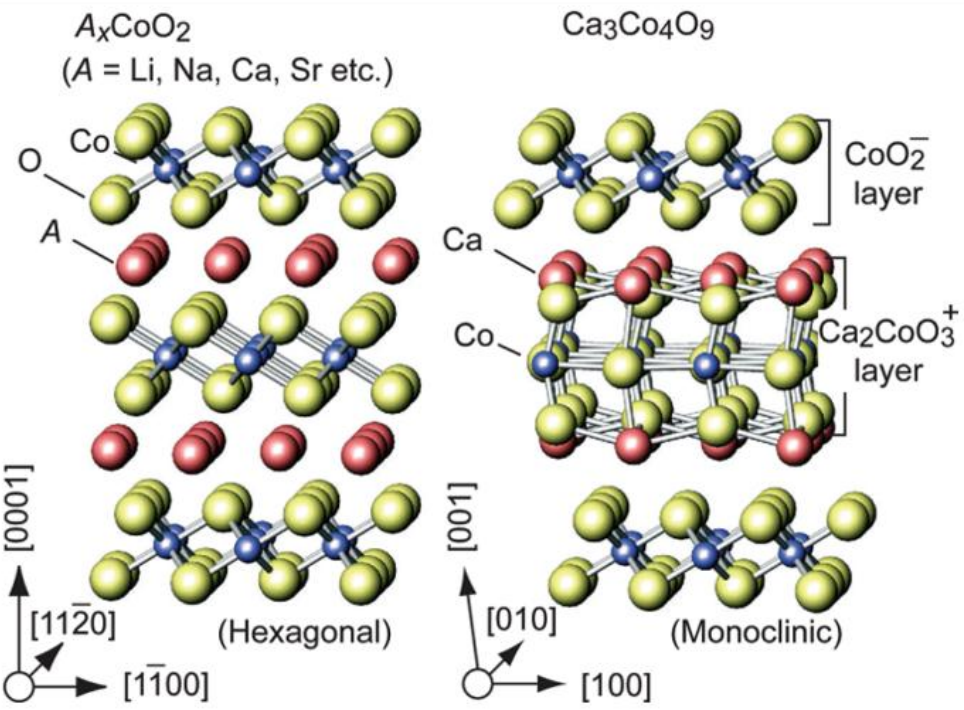

Figure 1-4. Schematic illustrations of crystal structure of $Na_{3/4}CoO_2$ and $Ca_3Co_4O_9$[72]

The crystal structures of these layered cobalt oxides are shown in **Figure. 1-4**[72]. In A_xCoO_2 compounds (A = Li, Na, Ca, Sr, etc.), the structure consists of alternately stacked sheets of A-site cations and electronically active CoO_2 layers arranged in a hexagonal framework. In contrast, $Ca_3Co_4O_9$ adopts a monoclinic misfit structure composed of conductive CoO_2 layers interleaved with Ca_2CoO_3 blocks. In both cases, the two-dimensional CoO_2 layers provide efficient pathways for hole transport, while the layered architecture enhances phonon scattering and helps suppress lattice thermal conductivity. This combination of electronic and structural features enables these materials to achieve promising thermoelectric performance at elevated temperatures.

The unusually large thermopower observed in layered cobalt oxides has been a central topic in understanding their promising thermoelectric properties.[73-74] A key theoretical contribution was made by Koshibae et al., who demonstrated that the large thermopower originates from the low-spin electronic configuration of Co ions in the CoO_2 layers. In $Na_{3/4}CoO_2$, the formal valence states of Na^+ and O^{2-} require equal proportions of Co^{3+} and Co^{4+} to maintain charge neutrality.[73] As illustrated in **Figure. 1-5**, both Co^{3+} and Co^{4+} adopt low-spin states, but their electronic degeneracies differ significantly. Co^{3+} has no degeneracy, whereas Co^{4+} possesses sixfold degeneracy that reflects the available t_{2g} orbitals and spin degrees of freedom. Koshibae et al. described this behavior using an extended Heikes formula:

$$S = \frac{k_B}{C} \ln \left(\frac{g_A}{g_B}\right) \frac{p}{1-p} \tag{1.9}$$

where g_A and g_B represent the degeneracies of Co^{3+} and Co^{4+}, C is their charge difference, and p is the concentration of Co^{4+}. For $Na_{3/4}CoO_2$, $p = 0.5$, which allows the equation to be simplified to

$$S = \frac{k_B}{C} \ln \left(\frac{g_{Co^{3+}}}{g_{Co^{4+}}}\right) \tag{1.10}$$

This gives a thermopower of approximately 150 μV K^{-1}, which is very close to the experimentally measured values at high temperatures. This theoretical prediction was later confirmed by Yayu Wang et al., establishing the spin-entropy mechanism as the fundamental origin of the large thermopower in layered cobaltites.[75] In this mechanism, a hole on a Co^{4+} site carries both electric charge and a substantial amount of entropy, which directly enhances thermopower. The combination of strong electronic correlations, low-spin Co valence states, and the two-dimensional electronic structure of the CoO_2 layers provides a robust explanation for the large thermopower in A_xCoO_2.

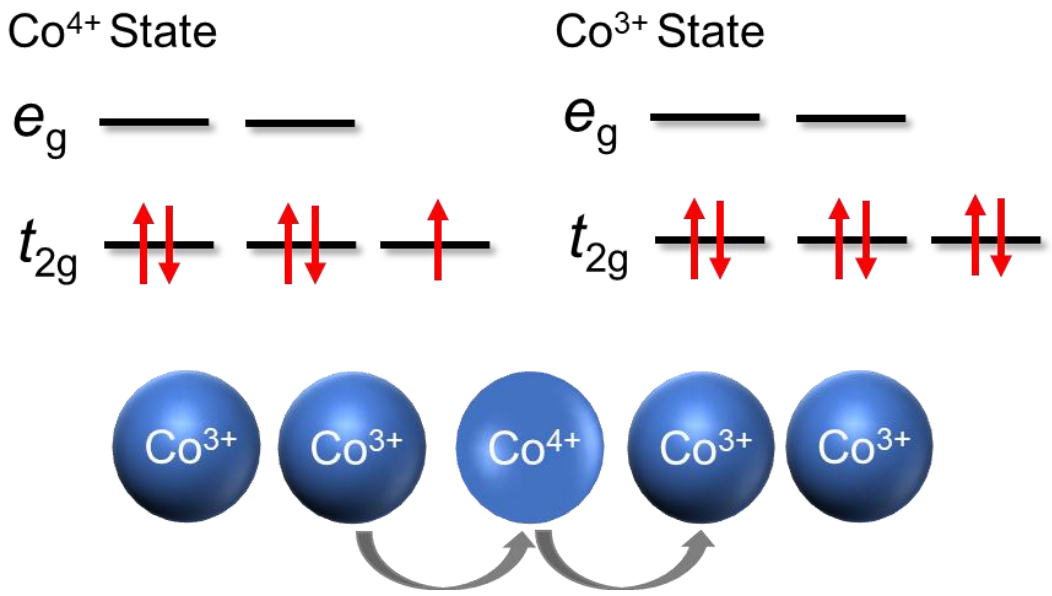

Figure 1-5. Schematic illustrations of mechanism of large thermopower in $NaCo_2O_4$

1.3.1. Epitaxial A_xCoO_2 (A_x = $Na_{3/4}$, $Ca_{1/3}$, $Sr_{1/3}$ and $Ba_{1/3}$) thin films

Our research group has focused on layered cobalt oxides of the A_xCoO_2 family as promising oxide thermoelectric materials. A_xCoO_2 compounds consist of alternately stacked electronically active CoO_2 layers and A-site ion layers, where charge transport is primarily governed by the CoO_2 layers, while the A-site ions mainly influence lattice dynamics and thermal transport. Owing to this structural separation, A_xCoO_2 provides an ideal platform for selectively reducing thermal conductivity without significantly degrading electrical transport properties.

Among layered cobalt oxides, $Na_{3/4}CoO_2$ has been reported to exhibit a high in-plane power factor of approximately 1.02 mW m^{-1} K^{-1}. However, its relatively high thermal conductivity of about 6.79 W m^{-1} K^{-1} limits the room-temperature *ZT* value to approximately 0.04.[76] This indicates that further enhancement of thermoelectric performance in A_xCoO_2 critically depends on suppressing thermal conductivity. In 2013, the research group led by D. J. Voneshen proposed a rattling model in Na_xCoO_2, demonstrating that sodium vacancies can enhance electron–phonon scattering and thereby reduce thermal conductivity.[77] This rattling mechanism strongly suggests that thermal transport in layered cobalt oxides can be effectively controlled through A-site ion substitution, providing a rational strategy for thermoelectric optimization.

To evaluate intrinsic and reliable thermoelectric properties free from extrinsic effects such as grain boundaries, our group investigated high-quality single-crystalline epitaxial thin films. Starting from $Na_{3/4}CoO_2$ epitaxial films, Na ions were systematically exchanged with Li, Ca, and Sr ions via ion-exchange reactions.[78] The thermal conductivity of these films was then measured using the time-domain thermoreflectance (TDTR) technique, as summarized in **Figure 1-6**. The experimental results revealed that the thermal conductivity of A_xCoO_2 decreases monotonically with increasing atomic mass of the A-site ion (**Figure 1-6a**). Heavier A-site ions suppress lattice vibrations and enhance phonon scattering, which is considered to be the primary origin of the reduced lattice thermal conductivity (**Figure 1-6 b** and **c**).[78]

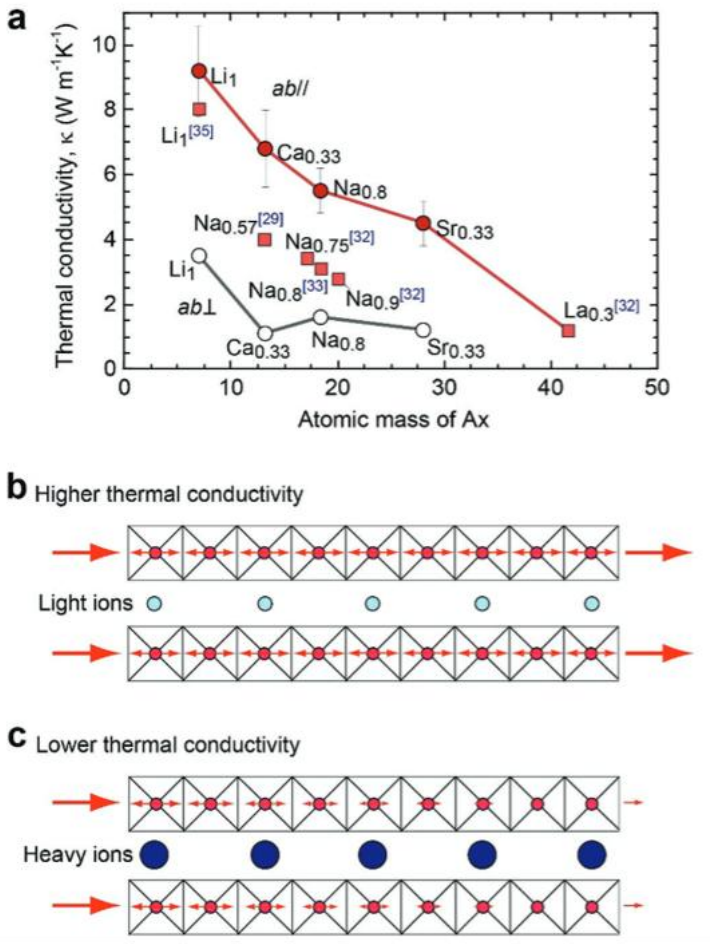

Figure 1-6. (a) Dependence of the in-plane thermal conductivity κ of epitaxial A_xCoO_2 thin films on the atomic mass of the A-site ion, showing a monotonic decrease in κ with increasing A-site atomic mass. (b, c) Schematic illustrations of phonon transport in A_xCoO_2, comparing systems with light and heavy A-site ions, where heavier ions enhance phonon scattering and consequently reduce lattice thermal conductivity.[78]

1.3.2. Epitaxial $Ba_{1/3}CoO_2$ thin films

Based on this material design principle, barium was selected as the A-site ion because it is the heaviest among the alkali and alkaline-earth elements. $Ba_{1/3}CoO_2$ (BCO) epitaxial thin films were fabricated by ion exchange from $Na_{3/4}CoO_2$ precursor films, replacing Na^+ ions with Ba^{2+} ions.[76]

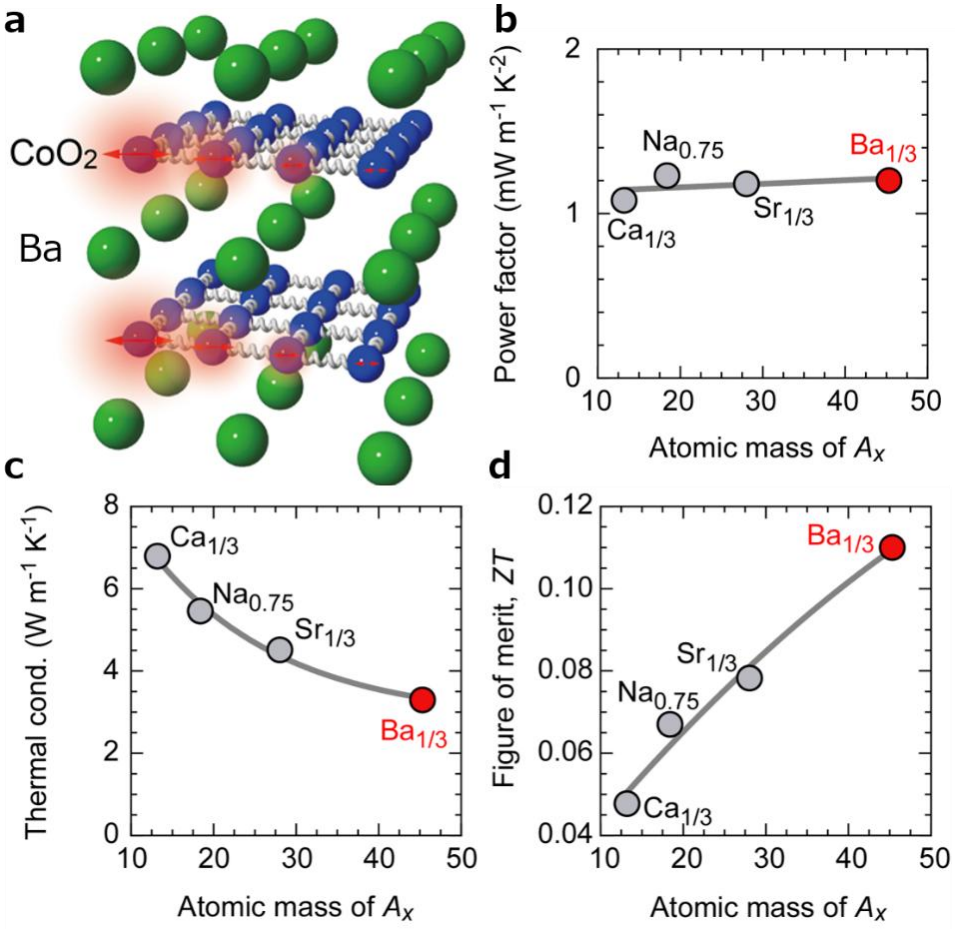

Figure 1-7. (a) Schematic illustrations of crystal structure of $Ba_{1/3}CoO_2$. (b–d) Atomic-mass dependence of (b) the power factor, (c) thermal conductivity, and (d) the figure of merit *ZT* at room temperature.[76]

Comparative studies of $Ca_{1/3}CoO_2$, $Na_{3/4}CoO_2$, $Sr_{1/3}CoO_2$, and BCO epitaxial films showed that the power factor remains nearly constant across the series (**Figure 1-7b**), whereas the in-plane thermal conductivity decreases sharply with increasing atomic mass of the A-site ion (**Figure 1-7c**). As a result, BCO epitaxial thin films exhibit a significantly enhanced room-temperature *ZT* of approximately 0.11, which is the highest value among the A_xCoO_2 compounds studied (**Figure 1-7d**).[76]

The thermoelectric performance and thermal stability of A_xCoO_2 were further evaluated at elevated temperatures in air. BCO was found to be structurally stable up to 600 °C, which is the highest temperature among the A_xCoO_2 series (**Figure 1-8**). This enhanced thermal stability is likely associated with the incorporation of the heaviest A-site ion, Ba, which stabilizes the layered structure.[79]

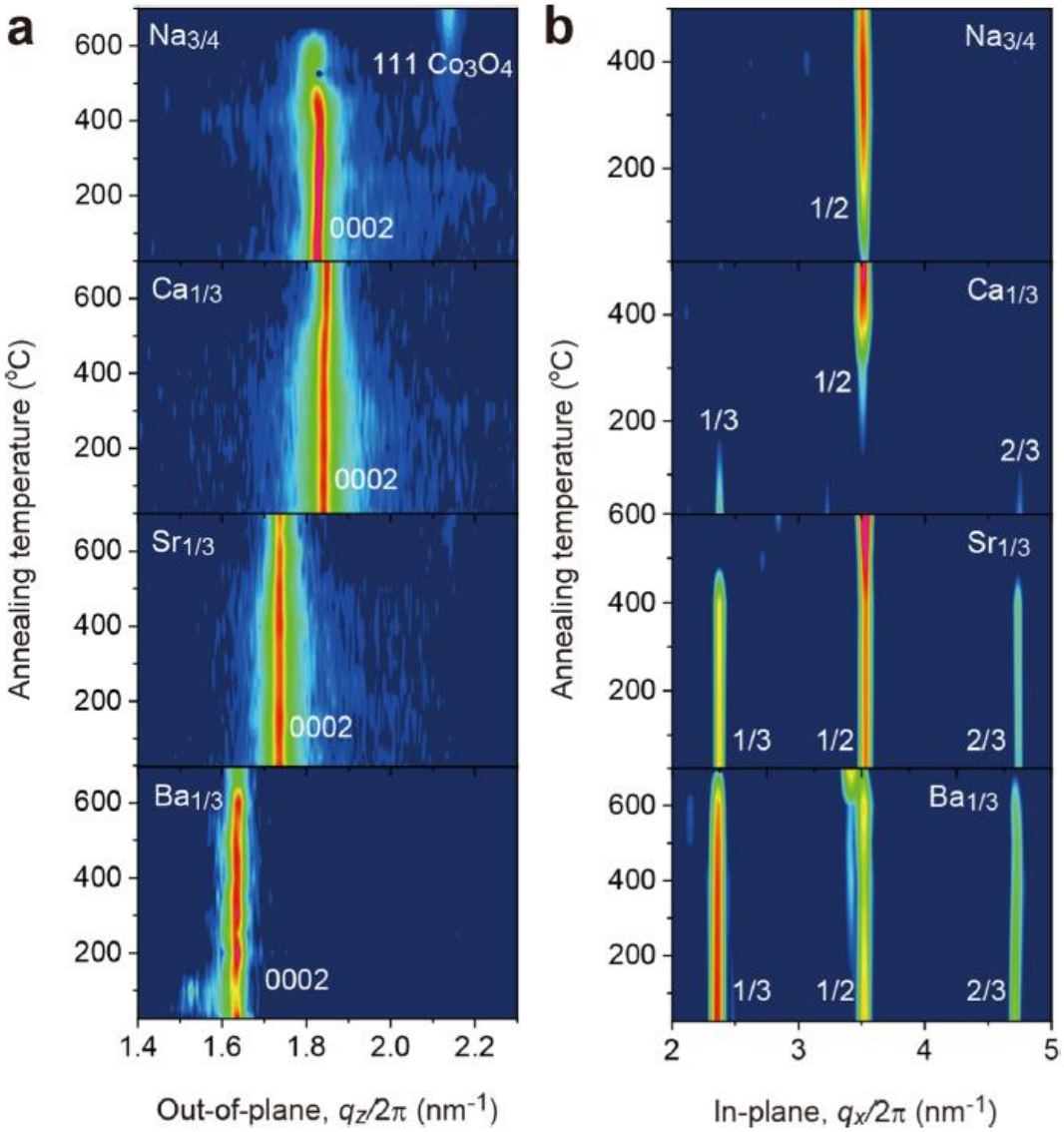

Figure 1-8. Change in the crystal structure of A_xCoO_2 films after annealing at high temperatures for 0.5 h in air.[79] (a) Out-of-plane XRD and (b) in-plane XRD patterns measured at room temperature after each annealing step.

A comparison of the temperature dependence of *ZT* values clearly demonstrates that BCO exhibits the best thermoelectric performance among the A_xCoO_2 compounds (**Figure 1-9a**). Notably, BCO reaches a *ZT* of approximately 0.55 at 600 °C, which represents the highest reported value among oxide thermoelectric materials and is comparable to those of p-type PbTe and SiGe (**Figure 1-9b**). These research highlight BCO as a highly promising candidate for high-temperature oxide thermoelectric applications.[79]

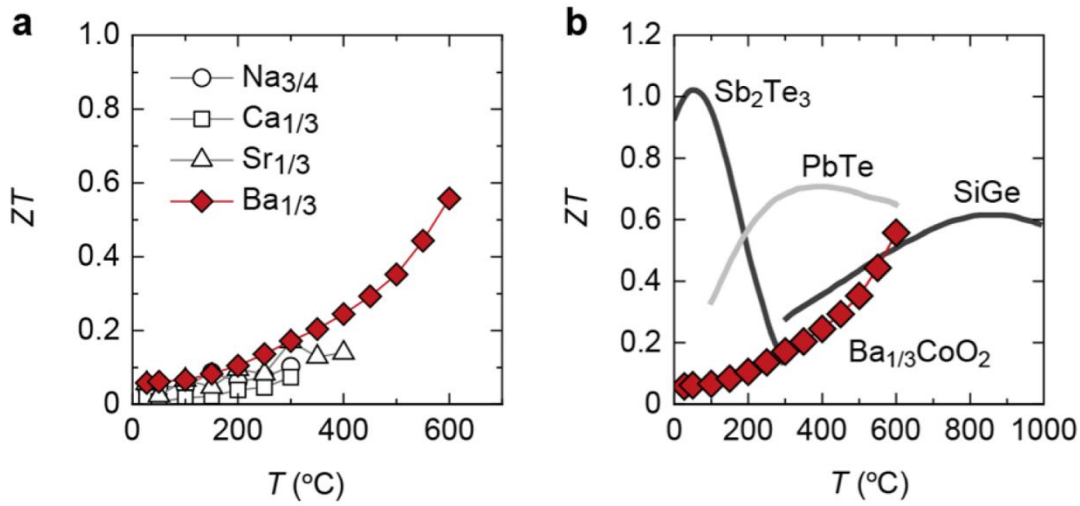

Figure 1-9. Temperature dependence of the in-plane *ZT* of epitaxial $Ba_{1/3}CoO_2$ thin films.[79] (a) Comparison among A_xCoO_2 (A = $Na_{3/4}$, $Ca_{1/3}$, $Sr_{1/3}$, and $Ba_{1/3}$). (b) Comparison with commercially available p-type thermoelectric materials.

1.3.3. Practical consideration for $Ba_{1/3}CoO_2$

As discussed in the previous sections, BCO has emerged as one of the most promising oxide thermoelectric materials among layered cobaltites. In particular, epitaxial BCO thin films exhibit simultaneously large thermopower and high electrical conductivity, resulting in excellent thermoelectric performance over a wide temperature range from room temperature to high temperatures. These results clearly indicate the strong potential of BCO for high-temperature thermoelectric applications.[76,79]

However, epitaxial BCO thin films typically have a thickness of approximately 150 nm and are deposited as heterostructures on insulating substrates such as Al_2O_3 or yttria-stabilized zirconia (YSZ), whose thickness is on the order of 0.5 mm. As a consequence, although the intrinsic thermoelectric properties of the BCO film are excellent, the overall thermoelectric performance of the entire sample is severely suppressed by the dominant thermal and electrical contributions of the substrate. Therefore, the thermoelectric performance evaluated in epitaxial thin-film geometries does not directly reflect the performance achievable at the device level.

Moreover, from the viewpoint of practical thermoelectric device implementation, epitaxial thin films inherently suffer from structural and processing limitations. Most thermoelectric generators are fabricated using bulk or ceramic materials, which allow

sufficient output power and mechanical robustness. Thin-film-based materials are limited in terms of power density and device architecture, making their direct application to large-scale thermoelectric modules challenging. Consequently, to translate the superior thermoelectric properties of BCO into practical applications, it is necessary to realize comparable properties in bulk, ceramic, or other large-area material forms.

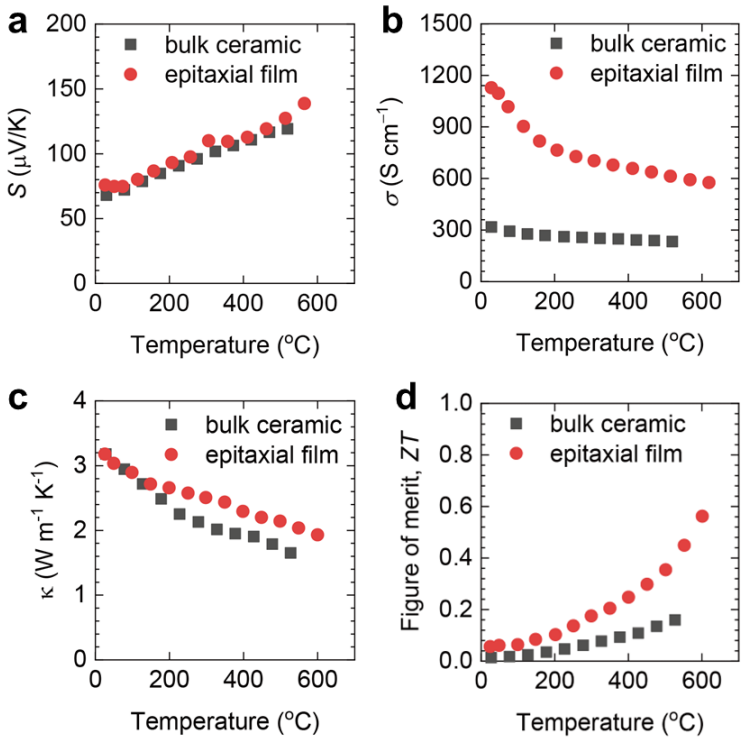

Figure 1-10. Temperature dependence of the thermoelectric properties of $Ba_{1/3}CoO_2$ (BCO) epitaxial thin films and bulk ceramics, including (a) thermopower, (b) electrical conductivity, (c) thermal conductivity, and (d) figure of merit *ZT*.[79-80]

Despite this necessity, the thermoelectric performance of bulk or ceramic BCO reported to date remains significantly inferior to that of epitaxial thin films. As shown in **Figure**

1-10, BCO ceramics exhibit a very low *ZT* value of approximately 0.014 at room temperature. This poor performance is primarily attributed to the markedly reduced electrical conductivity of bulk samples, which is typically around 300 S cm^{-1} at room temperature, compared to approximately 1500 S cm^{-1} observed in epitaxial films. The substantial reduction in electrical conductivity directly leads to a pronounced degradation of the overall thermoelectric performance.

In addition to the reduced electrical conductivity, the fundamental origin of the degraded thermoelectric performance in bulk BCO has not yet been clearly identified. The fabrication of high-density bulk or ceramic thermoelectric materials generally requires sintering processes at temperatures exceeding 1000 °C. However, BCO is known to undergo changes in its crystal structure at temperatures above approximately 600 °C. This intrinsic thermal instability poses a critical challenge for bulk fabrication, as the high-temperature sintering process necessary to achieve sufficient densification may simultaneously induce structural evolution that deteriorates the intrinsic thermoelectric properties.

Despite the importance of this issue, systematic studies on the high-temperature structural evolution of BCO and its direct impact on thermoelectric transport properties remain limited. In particular, the relationship between phase evolution during high-temperature treatment and the resulting electrical and thermal transport behavior has not been fully

clarified. A comprehensive understanding of these effects is therefore essential for identifying the factors responsible for the performance gap between epitaxial thin films and bulk ceramics, and for establishing viable processing routes toward scalable BCO-based thermoelectric materials.

In order to advance BCO as a practical thermoelectric material, it is therefore essential to verify the reproducibility of its thermoelectric properties in single-crystalline BCO that are free from substrate effects, and to clarify the factors responsible for the property differences between epitaxial thin films and bulk materials. Fundamental studies aimed at understanding the structural evolution and thermoelectric transport behavior during scale-up processes are required. These considerations form the basis of the objectives of this study, which are described in the following section.

1.4. Objective of This Study

The primary objective of this dissertation is to advance BCO toward practical thermoelectric applications by clarifying two critical issues identified in the preceding chapters: the reproducibility of intrinsic thermoelectric properties in substrate-free single-crystalline BCO, and the mechanisms responsible for the degraded thermoelectric performance in bulk ceramics. Through addressing these issues, this study aims to provide new insights into the practical utilization of layered cobalt oxide thermoelectrics.

In this work, epitaxial BCO thin films with a thickness of approximately 600 nm were fabricated on Al_2O_3 thin-film substrates. By employing a water-soluble process, the films were successfully exfoliated from the substrates to obtain freestanding single-crystalline BCO sheets. Even after removal from the substrate, the freestanding BCO single-crystalline sheets retained excellent thermoelectric performance, demonstrating the intrinsic transport properties of BCO without substrate-induced suppression.[81]

Furthermore, to elucidate the origin of the poor thermoelectric performance observed in bulk BCO, epitaxial BCO thin films grown on yttria-stabilized zirconia (YSZ) substrates were annealed in air over a wide temperature range from 100 °C to 1000 °C. The evolution of crystal structure and thermoelectric properties was systematically investigated. BCO was found to decompose into $BaCoO_3$, $BaCoO_{2.6}$, and Co_3O_4 at temperatures above approximately 700 °C. This decomposition induces a transition in the electronic transport mechanism from metallic conduction to percolation conduction, leading to a pronounced loss of electrical conductivity. These findings clarify the strong correlation between high-temperature structural evolution and thermoelectric performance degradation in BCO.[82]
This dissertation is organized as follows.

In Chapter 1, the fundamental principles of thermoelectrics, the development of thermoelectric materials, and the characteristics of layered cobalt oxides are introduced.

In Chapter 2, the experimental methods used for thin-film growth, structural characterization, and thermoelectric property measurements are described.

In Chapter 3, the fabrication of freestanding $Ba_{1/3}CoO_2$ single-crystalline films and their thermoelectric properties are presented, highlighting the intrinsic transport behavior of free-standing single crystalline BCO sheets.

In Chapter 4, the high-temperature decomposition behavior of $Ba_{1/3}CoO_2$ and its impact on electron transport are discussed in detail, with particular emphasis on the mechanisms underlying performance degradation during high temperature annealing.

Finally, Chapter 5 summarizes the main conclusions of this dissertation and discusses future perspectives for practical thermoelectric applications of layered cobalt oxides.

References

[1] Rowe, D. M., *CRC handbook of thermoelectrics*. CRC press: 1995.

[2] Goldsmid, H. J., *Introduction to thermoelectricity*. Springer: 2010; Vol. 121.

[3] Seebeck, T. J., *Magnetische polarisation der metalle und erze durch temperatur-differenz*. Engelmann: 1895; Vol. 70.

[4] Cutler, M. *et al.*, Observation of Anderson localization in an electron gas. *Phys. Rev.* **181**, 1336 (1969).

[5] Franz, R. *et al.*, Ueber die wärme-leitungsfähigkeit der metalle. *Annalen der Physik* **165**, 497-531 (1853).

[6] He, J. *et al.*, Advances in thermoelectric materials research: Looking back and moving forward. *Science* **357**, eaak9997 (2017).

[7] Hsu, K. F. *et al.*, Cubic $AgPb_mSbTe_{2+m}$: bulk thermoelectric materials with high figure of merit. *Science* **303**, 818-821 (2004).

[8] Heremans, J. P. *et al.*, Enhancement of thermoelectric efficiency in PbTe by distortion of the electronic density of states. *Science* **321**, 554-557 (2008).

[9] Pei, Y. *et al.*, Convergence of electronic bands for high performance bulk thermoelectrics. *Nature* **473**, 66-69 (2011).

[10] Biswas, K. *et al.*, High-performance bulk thermoelectrics with all-scale hierarchical architectures. *Nature* **489**, 414-418 (2012).

[11] Fu, T. *et al.*, Enhanced thermoelectric performance of PbTe bulk materials with figure

of merit *ZT*> 2 by multi-functional alloying. *J. Materiomics* **2**, 141-149 (2016).

[12] Wang, H. *et al.*, Weak electron–phonon coupling contributing to high thermoelectric performance in n-type PbSe. *Proc. Natl. Acad. Sci. U.S.A.* **109**, 9705-9709 (2012).

[13] Zhao, L.-D. *et al.*, High thermoelectric performance via hierarchical compositionally alloyed nanostructures. *J. Am. Chem. Soc.* **135**, 7364-7370 (2013).

[14] Zhao, L.-D. *et al.*, High performance thermoelectrics from earth-abundant materials: enhanced figure of merit in PbS by second phase nanostructures. *J. Am. Chem. Soc.* **133**, 20476-20487 (2011).

[15] Wang, H. *et al.*, High thermoelectric efficiency of n-type PbS. *Adv. Energy Mater.* **3**, 488-495 (2013).

[16] Ibánez, M. *et al.*, High-performance thermoelectric nanocomposites from nanocrystal building blocks. *Nat. Commun.* **7**, 10766 (2016).

[17] Liu, H. *et al.*, Copper ion liquid-like thermoelectrics. *Nat. Mater.* **11**, 422-425 (2012).

[18] Liu, H. *et al.*, Ultrahigh Thermoelectric Performance by Electron and Phonon Critical Scattering in $Cu_2Se_{1-x}I_x$. *Adv. Mater.* **25**, 6607-6612 (2013).

[19] Zhong, B. *et al.*, High superionic conduction arising from aligned large lamellae and large figure of merit in bulk $Cu_{1.94}Al_{0.02}Se$. *Appl. Phys. Lett.* **105**, (2014).

[20] Olvera, A. *et al.*, Partial indium solubility induces chemical stability and colossal thermoelectric figure of merit in Cu_2Se. *Energy Environ. Sci.* **10**, 1668-1676 (2017).

[21] Ge, Z.-H. *et al.*, Synthesis and transport property of $Cu_{1.8}S$ as a promising thermoelectric compound. *Chem. Commun.* **47**, 12697-12699 (2011).

[22] He, Y. *et al.*, High thermoelectric performance in non-toxic earth-abundant copper sulfide. *Adv. Mater.* **26**, 3974-3978 (2014).

[23] Zhao, L.-D. *et al.*, Ultralow thermal conductivity and high thermoelectric figure of merit in SnSe crystals. *Nature* **508**, 373-377 (2014).

[24] Duong, A. T. *et al.*, Achieving *ZT*= 2.2 with Bi-doped n-type SnSe single crystals. *Nat. Commun.* **7**, 13713 (2016).

[25] Peng, K. *et al.*, Broad temperature plateau for high *ZT* s in heavily doped p-type SnSe single crystals. *Energy Environ. Sci.* **9**, 454-460 (2016).

[26] Zhao, L.-D. *et al.*, Ultrahigh power factor and thermoelectric performance in hole-doped single-crystal SnSe. *Science* **351**, 141-144 (2016).

[27] Zhang, J. *et al.*, Discovery of high-performance low-cost n-type Mg_3Sb_2-based thermoelectric materials with multi-valley conduction bands. *Nat. Commun.* **8**, 13901 (2017).

[28] Zhao, L.-D. *et al.*, $Bi_{1-x}Sr_xCuSeO$ oxyselenides as promising thermoelectric materials. *Appl. Phys. Lett.* **97**, (2010).

[29] Zhao, L.-D. *et al.*, BiCuSeO oxyselenides: new promising thermoelectric materials. *Energy Environ. Sci.* **7**, 2900-2924 (2014).

[30] Poudel, B. *et al.*, High-thermoelectric performance of nanostructured bismuth antimony telluride bulk alloys. *Science* **320**, 634-638 (2008).

[31] Xie, W. *et al.*, Unique nanostructures and enhanced thermoelectric performance of melt-spun BiSbTe alloys. *Appl. Phys. Lett.* **94**, (2009).

[32] Kim, S. I. *et al.*, Dense dislocation arrays embedded in grain boundaries for high-performance bulk thermoelectrics. *Science* **348**, 109-114 (2015).

[33] Liu, W. *et al.*, Convergence of conduction bands as a means of enhancing thermoelectric performance of n-type $Mg_2Si_{1-x}Sn_x$ solid solutions. *Phys. Rev. Lett.* **108**, 166601 (2012).

[34] Plirdpring, T. *et al.*, Chalcopyrite $CuGaTe_2$: A High-Efficiency Bulk Thermoelectric Material. *Adv. Mater.* **24**, 3622-3626 (2012).

[35] Luo, Y. *et al.*, Progressive Regulation of Electrical and Thermal Transport Properties to High-Performance $CuInTe_2$ Thermoelectric Materials. *Adv. Energy Mater.* **6**, 1600007 (2016).

[36] Sales, B. C. *et al.*, Filled Skutterudite Antimonides: A New Class of Thermoelectric Materials. *Science* **272**, 1325-1328 (1996).

[37] Shi, X. *et al.*, Multiple-filled skutterudites: high thermoelectric figure of merit through separately optimizing electrical and thermal transports. *J. Am. Chem. Soc.* **133**, 7837-7846 (2011).

[38] Rogl, G. *et al.*, n-Type skutterudites $(R,Ba,Yb)_yCo_4Sb_{12}$ (R=Sr, La, Mm, DD, SrMm, SrDD) approaching $ZT \approx 2.0$. *Acta Mater.* **63**, 30-43 (2014).

[39] Yamaguchi, S. *et al.*, Thermoelectric properties and figure of merit of a Te-doped InSb bulk single crystal. *Appl. Phys. Lett.* **87**, (2005).

[40] Cheng, Y. *et al.*, New insight into InSb-based thermoelectric materials: from a divorced eutectic design to a remarkably high thermoelectric performance. *J. Mater.*

Chem. A **5**, 5163-5170 (2017).

[41] Joshi, G. *et al.*, Enhancement in Thermoelectric Figure-Of-Merit of an N-Type Half-Heusler Compound by the Nanocomposite Approach. *Adv. Energy Mater.* **1**, 643-647 (2011).

[42] Yan, X. *et al.*, Thermoelectric Property Study of Nanostructured p-Type Half-Heuslers (Hf, Zr, Ti)$CoSb_{0.8}Sn_{0.2}$. *Adv. Energy Mater.* **3**, 1195-1200 (2013).

[43] Fu, C. *et al.*, Realizing high figure of merit in heavy-band p-type half-Heusler thermoelectric materials. *Nat. Commun.* **6**, 8144 (2015).

[44] Tritt, T. M. *et al.*, Thermoelectric materials, phenomena, and applications: a bird's eye view. *MRS Bull.* **31**, 188-198 (2006).

[45] Snyder, G. J. *et al.*, Complex thermoelectric materials. *Nat. Mater.* **7**, 105-114 (2008).

[46] Zhao, H. *et al.*, High thermoelectric performance of MgAgSb-based materials. *Nano Energy* **7**, 97-103 (2014).

[47] Rogl, G. *et al.*, Thermoelectric properties of novel skutterudites with didymium: $DD_y(Fe_{1-x}Co_x)_4Sb_{12}$ and $DD_y(Fe_{1-x}Ni_x)_4Sb_{12}$. *Intermetallics* **18**, 57-64 (2010).

[48] Tan, G. *et al.*, Codoping in SnTe: enhancement of thermoelectric performance through synergy of resonance levels and band convergence. *J. Am. Chem. Soc.* **137**, 5100-5112 (2015).

[49] Chang, C. *et al.*, 3D charge and 2D phonon transports leading to high out-of-plane *ZT* in n-type SnSe crystals. *Science* **360**, 778-783 (2018).

[50] Koumoto, K. *et al.*, Complex oxide materials for potential thermoelectric

applications. *MRS Bull.* **31**, 206-210 (2006).

[51] Koumoto, K. *et al.*, Oxide thermoelectric materials: a nanostructuring approach. *Annu. Rev. Mater. Res.* **40**, 363-394 (2010).

[52] Koumoto, K. *et al.*, Thermoelectric ceramics for energy harvesting. *J. Am. Ceram. Soc.* **96**, 1-23 (2013).

[53] Hogarth, C. *et al.*, XXV. Variation with oxygen pressure of the thermoelectric power of cadmium oxide. *The London, Edinburgh, and Dublin Philosophical Magazine and Journal of Science* **40**, 273-282 (1949).

[54] Hutson, A., Electronic properties of ZnO. *J. Phys. Chem. Solids* **8**, 467-472 (1959).

[55] Arvin, M., Electrical conductivity and thermoelectric power of indium oxide. *Phys. Chem. Solids* **23**, (1962).

[56] Frederikse, H. *et al.*, Electronic transport in strontium titanate. *Phys. Rev.* **134**, A442 (1964).

[57] Thurber, W. *et al.*, Thermal Conductivity and Thermoelectric Power of Rutile (Ti O_2). *Phys. Rev.* **139**, A1655 (1965).

[58] Young, A. *et al.*, Electrical conductivity and thermoelectric power of Cu_2O. *J. Phys. Chem. Solids* **30**, 249-252 (1969).

[59] Bednorz, J. G. *et al.*, Possible high T c superconductivity in the Ba− La− Cu− O system. *Z. Phys. B Condens. Matter* **64**, 189-193 (1986).

[60] Cooper, J. *et al.*, Thermoelectric power of some high-T_c oxides. *Phys. Rev. B* **35**, 8794 (1987).

[61] Chen, J. *et al.*, Determination of charge carriers in superconducting La-Ba-Cu-O by thermoelectric measurements. *Phys. Rev. B* **35**, 7124 (1987).

[62] Mitra, N. *et al.*, Thermoelectric power of the Tl-Ca-Ba-Cu-O superconductor. *Phys. Rev. B* **38**, 7064 (1988).

[63] Ohtaki, M. *et al.*, Electrical transport properties and high-temperature thermoelectric performance of $(Ca_{0.9}M_{0.1})MnO_3$ (M= Y, La, Ce, Sm, In, Sn, Sb, Pb, Bi). *J. Solid State Chem.* **120**, 105-111 (1995).

[64] Ohtaki, M. *et al.*, High-temperature thermoelectric properties of $(Zn_{1-x}Al_x)O$. *J. Appl. Phys.* **79**, 1816-1818 (1996).

[65] Terasaki, I. *et al.*, Large thermoelectric power in $NaCo_2O_4$ single crystals. *Phys. Rev. B* **56**, R12685 (1997).

[66] Masset, A. *et al.*, Misfit-layered cobaltite with an anisotropic giant magnetoresistance: $Ca_3Co_4O_9$. *Phys. Rev. B* **62**, 166 (2000).

[67] Funahashi, R. *et al.*, An oxide single crystal with high thermoelectric performance in air. *Jpn. J. Appl. Phys.* **39**, L1127 (2000).

[68] Ohta, S. *et al.*, High-temperature carrier transport and thermoelectric properties of heavily La-or Nb-doped $SrTiO_3$ single crystals. *J. Appl. Phys.* **97**, (2005).

[69] Ohta, S. *et al.*, Large thermoelectric performance of heavily Nb-doped $SrTiO_3$ epitaxial film at high temperature. *Appl. Phys. Lett.* **87**, (2005).

[70] Okuda, T. *et al.*, Large thermoelectric response of metallic perovskites: $Sr_{1-x}La_xTiO_3$ ($0< x<0.1$). *Phys. Rev. B* **63**, 113104 (2001).

[71] Zhang, Y. *et al.*, Recent progress in thermoelectric layered cobalt oxide thin films. *NPG Asia Materials* **15**, 67 (2023).

[72] Ohta, H. *et al.*, Recent progress in oxide thermoelectric materials: p-type $Ca_3Co_4O_9$ and n-type $SrTiO_3^-$. *lnorg. Chem.* **47**, 8429-8436 (2008).

[73] Koshibae, W. *et al.*, Thermopower in cobalt oxides. *Phys. Rev. B* **62**, 6869 (2000).

[74] Takeuchi, T. *et al.*, Contribution of electronic structure to the large thermoelectric power in layered cobalt oxides. *Phys. Rev. B* **69**, 125410 (2004).

[75] Wang, Y. *et al.*, Spin entropy as the likely source of enhanced thermopower in $Na_xCo_2O_4$. *Nature* **423**, 425-428 (2003).

[76] Takashima, Y. *et al.*, Layered cobalt oxide epitaxial films exhibiting thermoelectric *ZT* = 0.11 at room temperature. *J. Mater. Chem. A* **9**, 274-280 (2021).

[77] Voneshen, D. *et al.*, Suppression of thermal conductivity by rattling modes in thermoelectric sodium cobaltate. *Nat. Mater.* **12**, 1028-1032 (2013).

[78] Cho, H. J. *et al.*, Anisotropic Heat Conduction in Ion-Substituted Layered Cobalt Oxides. *Adv. Mater. Interfaces* **7**, 1901816 (2020).

[79] Zhang, X. *et al.*, $Ba_{1/3}CoO_2$: A Thermoelectric Oxide Showing a Reliable *ZT* of approximately 0.55 at 600 ºC in Air. *ACS Appl Mater Interfaces* **14**, 33355-60 (2022).

[80] Liu, J. *et al.*, High-temperature thermoelectric properties of layered Ba_xCoO_2. *Scripta Mater.* **100**, 63-65 (2015).

[81] Kang, K. *et al.*, Fabrication and thermoelectric properties of freestanding $Ba_{1/3}CoO_2$ single-crystalline films. *ACS Applied Electronic Materials* **5**, 5749-5754 (2023).

[82] Kang, K. *et al.*, Decomposition Behavior of a Thermoelectric Oxide at High-Temperatures and Its Impact on the Thermoelectric Properties. *ACS Applied Energy Materials* **9**, 1883-1890 (2026).

Chapter 2. Experimental procedures

2.1. Thin film fabrication

Thin-film deposition techniques are generally classified into two categories: physical vapor deposition (PVD) and chemical vapor deposition (CVD), depending on whether the film is formed through physical transport or chemical reactions of the source material. In this study, all epitaxial single-crystalline films used for the fabrication of the oxide thermoelectric thin films were grown by pulsed laser deposition (PLD), which is a representative PVD technique. Therefore, this section focuses exclusively on PVD-based thin-film growth methods.

PVD involves the physical transport of source materials, either in solid or molten states, to the substrate surface under high vacuum conditions. PVD processes are typically characterized by relatively low deposition temperatures, high purity of deposited films, and simple system configurations. With the advancement of vacuum engineering since the mid-20th century, a variety of PVD techniques have been developed.

Among vacuum evaporation-based methods, electron beam evaporation and molecular beam epitaxy (MBE) enable precise control of film thickness and composition. In addition, several advanced deposition techniques utilizing energetic particle–solid

interactions have been established, including sputtering, ion beam sputtering, magnetron sputtering, pulsed laser deposition (PLD), and ion beam-assisted deposition (IBAD). These methods provide enhanced control over film density, crystallinity, and interfacial quality.

2.1.1. Pulsed Laser Deposition (PLD)

Pulsed laser deposition (PLD) is a PVD technique and, together with sputtering, is widely used for the growth of high-quality thin films. In this method, a high-energy pulsed laser beam—typically an excimer or Nd:YAG laser—is focused onto a ceramic target having the same chemical composition as the desired film. When the laser pulse irradiates the target surface, most of the incident energy (excluding the reflected portion) is absorbed within a shallow optical penetration depth. This induces rapid local heating and results in laser ablation, in which the target surface is explosively vaporized. The ablated species form a hot and highly ionized plasma plume directed toward the substrate, and the film grows as these energetic species condense on the heated substrate surface.[1]

Pulsed lasers are used instead of continuous-wave sources to avoid excessive target heating and to achieve the high instantaneous power density required for efficient ablation. A schematic illustration of the PLD process is shown in **Figure 2-1**. In each laser pulse, a small amount of target material is removed and accelerated toward the substrate. The plume expands predominantly along the target normal direction, and its angular

distribution is commonly described by a $\cos^n(\theta)$ function, where n typically ranges from ~4 to 30 depending on the material and laser conditions.[2] Factors such as surface texturing from repeated ablation, spatial inhomogeneity in the laser spot, and partial laser absorption by the plasma can lead to non-uniform deposition. However, uniformity over a large area can be achieved by rastering the target and rotating the substrate. Similar to molecular-scale evaporation, PLD enables precise control over the film growth at the atomic level under optimized conditions.

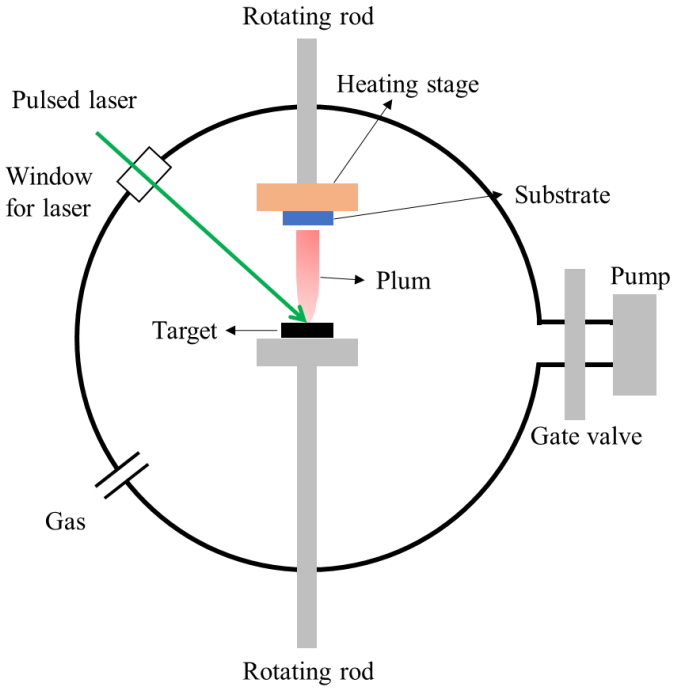

Figure 2-1. Schematic of PLD

PLD offers several advantages for complex oxide thin-film deposition:

1. **Accurate stoichiometric transfer:** The high-power pulsed ablation process generates a plume whose composition closely matches that of the target. By controlling the oxygen partial pressure during deposition, oxygen loss can be minimized, enabling highly stoichiometric oxide films.
2. **High deposition efficiency:** Ablated species possess kinetic energies of approximately 10–100 eV, promoting surface diffusion and allowing epitaxial growth at relatively low substrate temperatures.
3. **Flexible parameter control:** Because the laser system operates independently from the chamber vacuum system, laser parameters such as fluence, pulse frequency, and spot size can be readily adjusted for different materials.
4. **High compatibility with research environments:** The directional nature of the plume minimizes chamber contamination, facilitating rapid material changes and making PLD well suited for exploratory thin-film research.
5. **Integration with in-situ monitoring tools:** Modern PLD systems can incorporate real-time diagnostics such as reflection high-energy electron diffraction (RHEED) and rotating multi-target carousels, allowing precise control of growth mode and multilayer structures.

The development of high-power excimer lasers, such as the KrF laser (λ = 248 nm), significantly expanded the applicability of PLD by enabling shorter wavelengths, higher

pulse energies, and more efficient ablation of complex materials. In this study, epitaxial oxide thermoelectric thin films used were grown using a PLD system equipped with a Coherent COMPex 102 excimer laser (λ = 248 nm).

2.1.2. Direct Current (DC) Sputtering

DC sputtering is a cost-effective PVD technique that is well suited for depositing electrically conductive materials. In this process, high-purity argon gas is introduced into a vacuum chamber in which the target material and the substrate are arranged parallel to each other, and a pulsed DC current is applied to ionize the argon gas. The generated Ar^+ ions are accelerated toward the negatively biased metal target (cathode) and collide with its surface, resulting in the ejection of metal atoms through momentum transfer. The sputtered atoms are then transported through the plasma and subsequently condense on the positively biased substrate (anode), forming a thin-film coating.

In this study, a DC sputtering system was employed to deposit Pt top electrodes on thermoelectric oxide thin films for electrical transport and thermal conductivity measurements.

2.2. Crystallographic analysis

2.2.1. X-ray diffraction (XRD)

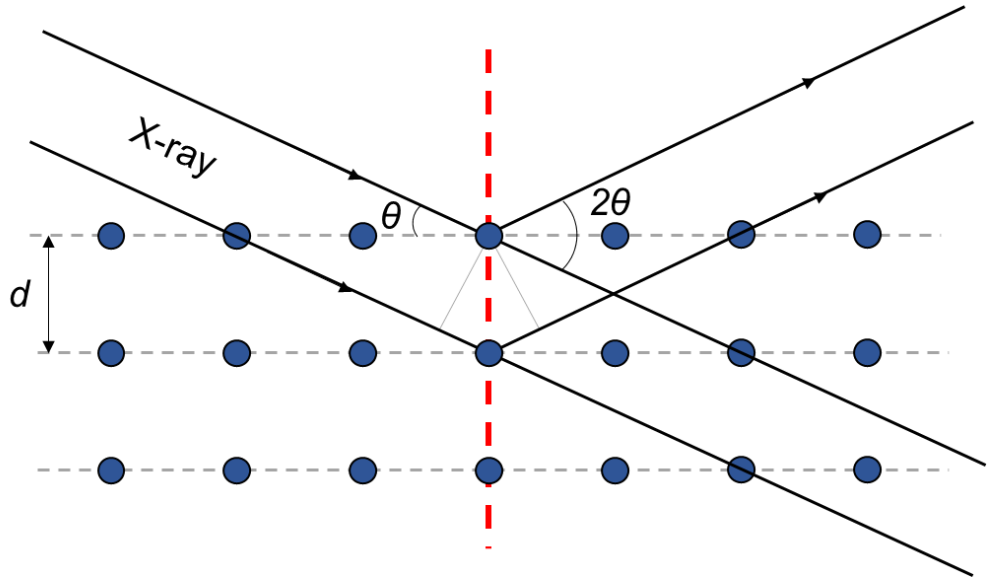

Figure 2-2. Geometric relationship of Bragg's law

In 1895, the German physicist Wilhelm Röntgen discovered a highly penetrating form of radiation, which he named X-rays. Later, in 1912, P. P. Ewald established the theoretical framework for X-ray scattering in crystals based on the hypothesis that crystals consist of atoms arranged in a periodic spatial lattice. Through discussions with Ewald, Max von Laue recognized that X-rays possess a suitable wavelength to produce diffraction from crystal lattices and reported the first X-ray diffraction pattern in 1912. Inspired by this discovery, W. H. Bragg and W. L. Bragg formulated Bragg's law, which provides a quantitative description of X-ray diffraction.

When X-rays interact with crystalline material, atoms located at the lattice points act as independent scattering centers. Constructive interference occurs when the path difference between X-rays scattered from adjacent lattice planes is an integer multiple of the X-ray wavelength. As shown in **Figure 2-2**, This geometric relationship is described by Bragg's law:

$$2 \cdot d \cdot \sin\theta = n \cdot \lambda \quad (2.1)$$

where d is the interplanar spacing, θ is the Bragg angle, λ is the wavelength of the incident X-rays, and n is the diffraction order. Based on this principle, X-ray diffraction is a powerful, non-destructive structural analysis technique widely used in materials science, physics, geology, and various industrial and medical applications to determine crystal structure, lattice parameters, preferred orientation, and crystallinity.

In this study, the crystal structures of thermoelectric thin films used as the active layers of thermal transistors were analyzed using a high-resolution X-ray diffractometer (HRXRD, ATX-G, Rigaku, Japan). A Cu Kα1 radiation source with a wavelength of 1.5406 Å was employed. Characteristic X-rays are generated when accelerated electrons collide with a copper target, causing inner-shell electron transitions that emit X-rays with a specific wavelength corresponding to the energy difference.

Several XRD measurement modes, including ω–2θ scanning, rocking curve (ω scan), X-ray reflectivity (XRR), in-plane scanning, and φ scanning, were employed. The ω–2θ scan is the most fundamental measurement mode, in which the incident angle ω and the

diffraction angle 2θ are synchronously varied while the sample remains fixed. This method is widely used to analyze the crystal structure and lattice parameters of thin films. For epitaxial thin films, the crystallographic orientation is constrained by the substrate; therefore, an additional correction angle ω is introduced to precisely satisfy the diffraction condition during ω–2θ measurements.

The crystallinity of the thin films was evaluated using rocking curve measurements. In this method, the diffraction angle 2θ corresponding to a specific Bragg peak is fixed, while the incident angle ω is scanned. The full width at half maximum (FWHM) of the rocking curve is commonly used as an indicator of crystal quality, with smaller FWHM values representing higher crystallinity.

X-ray reflectivity (XRR) measurements were performed to determine the thickness and surface/interface roughness of the thin films. XRR measurements are typically conducted at low incident angles below 6°, where X-rays are reflected from both the film surface and the film–substrate interface, forming interference fringes. The period of these fringes is directly related to the film thickness, while their decay behavior reflects the surface and interface roughness. In addition, the critical angle behavior provides information on the electron density of the film. The approximate film thickness can be derived using the Bragg equation:

$$H \approx \frac{\lambda}{2} \cdot \frac{1}{\theta_{m+1} - \theta_m} = \frac{\lambda}{2} \cdot \frac{1}{T} \tag{2.2}$$

φ scans were conducted by rotating the sample azimuthally through 360° with respect to a selected crystallographic plane to investigate the in-plane epitaxial relationship and crystal symmetry between the thin films and the substrates. In-plane XRD measurements were additionally performed to analyze the in-plane lattice structure of the epitaxial thin films.

Through these comprehensive HRXRD analyses, the crystal structure, epitaxial growth characteristics, crystallinity, film thickness, and interface properties of the thermoelectric oxide thin films were systematically evaluated in this study.

2.2.2. Scanning Transmission Electron Microscopy (STEM)

High-angle annular dark-field scanning transmission electron microscopy (HAADF-STEM) was employed to investigate the detailed microstructure of the films. In STEM, a finely focused electron probe is formed by a condenser lens system and scanned across the specimen in a raster pattern. As the incident electrons interact with the sample, they are scattered both elastically and inelastically, leading to changes in their propagation direction and energy. The transmitted and scattered electrons are collected by various detectors positioned at different angular ranges, which enables multiple imaging and analytical modes to be realized within the same instrument.

In annular dark-field (ADF) STEM, electrons scattered to intermediate and high angles

are collected by an annular detector. Because the scattering cross-section in this angular range is dominated by incoherent, Rutherford-type elastic scattering and thermal diffuse scattering (TDS), the intensity is approximately proportional to a power of the atomic number ($\sim Z^{1.6}$–Z^2) of the atomic columns. As a result, heavier elements appear brighter, whereas lighter elements provide weaker contrast.[3-4] When the inner collection angle of the detector is sufficiently large, this mode is referred to as high-angle annular dark-field (HAADF) STEM, and the resulting images are often called "Z-contrast" micrographs due to their strong dependence on the atomic number. This Z-contrast imaging is particularly suitable for visualizing the position of heavy-element columns, interfaces, and compositional inhomogeneities at the atomic scale.

To improve the visibility of light elements, such as oxygen or alkali/alkaline-earth cations, complementary imaging modes can be employed. Annular bright-field (ABF) STEM utilizes an annular detector placed at relatively low scattering angles, where both the unscattered beam and electrons scattered to small angles are detected.[5] In ABF images, light-element columns can be visualized simultaneously with heavy-element columns, enabling direct observation of the complete crystal sublattice. Low-angle annular dark-field (LAADF) STEM collects electrons at lower scattering angles than HAADF, providing contrast that is more sensitive to strain, bonding, and light-element distributions.[6] By combining HAADF, ABF, and LAADF images acquired from the same region, both the heavy-atom framework and the accompanying light-element sublattice

can be reconstructed with high spatial resolution.

In addition to imaging, STEM offers powerful spectroscopic capabilities. Electron energy-loss spectroscopy (EELS) analyzes the energy distribution of inelastically scattered electrons and provides information on the local electronic structure, such as valence state, coordination environment, and unoccupied density of states.[7] Energy-dispersive X-ray spectroscopy (EDS) detects characteristic X-rays emitted from the specimen and is used to quantify the elemental composition and to map the spatial distribution of constituent elements at the nanoscale. The combination of HAADF imaging with EELS and EDS enables direct correlation between structure, composition, and electronic states in complex oxide systems.

In this thesis, a Cs-corrected STEM (JEM-ARM200CF, JEOL) operated at an accelerating voltage of 200 keV was used to visualize the atomic arrangements in the active layers of the thermal transistors. HAADF-STEM imaging was primarily employed to resolve the heavy-element sublattice and to identify structural defects and interfaces. Where necessary, ABF/LAADF STEM imaging and STEM–EELS/EDS analyses were additionally conducted to obtain complementary information on the light-element sublattice, local chemical composition, and electronic structure of the thermoelectric oxide thin films.

2.2.3. Electron Energy Loss Spectroscopy (EELS)

Electron energy-loss spectroscopy (EELS) was employed to investigate the local electronic structure, bonding environment, and chemical composition of the thermoelectric oxide thin films at the nanoscale. In EELS, inelastically scattered electrons transmitted through a thin specimen lose a characteristic amount of energy due to interactions with atomic electrons, such as inner-shell ionization, interband transitions, and plasmon excitations. By analyzing the energy-loss distribution of these transmitted electrons, detailed information on elemental identity, oxidation states, coordination geometry, and unoccupied electronic density of states can be obtained with high spatial resolution.[7]

The low-loss region of the EELS spectrum (typically below ~50 eV) contains information on plasmon excitations and valence electron behavior, which is related to the dielectric response and electron density of the material. The core-loss region, appearing at higher energy losses, corresponds to inner-shell ionization edges that are characteristic of specific elements. For example, the O-K edge provides information on oxygen coordination and hybridization with transition-metal states, while the Co L2,3 edges reflect the electronic structure and oxidation state of cobalt through fine-structure analysis of the white-line intensity and energy positions.

By acquiring EELS spectra in the STEM mode, spatially resolved spectral information can be obtained simultaneously with atomic-resolution imaging. Spectrum imaging allows the collection of a full EELS spectrum at each probe position, enabling two-dimensional elemental and chemical-state mapping across interfaces, grain boundaries, and phase boundaries. This capability is particularly powerful for investigating nanoscale compositional variations and redox behavior in complex oxide thin films.

In this study, EELS measurements were performed using a Cs-corrected STEM (JEM-ARM200CF, JEOL) operated at an accelerating voltage of 200 keV. The EELS spectrometer was used to analyze the Co $L_{2,3}$, Ba M and O-K edges in order to evaluate the cobalt valence state and oxygen coordination environment in the thermoelectric oxide thin films. Line-scan and mapping analyses were conducted across selected regions to correlate local structural variations observed in HAADF-STEM images with changes in electronic structure and chemical composition.

Through the combined use of EELS and atomic-resolution STEM imaging, nanoscale variations in oxidation state, oxygen stoichiometry, and phase evolution in the active layers of the thermal transistors were systematically investigated.

2.3. Electrical transport properties

Electrical transport properties are intrinsic characteristics of materials and provide fundamental information for identifying whether a thin film exhibits metallic, semiconducting, or insulating behavior. These properties reflect the underlying electron transport mechanisms and are essential for understanding carrier conduction in functional materials.

In the context of thermoelectric research, the evaluation of electrical transport properties plays a particularly important role, as thermoelectric performance is directly governed by the electrical conductivity, thermopower, and thermal conductivity of a material. Accurate assessment of electrical transport behavior is therefore indispensable for analyzing charge-carrier transport, optimizing material performance, and clarifying the structure–property relationships relevant to thermoelectric applications.

Accordingly, systematic measurements of the electrical transport properties were carried out in this study to evaluate the thermoelectric characteristics of the thin-film active layers and to provide a reliable basis for subsequent analysis of their thermoelectric performance.

2.3.1. Electrical conductivity

Electrical conductivity of the thin-film active layers was evaluated using a four-electrode configuration. Electrical transport measurements in thin films commonly employ either a two-electrode or a four-electrode method, each offering distinct advantages depending on the resistance range and measurement environment. The conventional two-electrode

method is simple to operate and generally exhibits low signal-loss probability because the electrical leads and measurement electrodes are directly connected. However, when measuring low-resistance samples, the intrinsic resistance of the leads and contact interfaces becomes non-negligible, which may introduce systematic errors.

To minimize these contributions, the four-electrode method was adopted in this study. In this configuration, the current is supplied through the outer electrodes while the voltage drop is detected through the inner electrodes, effectively eliminating the influence of lead and contact resistances. The sheet resistance (R) was determined from four sequential measurement configurations, expressed as

$$R_1: R_{12,43}=\frac{V_{2(43)}-V_{1(43)}}{I_{12}-I_{21}}$$

$$R_2: R_{23,14}=\frac{V_{2(14)}-V_{1(14)}}{I_{23}-I_{32}}$$

$$R_3: R_{34,21}=\frac{V_{2(21)}-V_{1(21)}}{I_{34}-I_{43}}$$

$$R_4: R_{41,32}=\frac{V_{2(32)}-V_{1(32)}}{I_{41}-I_{14}} \quad (2.3)$$

These four series measurements enable the calculation of the thin-film resistivity (ρ). For each configuration, the resistivity was derived according to

$$\rho_1=\frac{\pi}{\ln 2}\cdot\frac{R_1+R_2}{2}=f\left[\frac{R_1}{R_2}\right]d \quad (2.4)$$

where d denotes the film thickness and f is the geometrical correction factor, which approaches unity for an ideally symmetric electrode arrangement. Four possible resistivity sets—ρ1(R1, R2), ρ2(R2, R3), ρ3(R3, R4), and ρ4(R4, R1)—were obtained,

and the averaged value was used to represent the intrinsic resistivity of the film.

In this thesis, all electrical conductivity measurements for the active layer of the all-solid-state thermal transistor were performed using this four-electrode method to ensure high measurement accuracy and reproducibility.

2.3.2. Thermopower

Thermopower (S) is a fundamental electrical transport parameter that provides insight into the electronic density of states (DOS) in the vicinity of the Fermi level (EF). In thermoelectric materials, thermopower is particularly important because it sensitively reflects changes in the electronic structure and carrier transport mechanisms.

For a single-band semiconductor, thermopower can be described by the Mott equation:[8]

$$S = \frac{\pi^2}{3}\frac{{k_B}^2 T}{e}\left\{\frac{d[\ln(\sigma(E))]}{dE}\right\}_{E=E_F} = \frac{\pi^2}{3}\frac{{k_B}^2 T}{e}\left\{\frac{1}{n}\cdot\frac{dn(E)}{dE}+\frac{1}{\mu}\cdot\frac{d\mu(E)}{dE}\right\}_{E=E_F} \quad (2.5)$$

where k_B is the Boltzmann constant, e is the elementary charge, n is the carrier concentration, and μ is the carrier mobility. This expression indicates that thermopower is governed by the energy dependence of both the carrier density and mobility near the Fermi level, and therefore effectively represents the slope of the DOS around EF.

In this study, thermopower measurements were employed to monitor variations in the electronic structure of the thin-film materials. The thermopower of the films was measured using a conventional steady-state method. The sample was positioned between two Peltier devices separated by approximately 3 mm. A temperature gradient was

generated by applying forward and reverse currents to the Peltier elements.

The temperature difference (ΔT) across the sample and the corresponding thermoelectromotive force (ΔV) were recorded simultaneously. Thermopower was determined from the slope obtained by linear fitting of the ΔV–ΔT relationship, ensuring reliable evaluation of the intrinsic thermoelectric response of the films.

2.4. Thermal conductivity

2.4.1. AC calorimetric measurement

For thin films with a thickness on the order of several hundred nanometers, the surface-to-volume ratio is extremely large. As a result, heat loss due to thermal radiation becomes significant, even when measurements are performed under vacuum conditions. In such cases, conventional steady-state thermal conductivity measurements based on applying a constant heat flux and evaluating the temperature difference between two ends of the sample cannot provide reliable results, because the measured temperature gradient is strongly affected by uncontrolled heat dissipation.

To overcome this limitation, the in-plane thermal conductivity of freestanding $Ba_{1/3}CoO_2$(BCO) sheets was measured using an AC calorimetric method, which is known to be insensitive to radiative and parasitic heat losses. This technique allows accurate evaluation of thermal diffusivity by analyzing the phase and amplitude of temperature oscillations induced by periodic heating.[9-10]

In this method, the sample was fixed between a Peltier device and a Cu plate using Ag paste. A sinusoidal heating and cooling signal was applied to the Peltier device, generating a thermal wave that propagates along the in-plane direction of the sample. Consequently, a corresponding local temperature wave, $T(x, t)$, is observed at position x from the edge of the device at time t. The $T(x, t)$ is determined based on the conventional heat conduction theory.

$$c\frac{\partial T}{\partial t} + \frac{2\delta}{d}(T - T_0) - \kappa\frac{\partial^2 T}{\partial x^2} = \frac{Q_0 e^{i\omega t}}{d} \tag{2.6}$$

Where c is the specific heat per sample volume. The second term from the left represents the thermal conduction to the heat bath. where δ is the thermal conductance per unit area between the Peltier device and the bottom of the sample, d is the sample thickness, and T_0 is the temperature of the Peltier element surface. The right side represents the external heat flux, where $Q_0 e^{i\omega t}$ is the AC heat flux per unit area from the Peltier device to the sample.

A wave-form solution for Eq. (2.6) is given by,

$$T(x, t) = \Delta T(x)\sin\big(2\pi f t - \phi(x)\big) + T_0 \tag{2.7}$$

The amplitude (ΔT) and phase (ϕ) are given by,

$$\Delta T = \frac{Q_0}{2\omega c d\sqrt{1 + (\omega\tau)^2}} e^{-k_a x} \tag{2.8}$$

$$\phi = k_p x + \phi_0 \tag{2.9}$$

k_a and k_p can be calculated from the amplitude and phase of the observed temperature oscillation as

$$k_a = -\frac{d(ln\Delta T(x))}{dx} = -\frac{ln\Delta T(x_2) - ln\Delta T(x_1)}{x_2 - x_1} \tag{2.10}$$

$$k_p = \frac{d(\phi(x))}{dx} = \frac{\phi(x_2) - \phi(x_1)}{x_2 - x_1} \tag{2.11}$$

Using the experimental data, k_a and k_p are obtained, and the frequency dependent thermal diffusivities D_a and D_p are given by,

$$D_i = \frac{\omega}{2k_i^2} \ (i = a \text{ and } b) \tag{2.12}$$

The thermal diffusivity (D) is obtained as

$$D = \sqrt{D_a D_p} \tag{2.13}$$

Finally, the thermal conductivity (κ) is obtained as $\kappa = D \cdot \rho \cdot C_p$, where ρ denotes the density, κ stands for thermal conductivity, and C_p represents the specific heat capacity.

2.4.2. Time-domain thermoreflectance (TDTR)

The time-domain thermoreflectance (TDTR) method is an optical pump–probe technique widely used to characterize thermal transport properties of thin films and nanostructured materials. The fundamental principle of TDTR is based on the linear relationship between the surface reflectivity of a material and its temperature, which is quantified by the photothermal reflectance coefficient (dR/dT). By monitoring changes in surface reflectivity induced by transient heating, TDTR enables indirect determination of temperature evolution and heat conduction processes on ultrafast timescales ranging from femtoseconds to nanoseconds.

In a typical TDTR measurement, a femtosecond pulsed laser is divided into two beams:

a pump beam and a probe beam. The pump beam is focused onto the sample surface to induce a transient temperature rise, while the probe beam is directed onto the same position with a controlled time delay relative to the pump beam. This time delay is precisely adjusted using a long-travel mechanical delay stage. As the delay stage scans, the probe beam detects the time-dependent change in surface reflectivity, which reflects the transient temperature response of the sample surface.

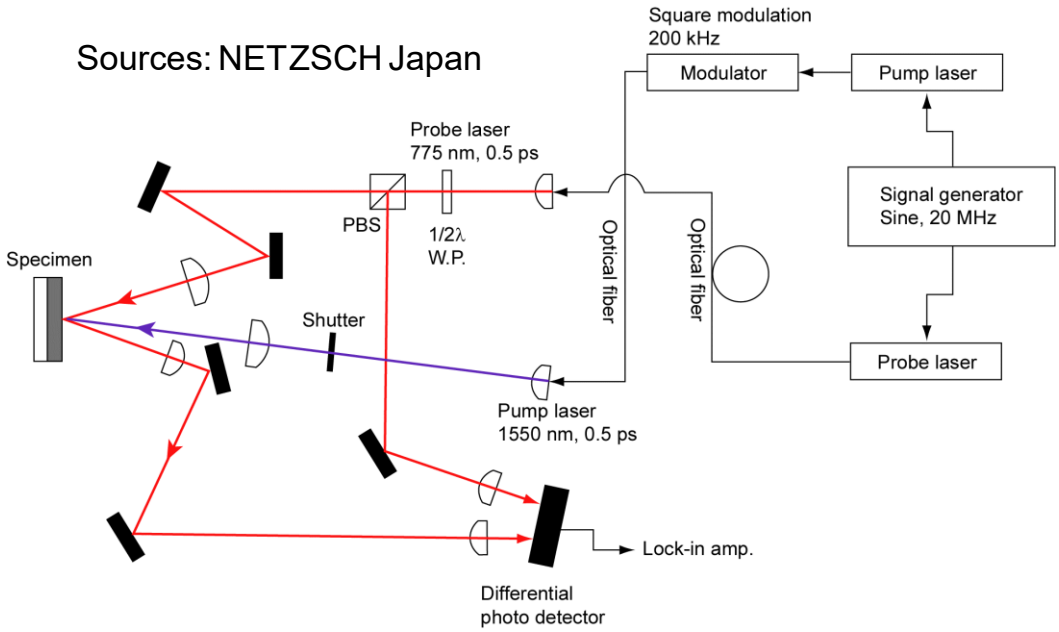

Figure 2-3. Geometric relationship of Bragg's law

By recording the reflectivity change as a function of time delay, the surface temperature evolution can be reconstructed indirectly. The experimentally obtained temperature decay curve is subsequently fitted using an appropriate thermal transport model to extract the thermal properties of the sample. A schematic illustration of the TDTR measurement setup used in this study is shown in **Figure 2-3**.

For TDTR measurements of nanostructured materials, a thin metallic transducer layer is commonly deposited on the sample surface. In this thesis, a Pt layer with a thickness of several tens of nanometers was employed. This metallic layer serves two essential functions: it efficiently absorbs the incident laser energy and converts it into heat, and it acts as a sensitive temperature sensor due to its linear reflectivity–temperature relationship. At very short timescales, the thermal transport within the metallic layer deviates from classical Fourier heat conduction, reflecting non-equilibrium energy absorption and redistribution processes intrinsic to ultrafast laser heating.

The detected TDTR signal consists of an in-phase component (Vin) and an out-of-phase component (Vout), which together form a complex signal expressed as

$$V = V_{in} + iV_{out} \tag{2.6}$$

where i is the imaginary unit. From these components, the amplitude (A) and phase (φ) of the thermal reflection signal are defined as

$$A = \sqrt{V_{in}{}^2 + V_{out}{}^2}$$
$$\varphi = \tan^{-1}(V_{out}/V_{in}) \tag{2.7}$$

Here, A represents the signal amplitude, while φ corresponds to the phase signal. Compared to the amplitude signal, the phase signal is less sensitive to experimental noise, mechanical vibrations, and background fluctuations. Therefore, in this thesis, the phase signal was primarily used to fit the thermal conductivity of the samples.

The TDTR data analysis and thermal simulations were performed using the packaged software provided by the instrument manufacturer, PicoTherm Corporation (currently NETZSCH), ensuring consistent and reliable extraction of thermal transport parameters.

References

[1] Chrisey, D. B. *et al.*, Pulsed laser deposition of thin films. (1994).

[2] Norton, D. P., Synthesis and properties of epitaxial electronic oxide thin-film materials. *Mater. Sci. Eng. R Rep.* **43**, 139-247 (2004).

[3] Nellist, P. *et al.*, The principles and interpretation of annular dark-field Z-contrast imaging. In *Advances in imaging and electron physics*, Elsevier: 2000; Vol. 113, pp 147-203.

[4] Hillyard, S. *et al.*, Annular dark-field imaging: resolution and thickness effects. *Ultramicroscopy* **49**, 14-25 (1993).

[5] Findlay, S. *et al.*, Dynamics of annular bright field imaging in scanning transmission electron microscopy. *Ultramicroscopy* **110**, 903-923 (2010).

[6] Phillips, P. J. *et al.*, Atomic-resolution defect contrast in low angle annular dark-field STEM. *Ultramicroscopy* **116**, 47-55 (2012).

[7] Egerton, R. F., Electron energy-loss spectroscopy in the TEM. *Rep. Prog. Phys.* **72**, 016502 (2009).

[8] Cutler, M. *et al.*, Observation of Anderson localization in an electron gas. *Phys. Rev.* **181**, 1336 (1969).

[9] Hatta, I. *et al.*, Thermal diffusivity measurement of thin films by means of an ac calorimetric method. *Rev. Sci. Instrum.* **56**, 1643-1647 (1985).

[10] Kawasaki, S. *et al.*, Thermal Diffusivity of the Mott Insulator Ca_2RuO_4 in a Non-equilibrium Steady State. *J. Phys. Soc. Jpn.* **90**, (2021).

Chapter 3. Freestanding $Ba_{1/3}CoO_2$ Single-Crystalline Films: Fabrication and Thermoelectric Properties

3.1. Objective of this chapter

In Chapter 1, I already mentioned that we realized the highest *ZT* value of $Ba_{1/3}CoO_2$(BCO) among reliable oxide thermoelectric materials. BCO shows metallic p-type conductivity up to 600 °C in air. Recently, we found that BCO epitaxial films exhibit a rather large *ZT* of 0.11 at room temperature[1] and 0.55 at 600 °C.[2] These values are the highest among reliable oxide thermoelectric materials and are comparable to those of commercially available p-type PbTe and SiGe.[3] However, there is a serious drawback in BCO epitaxial films. Since the substrate (α-Al_2O_3 or YSZ) is an electrical insulator, the overall *ZT* including the substrate is extremely low. Thus, the fabrication of bulk ceramics or single crystalline BCO is crucially demanded. In 2014, Liu *et al*. fabricated BCO ceramics and measured the *ZT* at several temperatures.[4-5] But the *ZT* of the ceramics was only 0.005 at room temperature, more than one order lower than that of epitaxial films, probably due to the suppression of electron transport at the grain boundaries.

Recently, peeling off of the epitaxial films of perovskite oxides has been energetically studied.[6-8] As the sacrificial layer, water-soluble $Sr_3Al_2O_6$ films are epitaxially grown on the substrate before the perovskite oxide film growth, then, the perovskite oxide film is peeled off by dissolving the sacrificial layers in water.[6] In 2006, Ohta *et al*. reported that $Na_{3/4}CoO_2$ epitaxial film grown on (0001) α-Al_2O_3 is peeled off by immersing it in water because there is a water-soluble amorphous Na-Al-O layer spontaneously formed at the

interface between $Na_{3/4}CoO_2$ epitaxial film and α-Al_2O_3 substrate.[9] Thus, the amorphous Na-Al-O layer plays as the sacrificial layer. In the case of BCO epitaxial films, there is an amorphous Ba-Al-O layer spontaneously formed at the interface between BCO epitaxial film and α-Al_2O_3 substrate.[1] Therefore, we expected that the amorphous Ba-Al-O layer plays as the sacrificial layer and freestanding BCO epitaxial film would be obtained.

Here, we show that freestanding BCO single crystalline films were fabricated by peeling off the BCO epitaxial films from the substrate. We fabricated BCO epitaxial films and immersed them in 40 °C hot water for several ten minutes. After that, the BCO epitaxial film was spontaneously peeled off and floated on the surface of the water like seaweed. We measured and analyzed the crystal structure, chemical composition, and thermoelectric properties before and after peeling off, and realized that there was no significant difference. The present results provide a useful way to fabricate freestanding oxide single crystalline films for thermoelectrics.

3.2. Experimental

First, CoO films (thickness: 300 nm, the target thickness of BCO: 600 nm) were heteroepitaxially grown on the substrate at 700 °C in an oxygen atmosphere (10^{-3} Pa) by a pulsed laser deposition technique (KrF excimer laser, ~2 J cm^{-2} $pulse^{-1}$, 10 Hz). BCO epitaxial films were fabricated on (0001) α-Al_2O_3 substrates by reactive solid-phase epitaxy (R-SPE) of $Na_{3/4}CoO_2$ films followed by ion exchange treatment. First, CoO films were heteroepitaxially grown on the substrate at 700 °C in an oxygen atmosphere (10^{-3} Pa) by a pulsed laser deposition technique (KrF excimer laser, ~2 J cm^{-2} $pulse^{-1}$, 10 Hz).

Then, the CoO film was heated with $NaHCO_3$ powder at 750 °C in air. This results in the formation of a $Na_{3/4}CoO_2$ epitaxial film. Then, the Na^+ ions in the resultant films were exchanged with Ba^{2+} ions by heating the $Na_{3/4}CoO_2$ epitaxial films with molten $Ba(NO_3)_2$ and KNO_3 at 500 °C in an alumina crucible for 1 h. During the R-SPE and the ion exchange treatment, a ~10-nm-thick amorphous Ba-Al-O layer formed spontaneously at the interface between the BCO film and the α-Al_2O_3 substrate.[1] Then, we peeled off the BCO epitaxial film from the α-Al_2O_3 substrate as schematically shown in **Figure 3-1a**. First, we immersed the BCO epitaxial film in hot water (40 °C). Before immersing in the water, the BCO epitaxial film was stuck hard to the substrate (**Figure 3-1b**). Several tens of minutes later, the dissolution of the amorphous Ba-Al-O layer and peeling off of the BCO epitaxial film occurred. After that, the peeled-off BCO epitaxial film floated on the surface of the water (**Figure 3-1c**) like seaweed. In order to measure the properties of the peeled-off BCO epitaxial film, we pasted the film onto a glass substrate and dried in air at room temperature (**Figure 3-1d**). Note that the film was flexible when we used thin plastic substrates instead of glass substrates (Data not shown). Crystallographic characteristics including the thickness, orientation, and lattice parameters of the resultant films were analyzed using high-resolution X-ray diffraction (HR-XRD, Cu $K\alpha_1$ radiation, ATX-G, Rigaku Co.). Out-of-plane Bragg diffraction patterns, rocking curves, and X-ray reflection patterns were acquired. The atomic arrangement of the resultant films was visualized using a high-angle annular dark-field scanning transmission electron microscope (HAADF-STEM, ARM-200F, JEOL). The electrical conductivity of the resultant films was measured by the dc four-probe method in the van der Pauw electrode configuration. The thermopower of the resultant films was measured by the conventional steady-state method. The film sample was placed on the gap (~5 mm) between two Peltier

devices. By applying the forward/reverse current to each Peltier device, temperature differences were generated in the sample. We then measured the temperature difference (ΔT) and the thermo-electromotive force (ΔV) simultaneously, and the thermopower was calculated as the linear slope of the $\Delta T - \Delta V$ plot.

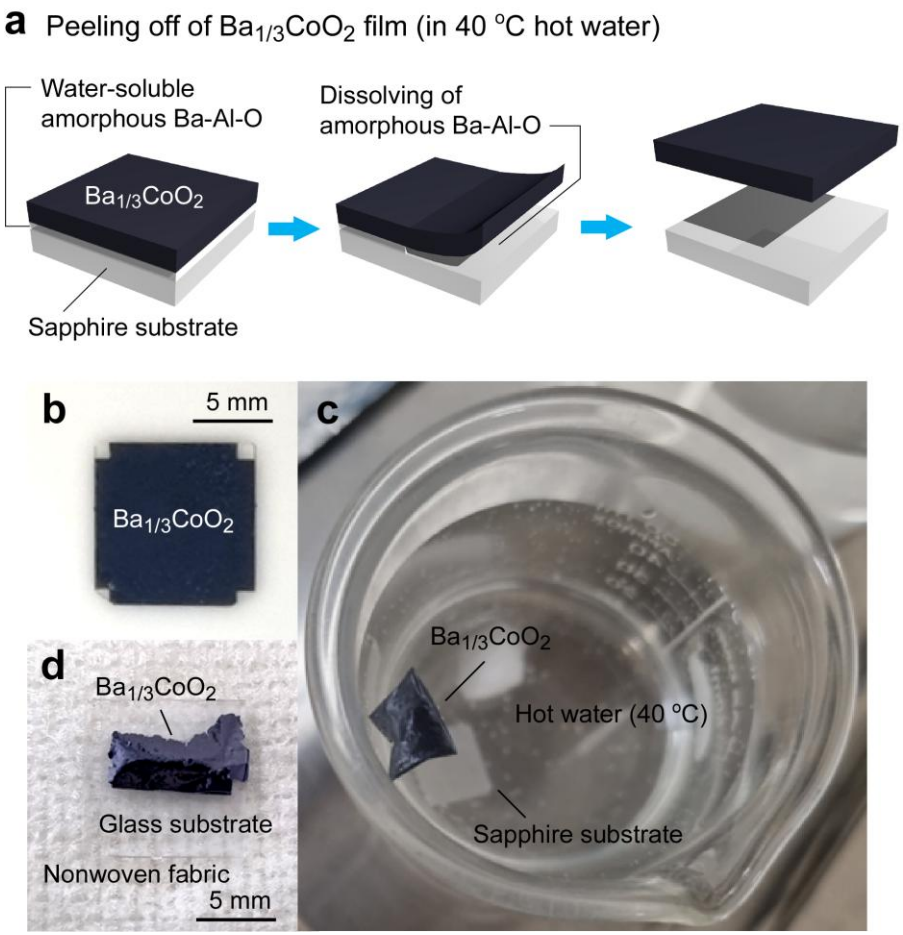

Figure 3-1. Fabrication process of freestanding $Ba_{1/3}CoO_2$ single-crystalline films. (a) Schematic illustration of the peeling-off process of a $Ba_{1/3}CoO_2$ epitaxial film by dissolving the amorphous Ba-Al-O sacrificial layer in 40 °C hot water. (b) Photograph of the as-grown $Ba_{1/3}CoO_2$ epitaxial film on the (0001) α-Al_2O_3 substrate. (c) Photograph of the $Ba_{1/3}CoO_2$ film floating on the water surface after separation in hot water. (d) Photograph of the peeled-off $Ba_{1/3}CoO_2$ film transferred onto a glass substrate.

3.3. Result and discussion

We performed high-resolution X-ray diffraction measurements of the peeled-off BCO epitaxial film. **Figure 3-2** summarizes the out-of-plane XRD pattern of the as-grown and the peeled-off BCO epitaxial films. The peeled-off BCO epitaxial film only shows intense Bragg diffraction peaks of 000*l* BCO (**Figure 3-2c**). The position and the intensity of the Bragg diffraction peaks did not change compared to that of as-grown BCO epitaxial film (**Figure 3-2a**), except the substrate peak disappeared. *c*-axis lattice parameter of the peeled-off BCO epitaxial film was 1.221 nm. The full width at half maximum (FWHM) of the out-of-plane X-ray rocking curve (OXRC) of the 0002 BCO was ~2.0° (**Figure 3-2d**), slightly wider than that of the as-grown film (~1.7°). Compared with a previous report,[1] the FWHM of the OXRC was significantly wider (this work: ~ 2.0°, previous report: ~0.8°), probably because the thickness was 3times greater (this work: 600 nm, previous report: 200 nm). We further measured the chemical composition of the peeled-off BCO epitaxial film by inductively coupled plasma mass spectrometry (ICP-MS) and obtained a Ba/Co ratio of 0.323. These results reveal that the peel-off treatment does not affect the chemical composition and the crystal structure of BCO epitaxial films.

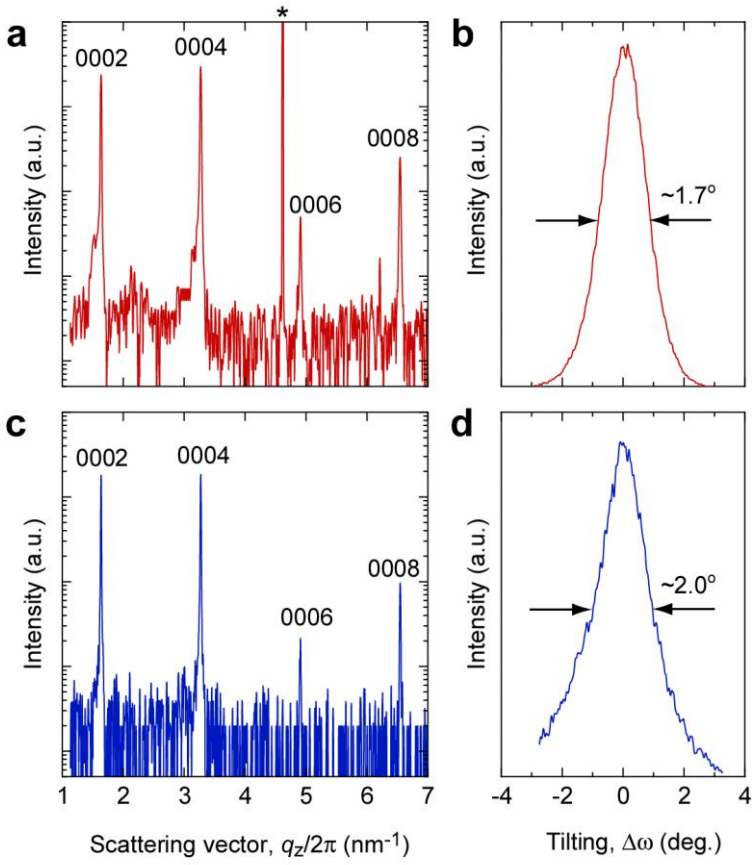

Figure 3-2. X-ray diffraction analysis of $Ba_{1/3}CoO_2$ films before and after peeling-off. (a) Out-of-plane XRD pattern of the as-grown $Ba_{1/3}CoO_2$ epitaxial film on a sapphire substrate. (b) Rocking curve of the 0002 diffraction peak for the as-grown film.(c) Out-of-plane XRD pattern of the peeled-off $Ba_{1/3}CoO_2$ film transferred onto a glass substrate. (d) Rocking curve of the 0002 diffraction peak after peeling-off.

We then performed a microstructure observation of the peeled-off BCO epitaxial film using high-angle annular dark-field (HAADF) scanning transmission electron microscopy (STEM). **Figure 3-3a** shows a cross-sectional HAADF-STEM image of the

peeled-off BCO epitaxial film. The overall thickness of the BCO film was ~600 nm, which is consistent with the designed thickness. **Figure 3-3b** shows a magnified HAADF-STEM image. The incident direction of the e-beam corresponded to [11$\bar{2}$0] of the peeled-off BCO epitaxial film. The crystal structure was composed of alternating CoO_2 (blue-filled circle) and Ba (yellow-filled circle) layers.

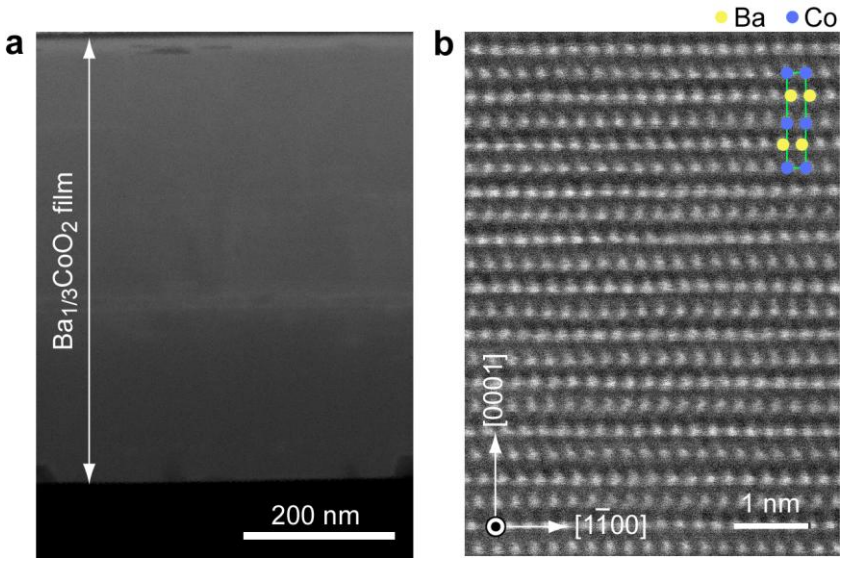

Figure 3-3. Microstructure of the peeled-off $Ba_{1/3}CoO_2$ epitaxial film. (a) Cross-sectional HAADF-STEM image. Microstructure of the peeled-off $Ba_{1/3}CoO_2$ epitaxial film. (a) Cross-sectional HAADF-STEM image. Overall thickness is ~600 nm. (b) Magnified HAADF-STEM image. A layered crystal structure composed of alternating CoO_2 (blue-filled circle) and Ba (yellow-filled circle) layers along the *c*-axis is clearly seen.

Next, we measured the thermoelectric properties of the freestanding BCO single crystalline films in the in-plane direction. The room-temperature electrical conductivity (σ) of the as-grown BCO film was ~1100 S cm^{-1}, while that of freestanding BCO single crystalline film was ~1000 S cm^{-1}. Both films exhibited metallic conductivity, in which

the σ increased as the temperature decreased (**Figure 3-4a**). Note that increased the σ of the freestanding single-crystalline film is significantly lower than that of the previous report (σ: 2300 S cm^{-1}).[1] This may be due to that the crystalline tilting of the freestanding BCO single crystalline film is larger than that of the previous report, and therefore grain boundary scattering contributes significantly. The room-temperature S of the as-grown BCO film was +76 μV K^{-1}, while that of the freestanding BCO single crystalline film was +73 μV K^{-1}. The S values of both films gradually decreased as the temperature decreased (**Figure 3-4b**), demonstrating that the peeling off treatment does not affect the thermoelectric properties.

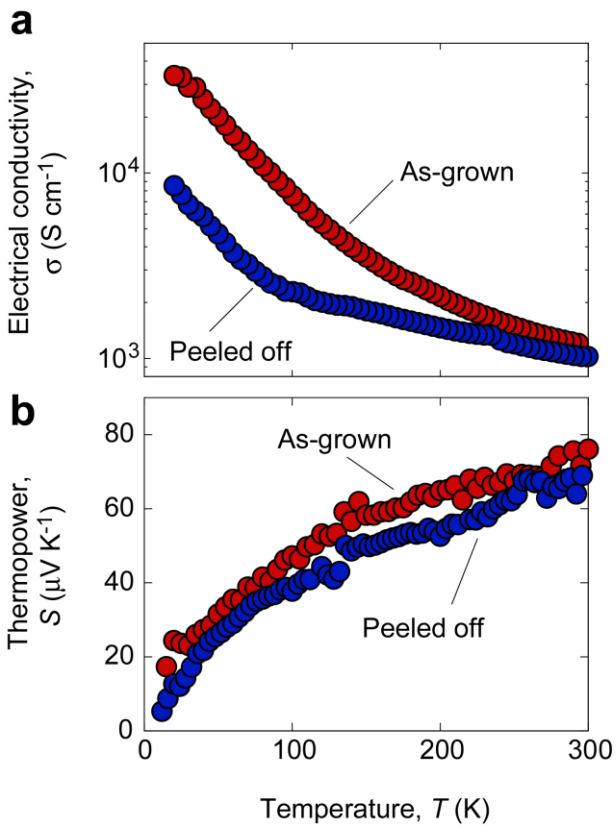

Figure 3-4. Thermoelectric properties. Temperature dependence of (a) electrical conductivity and (b) thermopower for the $Ba_{1/3}CoO_2$ films before and after peeled-off. The room-temperature σ of the as-grown $Ba_{1/3}CoO_2$ film was ~1100 S cm^{-1}, while that of after peeled-off was ~1000 S cm^{-1}. Both films exhibited metallic conductivity. The room-temperature *S* of the as-grown film was +76 μV K^{-1}, while that of after peeled-off was +73 μV K^{-1}. The S values of both films gradually decreased as the temperature decreased, demonstrating that the peeling-off treatment does not affect the thermoelectric properties.

Finally, we measured the thermal conductivity (κ) of the freestanding BCO single crystalline films. κ is expressed by $\kappa = C_p \cdot \rho \cdot D$, where C_p is the specific heat capacity, ρ is the bulk density, and D is the thermal diffusivity. Since C_p (0.44 J g^{-1} K^{-1}) and ρ (5.36 g cm^{-3}) at room temperature are known, we measured the D of the freestanding BCO single crystalline films at room temperature using the AC calorimetric method.[10-11] First, we fixed the sample between a Peltier device and a Cu plate using Ag paste (**Figure 3-5**).

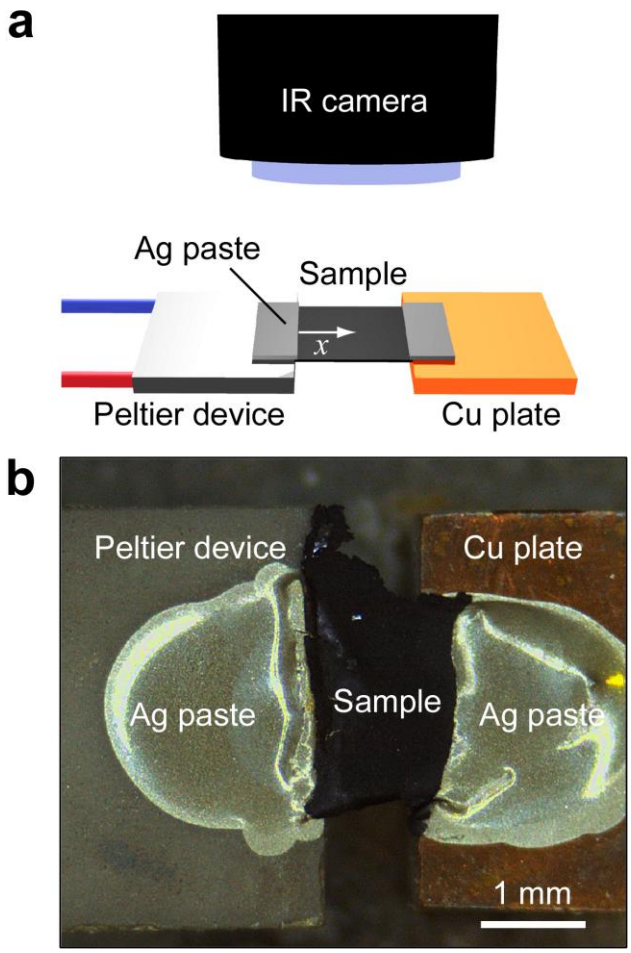

Figure 3-5. Measurement setup for the In-plane thermal diffusivity of the freestanding $Ba_{1/3}CoO_2$ single crystalline films. (a) Schematic illustration. (b) Photograph of the equipment.

Then, we applied AC heat flux to the sample using the Peltier device and measured the temperature at the position x using the IR camera. **Figures 3-6a** and **3-6b** illustrate $T(x, t)$ for a range of x values from 0.1 mm to 0.5 mm, corresponding to frequencies of 0.10 Hz and 0.30 Hz.

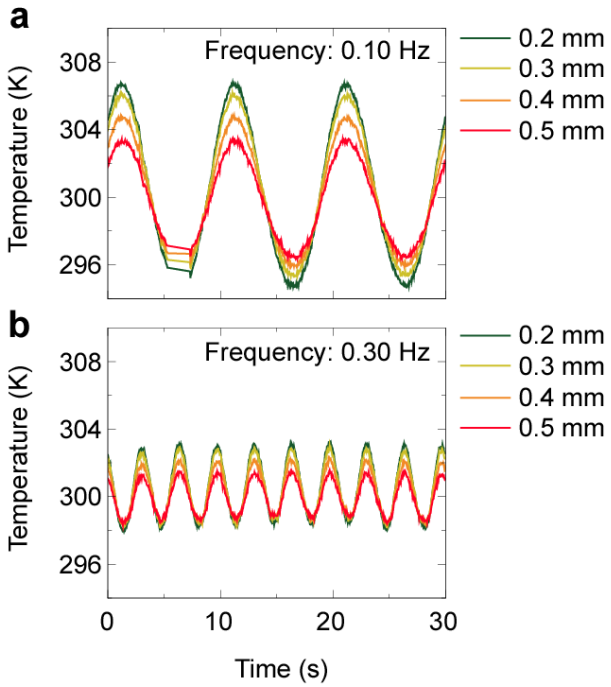

Figure 3-6. Time-dependent temperature at four points for ac thermal frequencies of (a) 0.10 Hz and (b) 0.30 Hz.

To determine the amplitude (ΔT) and phase difference ($\Delta\phi$) at various positions and frequencies, we employ Eq. 2.7 and perform fitting procedures. The resulting values of ΔT and $\Delta\phi$ are then presented as functions of x in **Figs 3-7a** and **3-7b**, respectively.

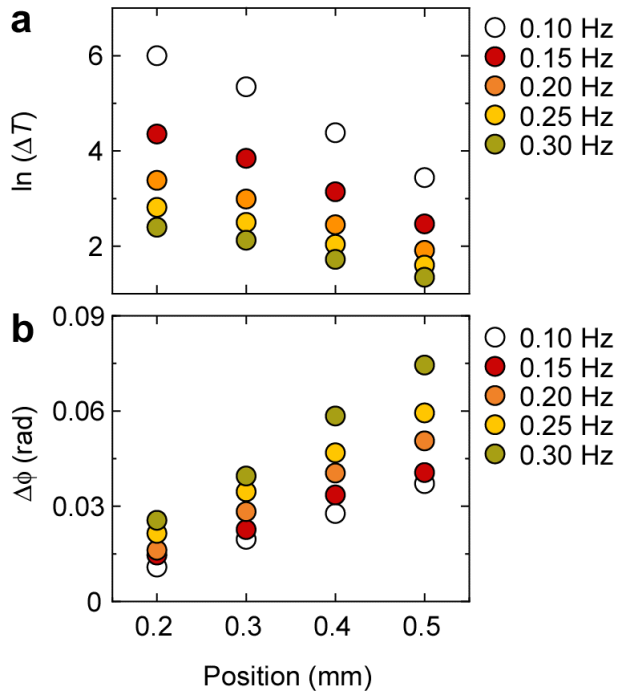

Figure 3-7. The amplitude of the temperature oscillation is represented in (a), and the phase is shown in (b) as a function of position *x*.

By applying Eqs. (2.10) and (2.11) to the experimental data shown in Fig. 3-7, the parameters k_a and k_p were obtained. Using these parameters, the room-temperature thermal diffusivity of the BCO single-crystalline film was determined to be 1.45 mm^2/s, as shown in **Figure 3-8**. Consequently, the obtained κ for the freestanding BCO single crystalline films was determined using a straightforward equation ($\kappa = D \cdot \rho \cdot C_p$), where ρ denotes the density, κ stands for thermal conductivity, and C_p represents the specific heat capacity. By using a bulk density (ρ) value of 5.36 g cm^{-3} and a C_p value of 0.44 J g^{-1} K^{-1}, we calculated the in-plane κ to be 3.45 W m^{-1} K^{-1}. This value agreed well with the as-grown film (~3.2 W m^{-1} K^{-1})[19]. For comparison, we measured the κ of a freestanding $Sr_{1/3}CoO_2$ single crystalline film, which was prepared in a similar manner as

BCO. Consistent with the as-grown film (~4.4 W m^{-1} K^{-1}),[1] the obtained κ was ~4.1 W $m^{-1}K^{-1}$. From these results, we judged that we successfully fabricated freestanding BCO single crystalline films that exhibit good thermoelectric *ZT* of 0.047 at room temperature.

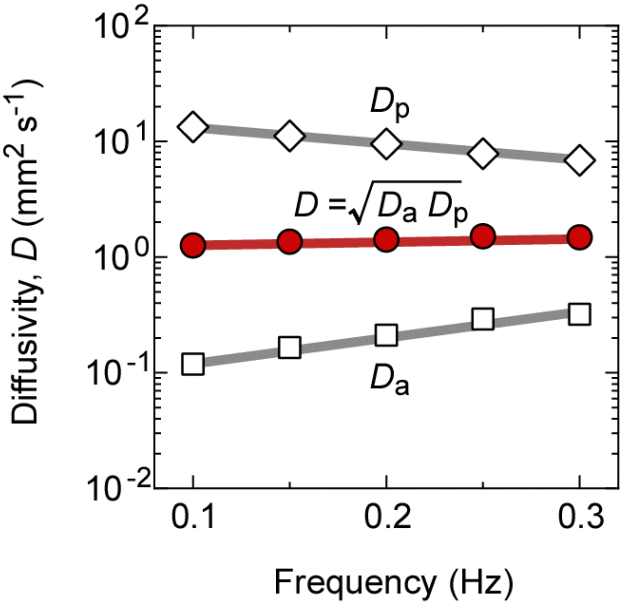

Figure 3-8. In-plane thermal diffusivity (*D*) of the freestanding $Ba_{1/3}CoO_2$ single crystalline films. The *D* values were obtained as $(D_a \cdot D_p)^{1/2}$.

Here, we would like to summarize the thermoelectric properties of the freestanding BCO single crystalline films (**Table 3-1**). From these results, we judged that we successfully fabricated freestanding BCO single crystalline films that exhibit thermoelectric *ZT* of 0.047 at room temperature. Compared to the previous report (BCO single crystalline films on (0001) α-Al_2O_3 substrate), the *ZT* of present freestanding BCO single crystalline films is significantly lower due to lower σ. Except for σ, the thermoelectric properties of the freestanding BCO single crystalline films are similar to the previous report. Since grain boundary scattering dominantly occurs at lower temperatures, the larger grain boundary angle of the freestanding BCO single crystalline film suppresses the σ. Due to the similar origin, the σ of the BCO films grown on YSZ substrates showed lower σ (1,100 S cm^{-1}) than that of BCO films on (0001) α-Al_2O_3 substrate (2,300 S cm^{-1}) at room temperature. Although the *ZT* of the BCO films grown on YSZ substrates was lower (0.058) than that of BCO films on (0001) α-Al_2O_3 substrate (0.11) at room temperature, it increased with temperature and reached 0.55 at 600 °C because the grain boundary scattering becomes less dominant. Therefore, we expect that the freestanding BCO single crystalline film exhibits high *ZT* at higher temperatures.

	This work	Takashima et al.[1]	Zhang et al.[2]
σ (S cm^{-1})	1000	2300	1100
S (μV K^{-1})	73	72	75
κ (W m^{-1} K^{-1})	3.4	3.3	3.2
ZT	0.047	0.11	0.058

Table 3-1. Thermoelectric Properties of the Freestanding Ba1/3CoO2 Single-Crystalline Films at Room Temperature. The data of the previous reports are also shown for comparison.

Finally, we discuss κ. In the previous report, we measured the κ of the BCO epitaxial films using the time-domain thermoreflectance (TDTR) method.[12] Because BCO epitaxial films exhibit good electron transport properties in the in-plane direction, κ must be measured in the in-plane direction to extract *ZT*. Previously, we used the TDTR method to measure the out-of-plane κ of the BCO epitaxial films with two different crystallographic orientations: a c-axis orientation and a 55°-inclined c-axis.[1-2] Using these two out-of-plane κ data, we extracted the in-plane κ theoretically. It is very important that the κ value of the freestanding BCO single-crystalline film measured using the AC calorimetric method agrees well with the κ value of the BCO epitaxial film measured using the TDTR method.

3.4. Conclusion

In summary, we successfully fabricated freestanding BCO single-crystalline films by peeling off BCO epitaxial films from the substrate. We immersed BCO epitaxial films in 40 °C hot water for several tens of minutes to peel off the films. The crystal structures and thermoelectric properties of the peeled films were maintained. The present results provide a useful method for fabricating freestanding single-crystalline oxide films for thermoelectrics. We showed that freestanding BCO single crystalline films were fabricated by peeling off the BCO epitaxial films from the substrate. We fabricated BCO epitaxial films and immersed them in 40 °C hot water for several ten minutes. After that, the BCO epitaxial film was spontaneously peeled off and floated on the surface of the water like seaweed. We measured and analyzed the crystal structure, chemical composition, and thermoelectric properties before and after peeling off, and realized that there was no significant difference. The present results provide a useful way to fabricate

freestanding oxide single crystalline films for thermoelectrics. Although the intrinsic thermoelectric performance of BCO was verified in freestanding single-crystalline form, a significant discrepancy remains between epitaxial films and bulk ceramics. In particular, previously reported bulk samples exhibit substantially degraded *ZT* values. Therefore, understanding the origin of this performance gap is essential for practical scale-up, which is addressed in the following chapter.

References

[1] Takashima, Y. *et al.*, Layered cobalt oxide epitaxial films exhibiting thermoelectric *ZT* = 0.11 at room temperature. *J. Mater. Chem. A* **9**, 274-280 (2021).

[2] Zhang, X. *et al.*, $Ba_{1/3}CoO_2$: A Thermoelectric Oxide Showing a Reliable *ZT* of approximately 0.55 at 600 °C in Air. *ACS Appl. Mater. Interfaces* **14**, 33355-60 (2022).

[3] Snyder, G. J. *et al.*, Complex thermoelectric materials. *Nat. Mater.* **7**, 105-114 (2008).

[4] Liu, J. *et al.*, Synthesis and physical properties of layered Ba_xCoO_2. *Dalton Trans.* **43**, 15414-15418 (2014).

[5] Liu, J. *et al.*, High-temperature thermoelectric properties of layered Ba_xCoO_2. *Scr. Mater.* **100**, 63-65 (2015).

[6] Lu, D. *et al.*, Synthesis of freestanding single-crystal perovskite films and heterostructures by etching of sacrificial water-soluble layers. *Nat. Mater.* **15**, 1255-1260 (2016).

[7] Kum, H. S. *et al.*, Heterogeneous integration of single-crystalline complex-oxide membranes. *Nature* **578**, 75-81 (2020).

[8] Gong, L. *et al.*, Significant Suppression of Cracks in Freestanding Perovskite Oxide Flexible Sheets Using a Capping Oxide Layer. *ACS Nano* **16**, 21013-21019 (2022).

[9] Ohta, H. *et al.*, Surface Modification of Glass Substrates for Oxide Heteroepitaxy: Pasteable Three-Dimensionally Oriented Layered Oxide Thin Films. *Adv. Mater.* **18**, 1649-1652 (2006).

[10] Hatta, I. *et al.*, Thermal diffusivity measurement of thin films by means of an ac calorimetric method. *Rev. Sci. Instrum.* **56**, 1643-1647 (1985).

[11] Ohta, S. *et al.*, Grain Size Dependence of Thermoelectric Performance of Nb-Doped $SrTiO_3$ Polycrystals. *J. Ceram. Soc. Jpn.* **114**, 102-105 (2006).

[12] Cahill, D. G., Analysis of heat flow in layered structures for time-domain thermoreflectance. *Rev. Sci. Instrum.* **75**, 5119-5122 (2004).

Chapter 4. High-Temperature Decomposition Behavior and Its Impact on Electron Transport in $Ba_{1/3}CoO_2$

4.1. Objective of this chapter

In the last Chapter, I realized that the crystal structure and thermoelectric properties of freestanding $Ba_{1/3}CoO_2$ (BCO) were maintained, resulting in excellent reproducibility and no performance degradation. Furthermore, cross-validation between heteroepitaxial and free-standing films confirmed the intrinsic properties and reliability of BCO, highlighting its potential for integration into practical thermoelectric devices. These characteristics make BCO a strong candidate for high-temperature thermoelectric modules, and its free-standing form factor may allow future exploration toward flexible architectures.

Despite these outstanding properties of BCO, its scale-up remains a key challenge for practical applications. Liu *et al*. reported that attempts to fabricate bulk BCO ceramics have resulted in significantly degraded performance, with *ZT* 0.014 at room temperature and 0.15 at 520 °C, much lower than epitaxial BCO thin film.[1] In particular, the electrical conductivity of bulk ceramics is 300 S cm^{-1} at room temperature, which corresponds to about 20% of that of the thin films (~1500 S cm^{-1}). This degradation is primarily due to thermal decomposition occurring during the high-temperature sintering process required

for densification. While oxide ceramics typically require sintering above 1000 °C, BCO become structurally unstable above 650−700 °C.[2-3] Although the structural instability of BCO at high temperatures has been qualitatively discussed in previous reports, the mechanism by which phase decomposition leads to thermoelectric degradation has not been fully clarified.

In this study, we elucidated the mechanism of thermoelectric properties degradation due to structural decomposition of BCO at high temperatures in air. As shown in **Figure 4-1**, BCO is structurally very stable up to 700 °C, exhibiting metallic conduction and maintaining consistent thermoelectric properties, with $\sigma \approx 1500$ S cm^{-1}, $S \approx 95$ μV K^{-1}, $\kappa \approx 3.3$ W m^{-1} K^{-1} and ZT value of 0.12 at room temperature. Above 700 °C, BCO undergoes thermal decomposition into three distinct phases: $BaCoO_x$ (x = 3 and 2.6), and Co_3O_4. Among these, $BaCoO_{2.6}$ acts as a conductor,[4] while Co_3O_4 is an electrical insulator.[5] $BaCoO_3$ exhibits one-dimensional conduction along the c-axis,[6-7] but it does not contribute significantly to in-plane electron transport. When the volume fraction of $BaCoO_{2.6}$ exceeds the percolation threshold, the decomposed film shows percolation electron transport, characterized by σ of 100 S cm^{-1} and S of 115 μV K^{-1}. Due to enhanced phonon scattering at the grain boundaries formed during phase decomposition, the thermal conductivity decreases to 2.3 W m^{-1} K^{-1}, resulting in a substantial reduction in ZT to about 0.017 at room temperature. With increasing temperature, $BaCoO_{2.6}$ is oxidized to $BaCoO_3$,[8] reducing its volume fraction below the percolation threshold.

Consequently, the σ rapidly decreases while the S increases. Such transport behavior is typical percolation and is well reproduced by the generalized effective medium theory (GEMT). Above 980 °C, $BaCoO_x$ (x = 3 and 2.6) and Co_3O_4 undergo reduction, leading to the formation of insulating $BaCoO_{2.2}$ and CoO.[5, 9] As a result, the mixture no longer exhibits electrical conductivity.

We clearly identify the key degradation mechanism in BCO: phase decomposition, which drives a transition in conduction from metallic to percolation and eventually to insulating behavior at elevated temperatures. These results reveal that low-temperature sintering strategies are essential to preserve the functional properties of BCO for thermoelectric applications. Moreover, the redox behavior of decomposed BCO may offer potential for future energy-related applications, such as solid oxide fuel cells.

RT ~ 675 °C	700 ~ 960 °C	980 °C ~
$Ba_{1/3}CoO_2$ single phase	$BaCoO_{2.6}$ / $BaCoO_3$ / Co_3O_4	$BaCoO_{2.2}$ / CoO
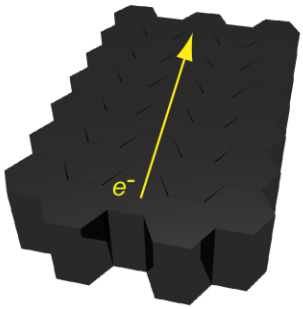	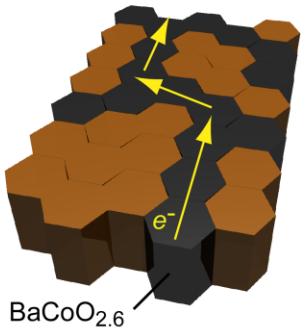	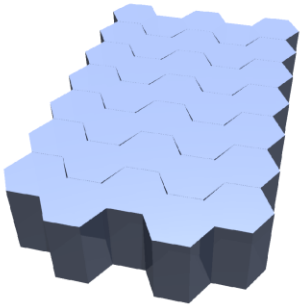
Metallic conduction	Percolation conduction	Insulating
σ ~ 1500 S/cm	σ ~ 100 S/cm	———
S ~ +95 μV/K	*S* ~ +115 μV/K	———
κ ~ 3.3 W/mK	κ ~ 2.3 W/mK	———
ZT (300 K) ~ 0.12	*ZT* (300 K) ~ 0.017	———

Figure 4-1. Schematic change in the electron conduction of $Ba_{1/3}CoO_2$ upon decomposition into $BaCoO_x$ (x = 3, 2.6, and 2.2) and Co_3O_4 at elevated temperatures. (Left) Below 700 °C, single phase $Ba_{1/3}CoO_2$ exhibits metallic conduction. The electrical conductivity (σ) is 1500 S cm^{-1} and thermopower (S) is 95 μV K^{-1}. (center) Above 700 °C, $Ba_{1/3}CoO_2$ decomposes into three phases including $BaCoO_{2.6}$, $BaCoO_3$, and Co_3O_4. $BaCoO_{2.6}$ is a conductor, whereas Co_3O_4 is an insulator. the mixture shows electron conduction with σ of ~100 S cm^{-1} and S of 115 μV K^{-1}. (right) Above 980 °C, reduction of $BaCoO_x$ and Co_3O_4 occur and insulation $BaCoO_{2.2}$ and CoO form. The mixture does not show electrical conductivity.

4.2. Experimental

Epitaxial (0001) BCO films (~150 nm) were fabricated on (111) YSZ substrates via reactive solid-phase epitaxy (R-SPE) of $Na_{3/4}CoO_2$ films, followed by a barium ion exchange process. The detailed fabrication method for BCO has been explained in the previous Chapter. The BCO films were annealed in air at temperatures ranging from 100 °C to 1000 °C for 30 min to confirm their thermal stability. After each annealing step, I measured the crystallographic structure and thermoelectric properties.

Crystallographic Analyses: The crystallographic structure, orientation, and thickness of the films were analyzed using X-ray diffraction (XRD, Cu $K\alpha_1$ radiation, ATX-G, Rigaku Co.). Out-of-plane and in-plane Bragg diffraction patterns, rocking curves, and grazing incident XRD (GIXRD) patterns were obtained to characterize the structures of the films. The lattice images and atomic arrangements were further visualized using plane-view high-angle annular dark-field scanning transmission electron microscopy (HAADF-STEM, JEM-ARM200F, JEOL Co.) operating at 200 kV and measured electron energy-loss spectroscopy (EELS).

Electrical Conductivity and Thermopower Measurements: The electrical resistivity (ρ) or conductivity ($\sigma = 1/\rho$) of the films was measured at room temperature and low temperatures (25 K ~ 300 K) by the d.c. four probe method with van der Pauw electrode

configuration. Thermopower (S) measurements were performed using a steady-state technique. Custom-built equipment was employed for thermopower measurements.

Thermal conductivity measurements: The cross-plane thermal conductivity (κ) of the BCO films was measured by time-domain thermoreflectance (TDTR, PicoTR, NETZSCH Japan Co.) method at room temperature. A 104-nm-thick Pt was deposited on the resultant film surface by DC sputtering to serve as a transducer. The decay curves of TDTR signals were simulated to obtain κ. The in-plane thermal conductivity ($\kappa_{\parallel}$) of the films was extracted using the following equation as previously reported.[3, 10-11]

$$\kappa_{\mathrm{obsd}} = \sqrt{\kappa_{\parallel}^2 \cos^2\varphi + \kappa_{\perp}^2 \sin^2\varphi}$$

Here, the cross-plane thermal conductivity ($\kappa_{\perp}$) was measured for the film grown on the (111) YSZ substrate, while the inclined thermal conductivity (κ_{obsd}) was obtained from the film grown on the $(11\bar{2}0)$ α-Al_2O_3 substrate, where the CoO_2 layers are tilted by φ = 55° from the surface normal, as confirmed by STEM observations in our previous report.[10]

4.3. Result and discussion

First, (0001)-oriented epitaxial BCO thin films, ~150 nm thick, were fabricated on (111) YSZ substrates by reactive solid phase epitaxy (R-SPE) and Ba ion exchange, and the impact of high-temperature on their structure using X-ray diffraction (XRD) and

thermoelectric properties were systematically investigated. As-grown BCO exhibited only the 000*l* diffraction peak with the 111 YSZ substrate diffraction peak in the out-of-plane XRD pattern. In-plane XRD pattern shows both the arrangement of Ba ions and the lattice structure. The as-grown BCO films exhibited three distinct superlattice peaks: $(11\bar{2}0) \times 1/3$ and 2/3 (hexagonal ordering), and $(11\bar{2}0) \times 1/2$ (orthorhombic ordering), indicating a mixed ordering of Ba ions. The $11\bar{2}0$ diffraction peak is observed together with the 110 YSZ diffraction peak in the in-plane XRD. The calculated lattice constants (a = 0.282 nm, c = 1.225 nm) and the Ba/Co atomic ratio of 0.28 determined by inductively coupled plasma-mass spectrometry (ICP-MS) are in good agreement with the previous report.[10]

In order to clarify the crystal structure evolution of a BCO epitaxial film at high temperatures, we performed XRD measurements after each annealing at elevated temperature in air (**Figure 4-2**). Out-of-plane XRD patterns (**Figure 4-2a**) show that the 0002, 0004, and 0006 diffraction peaks of BCO maintained up to 675 °C (blue), indicating the structural stability of the layered structure. In the in-plane XRD patterns (**Figure 4-2b**), the diffraction peaks remained identical to those of the as-grown BCO up to 650 °C. At 675 °C, however, the 1/3 and 2/3 superlattice peaks disappeared, while the 1/2 peak became more pronounced, indicating a change in the ordering of Ba ions. Similar ion-ordering transitions have also been reported in other A_xCoO_2-type layered cobaltites (A_x = $Ca_{1/3}$, $Sr_{1/3}$, $Ba_{1/3}$). For instance, $Ca_{1/3}CoO_2$ and $Sr_{1/3}CoO_2$ preserve their layered structure but undergo orthorhombic rearrangement of *A*-site cations at 350 °C and 450 °C,

respectively.[10, 12-13] The higher transition temperature observed for BCO is consistent with the greater thermal energy required to migrate the heavier Ba ions compared to Ca and Sr. At 700 °C, irreversible decomposition of BCO into $BaCoO_x$ (x = 3 and 2.6) and Co_3O_4 was observed, accompanied by the disappearance of the BCO diffraction peaks and the emergence of new diffraction peaks (red). In the out-of-plane XRD patterns, the 0001 and 0002 diffraction peaks of $BaCoO_3$ and the $10\bar{1}7$ diffraction peak of $BaCoO_{2.6}$ appeared. In the in-plane XRD patterns, the 1/2 superlattice peak was replaced by two new diffraction peaks, which were identified as the $11\bar{2}0$ of $BaCoO_3$ and $BaCoO_{2.6}$. Moreover, although BCO is decomposed, the Ba/Co ratio remains unchanged as confirmed by ICP-MS.

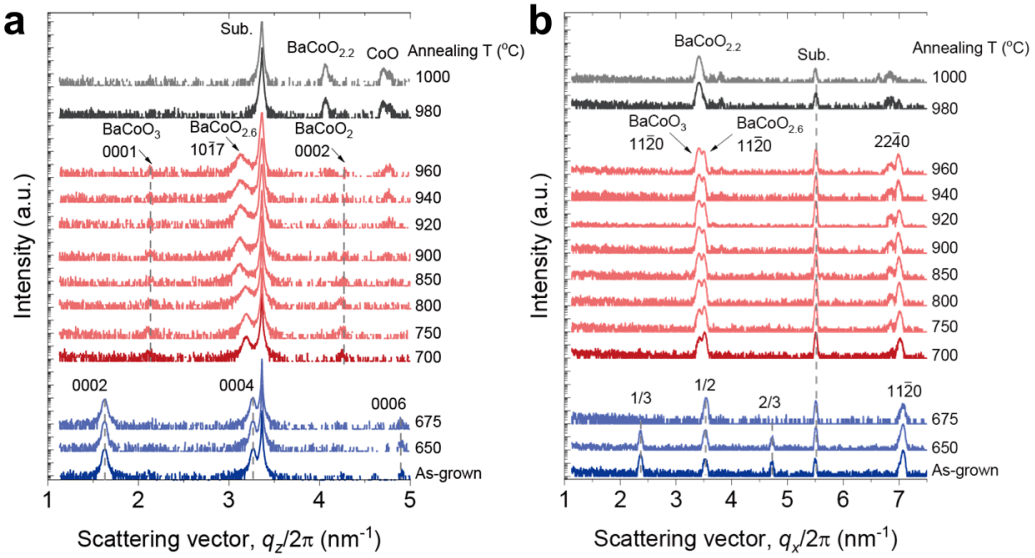

Figure 4-2. Crystal structure evolution of a $Ba_{1/3}CoO_2$ epitaxial film upon decomposition into $BaCoO_x$ (x = 3, 2.6, and 2.2) and Co_3O_4 at elevated temperatures. Change in (a) the out-of-plane and (b) the in-plane XRD patterns after each annealing at elevated temperatures. (a, b) When the annealing temperature is less than or equal to 675 °C, the diffraction peaks of $Ba_{1/3}CoO_2$ are maintained (blue). (a, b) When the annealing temperature is greater than or equal to 700 °C, diffraction peaks of $BaCoO_{2.6}$ and $BaCoO_3$ appear whereas those of $Ba_{1/3}CoO_2$ disappear (red). (b) The peak intensity ratio of $BaCoO_3/BaCoO_{2.6}$ becomes large with increasing the annealing temperature. (a, b) When the annealing temperature is greater than or equal to 980 °C, diffraction peaks of $BaCoO_{2.2}$ appear whereas those of $BaCoO_3$ and $BaCoO_{2.6}$ disappear (gray).

To further characterize the $BaCoO_x$ (x = 3 and 2.6) formed after annealing at 700 °C, in-plane X-ray rocking curves of the $11\bar{2}0$ of $BaCoO_3$ and $BaCoO_{2.6}$ exhibited six-fold symmetry every 60°, verifying their hexagonal crystal structure (**Figure 4-3a**). In addition, grazing incident XRD analysis with an incident angle of 0.5° revealed powder-like diffraction peaks of Co_3O_4, indicating the presence of randomly oriented polycrystalline Co_3O_4 with an average crystallite size of ~20 nm (**Figure 4-3b**).

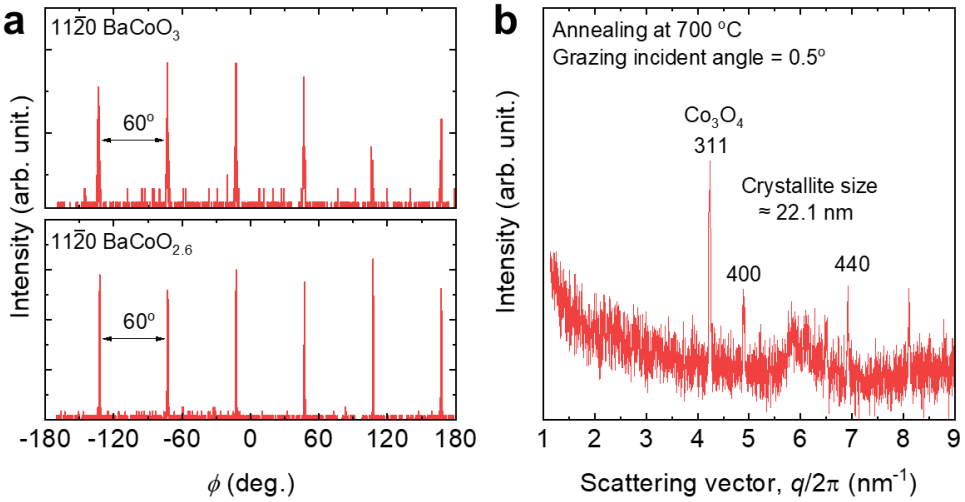

Figure 4-3. Detailed XRD analysis of a $Ba_{1/3}CoO_2$ epitaxial film after annealed at 700 °C. (a) In-plane X-ray rocking curves of $11\bar{2}0$ for $BaCoO_3$ and $BaCoO_{2.6}$. Six-fold symmetry is clearly seen in both cases. (b) Typical GIXRD pattern with an incident angle of X-ray of 0.5°. Powder like diffraction pattern of Co_3O_4 is seen, indicating that the existence of randomly oriented polycrystalline Co_3O_4 with average crystallite size of ~20 nm.

When the annealing temperature is greater than 700 °C, the $11\bar{2}0$ peak intensity ratio of $BaCoO_3/BaCoO_{2.6}$ becomes large with increasing the annealing temperature, indicating progressive oxidation of $BaCoO_{2.6}$ to $BaCoO_3$ in air. Between 920 °C and 960 °C, the peak ratio remained nearly constant, suggesting that the oxidation of $BaCoO_{2.6}$ to $BaCoO_3$ had reached its limit in air.[8]

When the annealing temperature is greater than or equal to 980 °C, diffraction peaks of $BaCoO_{2.2}$ and CoO appear whereas those of $BaCoO_3$ and $BaCoO_{2.6}$ disappear, indicating reduction process. This high-temperature reduction is consistent with previously reported trends in polycrystalline $BaCoO_{3-x}$ ($0 < x < 1$) and with the well-established reduction of Co_3O_4 to CoO above 900 °C.[5, 8]

Based on the observed structure evolution of BCO, we next confirmed its impact on electron transport properties, the in-plane σ and S of BCO thin films were measured at room temperature after annealing each step in air. (**Figure 4-4**). When the annealing temperature is less than or equal to 650°C (blue), σ is a constant of 1500 S cm^{-1} and S is a constant of 95 μV K^{-1}, indicating that the electron transport mechanisms were preserved. These observations are consistent with the stability of the layered structure. At 675 °C, σ dropped to 750 S cm^{-1}, while S remained unchanged (~95 μV K^{-1}). This is consistent with migration and rearrangement of Ba observed in in-plane XRD. A comparable trend has been reported in $Ca_{1/3}CoO_2$, where Ca-ion rearrangement introduces structural

disorder and reduces conductivity, while thermopower remains stable due to a preserved Co valence state under constant composition.[13] After the BCO structure was decomposed at 700 °C, σ drastically decreased to 120 S cm^{-1} and S slightly increased to 115 μV K^{-1}. As the annealing temperature increased, the σ continued to decrease, reaching ~ 30 S cm^{-1} at 920 °C, and the S increased to 143 μV K^{-1}. Between 920 °C and 960 °C, both σ and S saturated due to oxidation limitations identified by XRD. Above 980 °C, σ fell below the

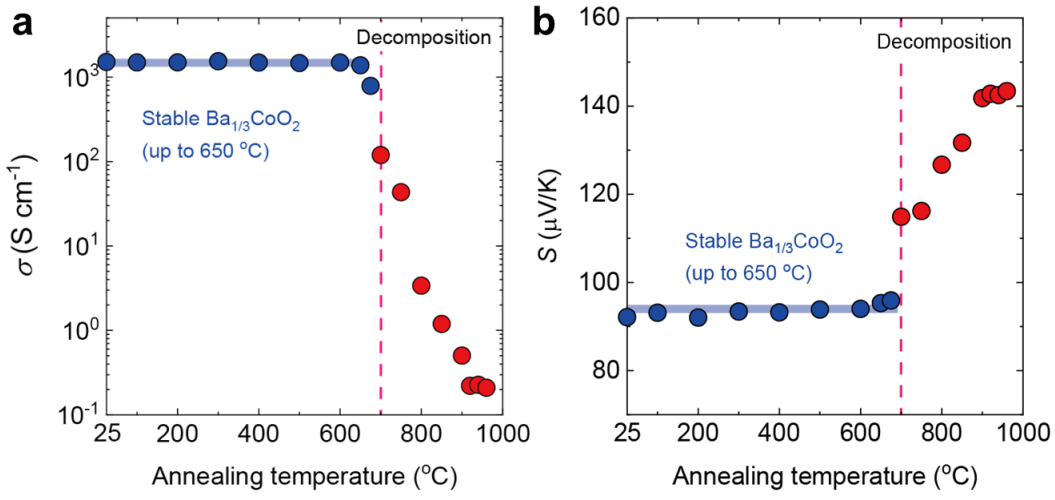

Figure 4-4. Changes in the electron transport properties of a $Ba_{1/3}CoO_2$ epitaxial film upon decomposition into $BaCoO_x$ (x = 3, 2.6, and 2.2) and Co_3O_4 at elevated temperatures. (a) Room temperature electrical conductivity (σ) and (b) thermopower (S) with the annealing temperature. The σ is 1500 S cm^{-1} constant and S is 95 μV K^{-1} constant when the annealing temperature is less than or equal to 650 °C (blue). After annealing at greater than or equal to 700 °C, σ drastically decreases while S linearly increases.

detection limit, precluding reliable transport properties measurements. This degradation is attributed to the reduction of $BaCoO_x$ (x = 3 and 2.6) to $BaCoO_{2.2}$, which increases the fraction of Co^{2+} ions and severely disrupts electron transport properties. These changes in electron transport properties were highly reproducible, with sample-to-sample variations below 5%.

The change in electron transport properties at high temperatures is attributed to the structural decomposition of BCO into several distinct phases, $BaCoO_3$, $BaCoO_{2.6}$, and Co_3O_4, all of which exhibit relatively low conductivity. This change can be interpreted in terms of percolation conduction, which will be examined in the following section by analyzing the transport properties and volume fractions of each constituent phase.

To this end, epitaxial thin films of $BaCoO_3$ and $BaCoO_{2.6}$ were formed, and their electron transport properties were investigated. These measurements clarify which phases play as conductive or insulating components within the percolation. As shown in **Figure 4-5**, $BaCoO_3$ epitaxial films were grown along both the 0001 and $11\bar{2}0$ orientations to experimentally confirm this anisotropy. The in-plane σ was below the detection limit, indicating highly insulating behavior, whereas the cross-plane σ was 3 S cm^{-1} with a thermopower of 60 μV K^{-1}, consistent with semiconducting behavior.[6, 14]

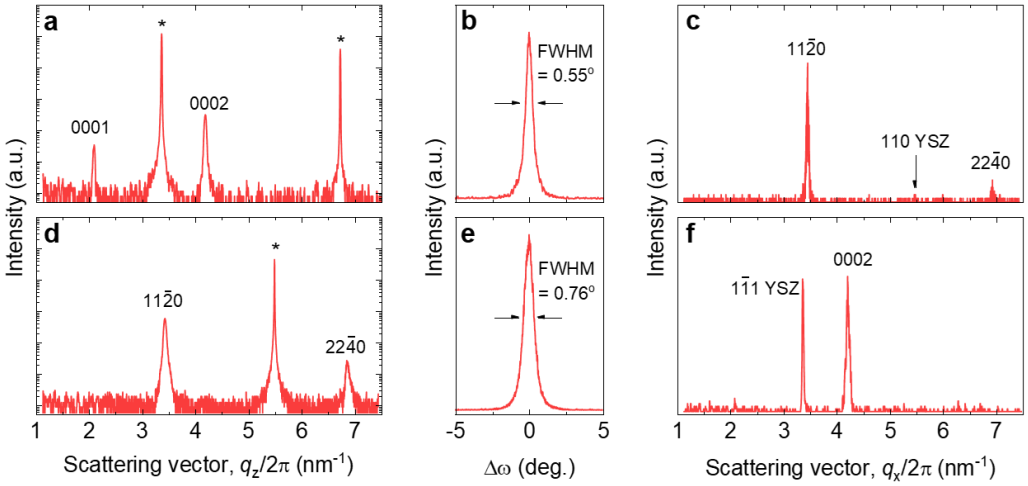

Figure 4-5. Crystallographic orientation of $BaCoO_3$ on YSZ substrates. (a–c) XRD patterns of $BaCoO_3$ on (111) YSZ. (a) Out-of-plane XRD pattern showing 000*l* diffraction peaks of $BaCoO_3$ with 111 YSZ. (b) Out-of-plane X-ray rocking curve of 0002 $BaCoO_3$. (c) In-plane XRD pattern revealing 11$\bar{2}$0 diffraction peak with the 110 YSZ. The epitaxial relationship is (0001)[11$\bar{2}$0] $BaCoO_3$ || (111)[110] YSZ. (d–f) XRD patterns of $BaCoO_3$ on (110) YSZ. (a) Out-of-plane XRD pattern showing 11$\bar{2}$0 and 22$\bar{4}$0 diffraction peaks of $BaCoO_3$ with 110 YSZ. (b) Out-of-plane X-ray rocking curve of 11$\bar{2}$0 $BaCoO_3$. (c) In-plane XRD pattern revealing 0002 diffraction peak with the 111 YSZ. The epitaxial relationship is (11$\bar{2}$0)[0001] $BaCoO_3$ || (110)[111] YSZ.

Then, $BaCoO_3$ thin films were annealed at 700 °C for 30 minutes under a vacuum pressure of 10^{-4} Pa to induce reduction, as shown in **Figure 4-6**, successfully formed the $BaCoO_{2.6}$ phase. The lattice parameters of the epitaxial $BaCoO_3$ and $BaCoO_{2.6}$ films closely match those obtained from BCO decomposition (see **Table 4-1**). The resultant $BaCoO_{2.6}$ films

exhibited an in-plane σ of ~ 100 S cm^{-1} and a thermopower of 80 μV K^{-1} at room temperature. Co_3O_4, by contrast, is well established as an insulating phase.[5] These results indicate that $BaCoO_{2.6}$ functions as a conductor, whereas $BaCoO_3$ and Co_3O_4 act as non-conductive phases.

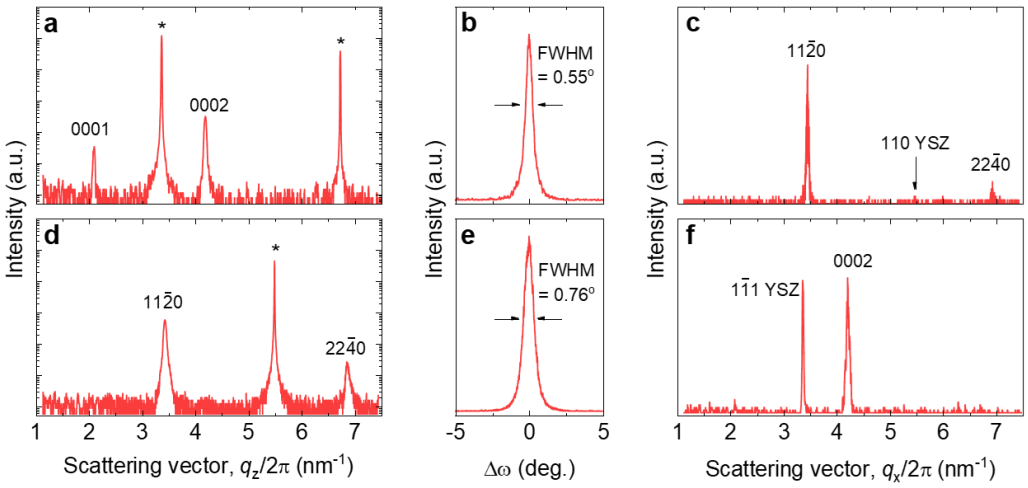

Figure 4-6. Reduction of $BaCoO_3$ into $BaCoO_{2.6}$ by thermal annealing in vacuum (700 °C for 30 min under 10^{-4} Pa). (a) Out-of-plane and (b) in-plane XRD patterns of $BaCoO_3$ epitaxial films before (gray) and after (red) the reduction treatment. $BaCoO_3$ is reduced to $BaCoO_{2.6}$ after annealing in vacuum.

Table 4-1. Change in the lattice parameters of the $BaCoO_3$ epitaxial film after thermal annealing in vacuum (700 °C for 30 min under 10^{-4} Pa).

Phase	***a*** **(Å)**	***c*** **(Å)**
$BaCoO_3$	5.78 (5.84)	4.78 (4.75)
$BaCoO_{2.6}$	5.67 (5.70)	28.52 (28.26)

Additionally, we prepared a binary phase ($BaCoO_{2.6}$ + Co_3O_4) to provide an additional data point for percolation analysis. This phase was obtained by subsequent vacuum annealing of a BCO epitaxial film that had been decomposed at 700 °C in air (**Figure 4-7**). The σ of this phase increased to 200 S cm^{-1}, compared to 114 S cm^{-1} before vacuum annealing, while the S unchanged at 115 μV K^{-1}. These results clearly indicate that $BaCoO_x$ (x = 3 and 2.6) is reduced under low-oxygen-pressure conditions.

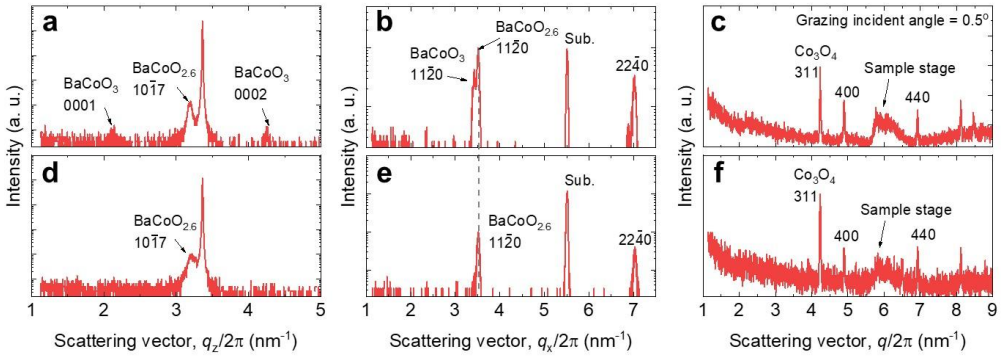

Figure 4-7. Formation of $BaCoO_{2.6}$ phase after vacuum annealing of 700 °C annealed $Ba_{1/3}CoO_2$ epitaxial film. (a–c) XRD patterns of a $Ba_{1/3}CoO_2$ epitaxial film decomposed at 700 °C in air. (a) Out-of-plane XRD pattern, (b) in-plane XRD pattern, and (c) GIXRD pattern indicate that the film is composed of oriented $BaCoO_{2.6}$ and $BaCoO_3$ phases as well as randomly oriented polycrystalline Co_3O_4 phase. (d–f) XRD patterns after subsequent vacuum annealing (10^{-4} Pa, 700 °C, 30 min) of a $Ba_{1/3}CoO_2$ epitaxial film decomposed at 700 °C in air. (d) Out-of-plane XRD pattern, (e) in-plane XRD pattern, and (f) GIXRD pattern indicate that the film is composed of oriented $BaCoO_{2.6}$ phase and randomly oriented polycrystalline Co_3O_4 phase.

Next, the volume fractions of each phase in decomposed BCO were estimated using in-plane XRD (**Figure 4-8a**). ICP-MS analysis confirmed that the Ba/Co ratio remained constant at ~ 0.28 after decomposition. In the volume fraction calculations, we assumed that (1) all Ba atoms form the $BaCoO_x$ (x = 3 and 2.6) phase, and (2) the remaining Co atoms form Co_3O_4. Therefore, the volume fraction of Co_3O_4 was fixed throughout the analysis, and the overall phase ratio was defined as follows:

$$0.28(y\ BaCoO_3 + z\ BaCoO_{2.6}) + 0.24\ Co_3O_4, \text{ where } y + z = 1$$

The mole ratios (y and z) of $BaCoO_x$ (x = 3 and 2.6) were calculated from the integral intensity ratio of in-plane XRD peaks and subsequently converted to volume fractions using the following equation.

$$\text{Volume fraction of phase } i = \frac{n_i \cdot \frac{M_i}{\rho_i}}{\sum n \cdot \frac{M}{\rho}}$$

Here, n is the relative mole ratio, M is the molar mass, and ρ is the theoretical density of each phase. As shown in **Figure 4-8b**, the volume fraction of $BaCoO_{2.6}$ decreases with increasing annealing temperature and eventually saturates between 920 °C and 960 °C in air. In this temperature range, the volume ratio of $BaCoO_{2.6}$ to $BaCoO_3$ stabilizes at 26:74, corresponding to an average composition of $BaCoO_{2.89}$. The observed oxidation behavior is consistent with previously reported studies.[8]

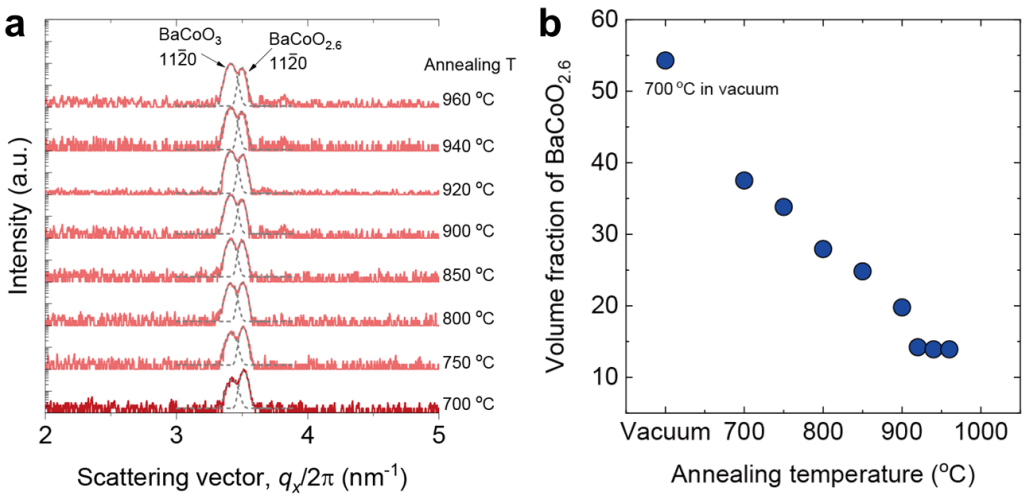

Figure 4-8. Change in the volume fraction of $BaCoO_3$/$BaCoO_{2.6}$ after annealing at elevated temperatures. (a) In-plane XRD patterns of a $Ba_{1/3}CoO_2$ epitaxial film annealed at elevated temperatures (700–960 °C) in ambient air. The two different diffraction peaks are fitted using Gaussian function (dashed lines). The volume fraction of $BaCoO_{2.6}$ was calculated by assuming the integrated diffraction peak intensity ratio directly reflects it.

To analyze the evolution in electron transport mechanism of decomposed BCO, σ and S are plotted as a function of volume fraction (**Figure 4-9**). A distinct transition in electron transport properties was observed near the percolation threshold (ϕ_c) at a volume fraction of 28%, which is typical of percolation behavior.[15-18] Below ϕ_c, the conductive network formed by the semiconducting phase is disconnected, resulting in suppressed σ and elevated S, which saturates around 143 μV K^{-1}. Above ϕ_c, the percolation network becomes connected, leading to an increase in σ, while S decreases and saturates at 113 μV

K^{-1}. Above the ϕ_c, saturation of S indicates that once percolation conduction paths are established, the total overall S of the system is predominantly determined by the conduction phase.[18-19]

To quantitatively interpret the percolation behavior, we applied the Generalized Effective Medium Theory (GEMT),[18-19] which successfully reproduced the experimental trends. The GEMT equation is expressed as:

$$\sum_i v_i \frac{\zeta_i^{\frac{1}{t}} - \zeta^{\frac{1}{t}}}{\zeta_i^{\frac{1}{t}} + A \cdot \zeta^{\frac{1}{t}}} = 0$$

Here, ζ_i represents the intrinsic transport property ($\zeta = \sigma$ and σ/S) of each constituent phase, and v_i is its corresponding volume fraction. The critical exponent t, which reflects the connectivity and dimensionality of the percolating network, was determined to be 1.2, a value consistent with typical disordered systems (1.2–1.6). The A is defined as $A = (1 - \phi_c) / \phi_c$. The fitted percolation threshold $\phi_c \approx 0.28$ (28%) closely aligns with the expected value for composite materials, where long-range conductivity typically emerges at approximately 1/3 volume fraction of the highly conductive phase. The GEMT model reproduced the sharp transition near ϕ_c and overall experimental trends, confirming the model's validity in describing percolation conduction in the decomposed BCO.

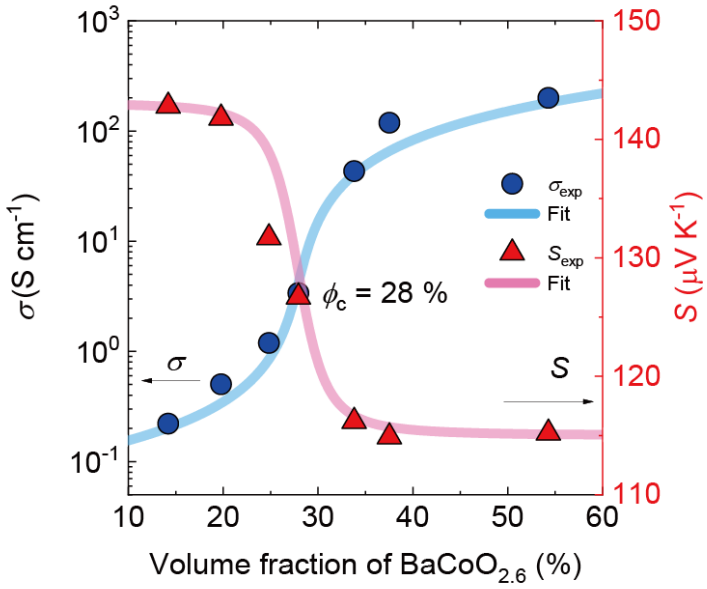

Figure 4-9. Percolation-like electron transport properties. Room temperature σ and S as a function of the volume fraction of $BaCoO_{2.6}$ phase in the annealed film. A sharp transition in transport behavior is observed near the percolation threshold (~28%). Measured values are shown as circles (σ) and triangles (S), while solid curves represent calculated results based on the Generalized Effective Medium Theory (GEMT).

For comparison, a conventional parallel circuit model was also applied (**Figure 4-10**).[20-22] However, this model substantially overestimated σ near the percolation threshold and failed to reproduce the sharp decrease in S. This comparison confirms that the transport in decomposed BCO is governed by a percolation mechanism, which is accurately captured by the GEMT model.

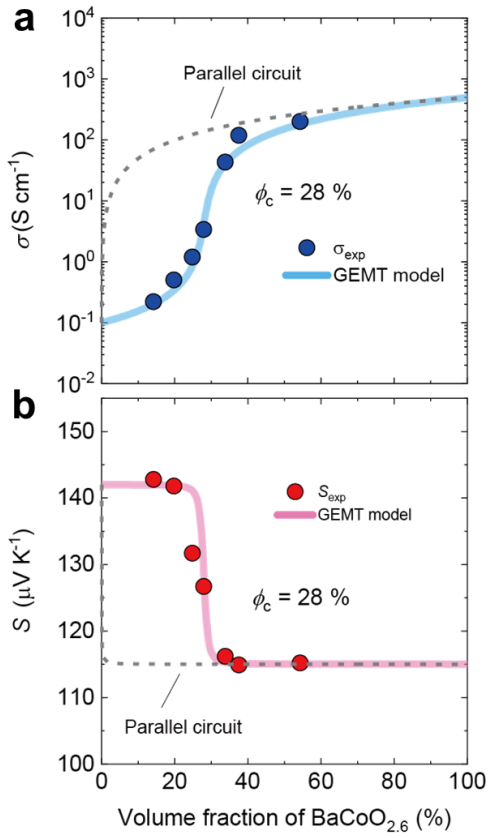

Figure 4-10. Comparison of GEMT and parallel circuit models. (a) Room temperature (a) σ and (b) S as a function of the volume fraction of $BaCoO_{2.6}$ phase in the annealed film. Solid lines represent the GEMT model, while dashed lines indicate the conventional parallel circuit model. The parallel circuit model significantly overestimates σ near the percolation threshold (~ 28%) and fails to capture the sharp decrease in S, whereas the GEMT model successfully reproduces the experimental percolation behavior.

Figure 4-11 shows the low-temperature resistivity of BCO. The as-grown film and the BCO annealed at 650 °C both exhibit Fermi-liquid-like metallic conduction, indicating that the structure and transport properties are preserved up to this temperature. In contrast, after decomposition at 700 °C, the conduction changes from metallic to semiconducting behavior governed by percolation.

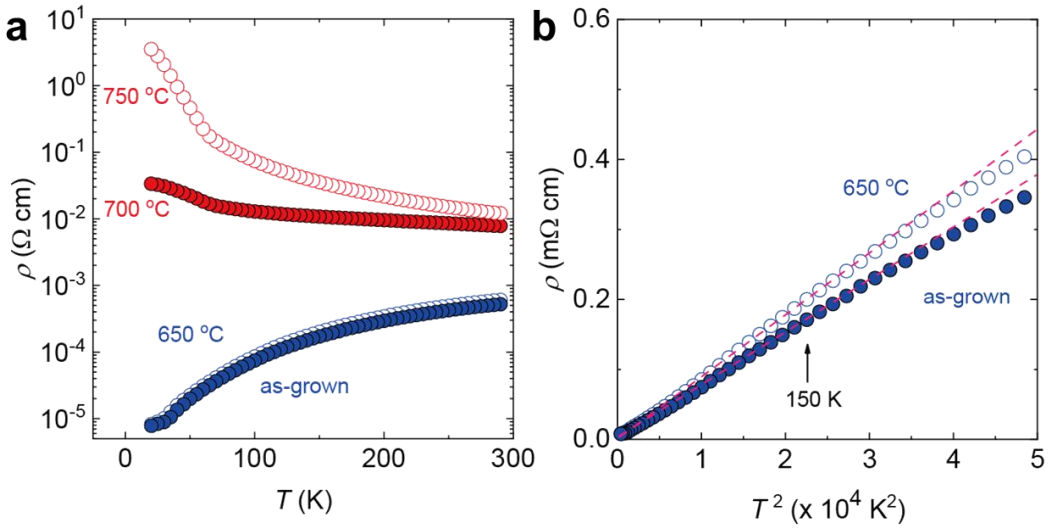

Figure 4-11. Temperature dependence of electrical resistivity for the film after thermal annealing. (a) $\rho - T$ curves. As-grown and 650 °C annealed films show metallic behavior whereas the 700 °C and 750 °C annealed films show insulating behavior. (b) ρ vs. T^2 plot of the metallic films. Fermi-liquid-like conduction is seen.

Then, we directly observed the percolation-like morphology of decomposed BCO at 700 °C using Cs-corrected scanning transmission electron microscopy (STEM). As shown in HAADF images in **Figure 4-12a and 4-12b**, hexagonal grains with overlapping

characteristics are observed, showing distinct three-dimensional percolation-like contrast variations illustrated in **Figure 4-1**. While the sample contains regions with different compositions forming the three-dimensional percolation network, high-angle annular dark-field scanning transmission electron microscopy (STEM-HAADF) contrast cannot be taken as a criterion to distinguish different phases, especially for $BaCoO_x$ (x = 3 and 2.6) that only contain different O contents. Therefore, electron energy-loss spectroscopy (EELS) analysis was combined with STEM-HAADF contrast to distinguish the dominant compositions of these regions and validate the multiphase percolation network. In particular, an increase in the L_3/L_2 ratio corresponds to a decrease in the average Co valence state.[23-24] Meanwhile, the Ba M edge represents the relative Ba content.[25] EELS analysis was employed to three areas with different HAADF contrasts, marked as gray, dark, and black in Figure 5b. The EELS results are shown in **Figure 4-12e** and **4-12f** and **Table 4-2**. The black region exhibits the lowest M_5/L_3 ratio, indicating the lowest relative Ba content. The Co L_3 and L_2 peaks shift to lower energy, and the L_3/L_2 ratio reaches 2.1, indicating the lowest Co valence state. These results mean that Co_3O_4 is the dominant phase in the black region, which could contribute to the Z-related HAADF contrast (Z is the atom number). The gray and dark regions show nearly identical M_5/L_3 ratios, indicating similar Ba contents. On the other hand, the L_3/L_2 ratio is 1.5 in the gray region and 1.9 in the dark region, indicating that the Co valence state is higher in the gray region. Thus, the gray region is dominated by $BaCoO_3$ (Co^{4+}), whereas the dark region is dominated by $BaCoO_{2.6}$ ($Co^{3.2+}$). In the O-K edge spectrum, peaks **a**, **b**, and **c** originate

from the Co−O hybridization. The pre-edge peak (feature **a** ≈ 530 eV) corresponds to the transition from electron to hole states in the Co 3d−O 2p octahedral coordination.[26-28] The O K-edge spectral shape of the black region is in good agreement with the typical spectrum of Co_3O_4.[23, 29] Whereas in the $BaCoO_3$ and $BaCoO_{2.6}$ dominated gray and dark regions, peaks **b** and **c** remain almost unchanged, while the intensity of peak **a** in the dark region decreases, indicating a relatively oxygen-reduced state, which means that $BaCoO_{2.6}$ is dominant in the dark region.

Atomic-resolution HAADF-STEM imaging also provide clear evidence of the coexistence of different $BaCoO_x$ (x = 3 and 2.6) phases. As shown in **Figures 4-12c** and **4-12d,** two grains with hexagonal lattices are observed, with a grain boundary between them (indicated by arrows). The $(11\bar{2}0)$ spacing of the two grains are 2.69 and 2.82 Å, in good accordance to that of $BaCoO_{2.6}$ and $BaCoO_3$. This interpretation provides direct microscopic evidence that the decomposed BCO forms a multiphase percolation network.

Table 4-2. Summary of characteristic EELS spectrum ratios for different contrast regions a $Ba_{1/3}CoO_2$ epitaxial film upon decomposition into $BaCoO_x$ (x = 3 and 2.6) and Co_3O_4 at 700 °C.

Contrast	Co L_3/L_2	Ba M_5/Co L_3	Dominant phase
Gray	1.5	0.54	$BaCoO_3$
Dark	1.9	0.58	$BaCoO_{2.6}$
Black	2.1	0.38	Co_3O_4

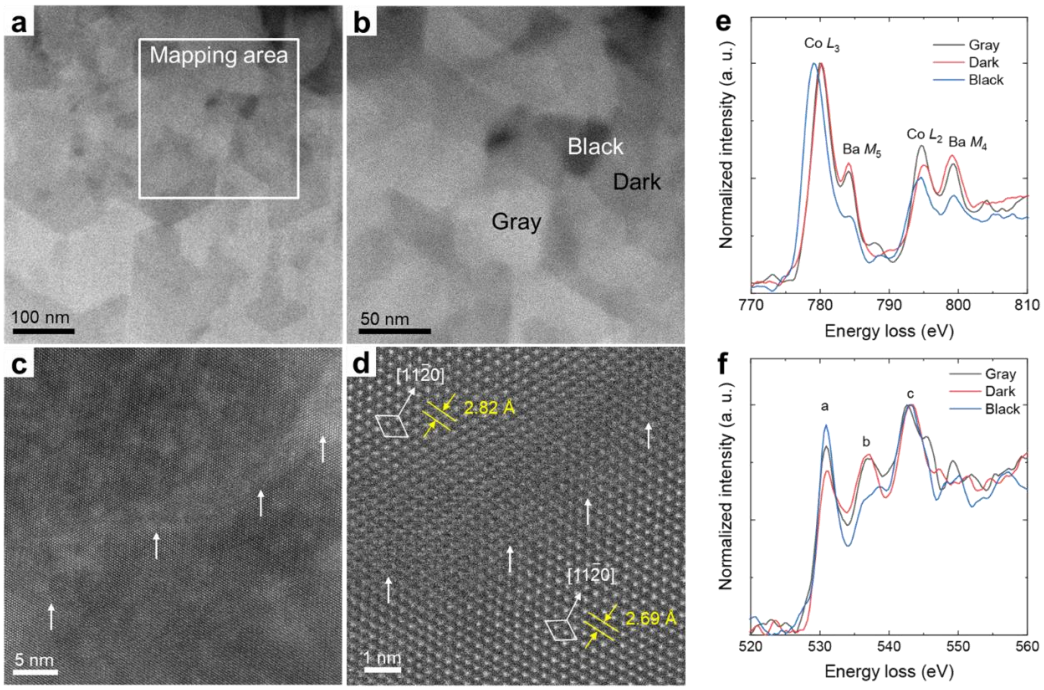

Figure 4-12. Microstructure observations of a $Ba_{1/3}CoO_2$ epitaxial film upon decomposition into $BaCoO_x$ (x = 3 and 2.6) and Co_3O_4 at 700 °C. (a) HAADF-STEM image showing the EELS mapping area. (b) Magnified HAADF-STEM image corresponding to the EELS mapping area in (a), with contrast variations labeled as gray, dark gray, and black regions. (c, d) Atomic-resolution HAADF-STEM images indicating hexagonal lattice pattern and grain boundaries (arrows), with the unit cell of $BaCoO_x$ (x = 3 and 2.6) highlighted in (d). (e) Co L-edge EELS spectra obtained from the gray, dark gray, and black regions. (f) O K-edge EELS spectra obtained from the same regions.

The impact of structural decomposition on thermal conductivity was also evaluated. To obtain the in-plane thermal conductivity ($\kappa_{\parallel}$), BCO films were grown on the $(1\bar{1}00)$ α-Al_2O_3 substrate, and they decomposed into $BaCoO_x$ (x = 3 and 2.6) and polycrystalline Co_3O_4 after annealing at 700 °C (see **Figure 4-13**). The as-grown film shows a well-defined epitaxial relationship of $[11\bar{2}0]$ BCO || [0001] α-Al_2O_3, and several diffraction peaks corresponding to Ba sublattices (1/3 and 1/2) are clearly observed. Diffraction peaks of 0006 and 0001$\underline{2}$ Al_2O_3 due to Cu Lα and Cu Kβ radiations are also seen near the 0006s and 0001$\underline{2}$s diffraction peaks due to Cu Kα radiation. After annealing at 700 °C,

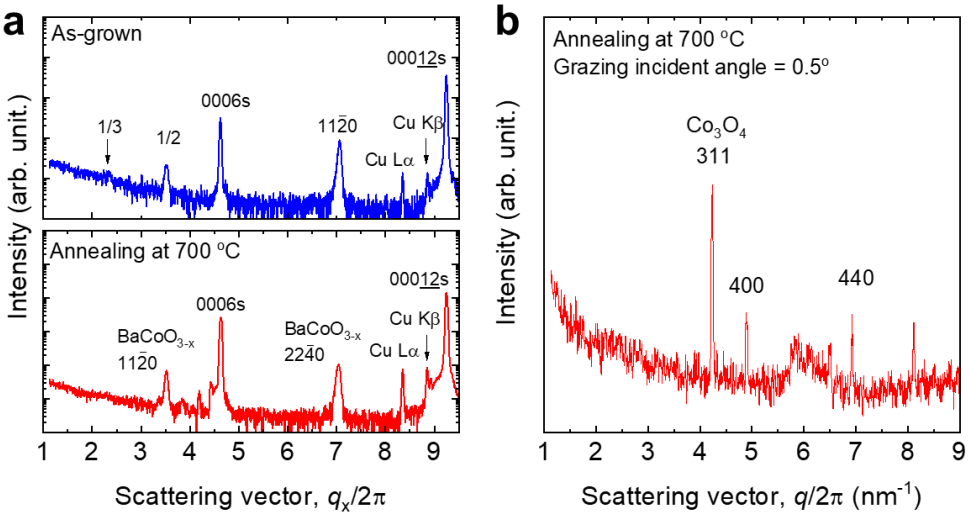

Figure 4-13. Structural analysis of $Ba_{1/3}CoO_2$ films grown on the $(11\bar{2}0)$ α-Al_2O_3 substrate before and after phase decomposition at 700 °C. (a) In-plane XRD patterns of the as-grown (blue) and annealed (red) films. (b) After annealing at 700 °C, GIXRD pattern measured at an incident angle of 0.5°, showing powder-like diffraction features from randomly oriented polycrystalline Co_3O_4.

the sublattice peaks disappear, and diffraction peaks corresponding to $BaCoO_x$ (x = 3 and 2.6) appear, indicating phase decomposition accompanied by the formation of polycrystalline Co_3O_4.

The room-temperature $\kappa_{\parallel}$ of the as-grown BCO film was 3.3 W m^{-1} K^{-1}, while it decreased to 2.3 W m^{-1} K^{-1} after annealing at 700 °C. This reduction would be attributed to enhanced phonon scattering at the grain boundaries formed during phase decomposition. The comparison of TDTR decay curves is shown in **Figure 4-14**. Despite the decrease in $\kappa_{\parallel}$, the room-temperature ZT significantly dropped from 0.12 (as-grown) to 0.017 (after annealed at 700 °C), primarily due to the drastic reduction in electrical conductivity. A similar low ZT was reported in bulk ceramic BCO (0.014 at 300 K), supporting that phase decomposition critically limits thermoelectric performance in bulk materials.[1] In addition, this result clearly indicates that the degradation in thermoelectric performance is dominated by the loss of σ.

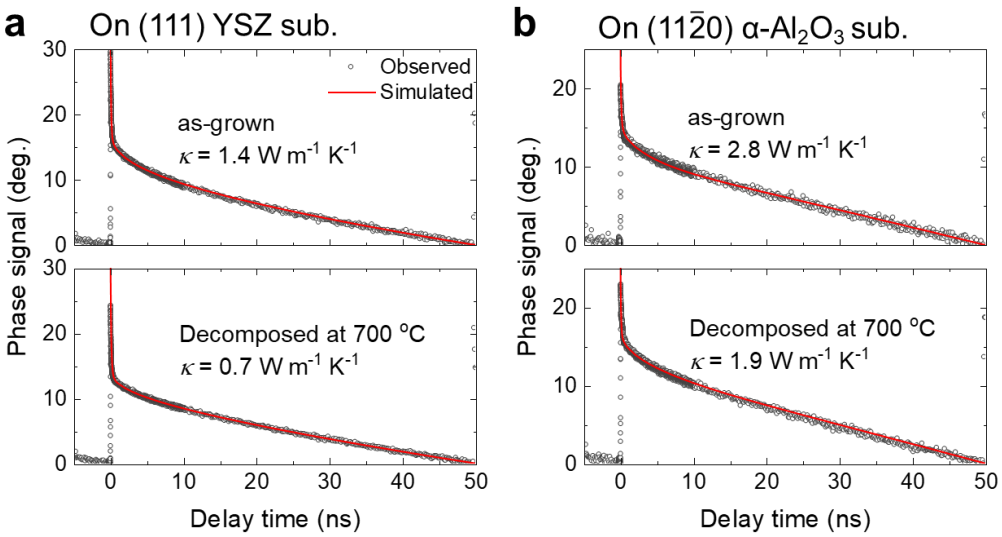

Figure 4-14. Comparison of room temperature TDTR decay curves before and after phase decomposition at 700 °C. (a) Thermal conductivity of *c*-axis-oriented (φ = 0°) films grown on the (111) YSZ substrate. (b) Thermal conductivity of 55° inclined (φ = 55°) films grown on the (11$\bar{2}$0) α-Al_2O_3 substrate.

This study elucidated the mechanism of thermoelectric performance degradation of BCO at high temperatures. Since decomposition of BCO above 700 °C significantly degrades its thermoelectric performance, low temperature fabrication below 700 °C is the key to realize practical thermoelectric devices using BCO. Therefore, low temperature processing methods such as hot pressing, spark plasma sintering, and microwave sintering might be useful to fabricate high-performance thermoelectric BCO bulk in future.

4.4. Conclusion

In this study, we systematically examined the structure evolution of BCO epitaxial films and identified a clear degradation mechanism under high-temperature in air. Above 700 °C, the films decomposed into $BaCoO_x$ (x = 3 and 2.6), and Co_3O_4, with a transition in transport mechanism from metallic to percolation conduction. This behavior was quantitatively reproduced by the GEMT model, while further reduction above 980 °C produced $BaCoO_{2.2}$ and CoO, resulting in complete loss of electron transport. After phase decomposition at 700 °C, the in-plane thermal conductivity decreased from 3.3 to 2.3 W m^{-1} K^{-1}, whereas the room-temperature ZT dropped sharply from 0.12 to 0.017. Such a drastic decline in ZT suggests that the thermoelectric functionality is almost completely degraded after phase decomposition. These results demonstrate that conventional high-temperature sintering cannot preserve the properties of BCO, making bulk fabrication and scale-up challenging. To overcome this limitation, the development of low-temperature sintering or alternative processing methods is required. In addition, this suggests that polymers or freestanding BCO, which do not require high-temperature sintering, could be utilized as flexible or wearable thermoelectric devices.

Reference

[1] Liu, J. *et al.*, High-temperature thermoelectric properties of layered Ba_xCoO_2. *Scr. Mater.* **100**, 63-65 (2015).

[2] Liu, J. *et al.*, Synthesis and physical properties of layered Ba_xCoO_2. *Dalton Trans.* **43**, 15414-15418 (2014).

[3] Zhang, X. *et al.*, $Ba_{1/3}CoO_2$: A Thermoelectric Oxide Showing a Reliable *ZT* of approximately 0.55 at 600 ºC in Air. *ACS Appl. Mater. Interfaces* **14**, 33355-60 (2022).

[4] Jacobson, A. *et al.*, An investigation of the structure of 12H-$BaCoO_{2.6}$ by electron microscopy and powder neutron diffraction. *J. Solid State Chem.* **35**, 334-340 (1980).

[5] Greenwood, N. N. *et al.*, *Chemistry of the Elements*. Elsevier: 2012.

[6] Wang, H. *et al.*, Crystal growth and characterization of the quasi-one-dimensional compound $BaCoO_3$. *J. Cryst. Growth* **430**, 52-54 (2015).

[7] Chin, Y. *et al.*, Spin-orbit coupling and crystal-field distortions for a low-spin $3d^5$ state in $BaCoO_3$. *Phys. Rev. B* **100**, 205139 (2019).

[8] Diatta, A. *et al.*, $BaCoO_2$ with Tetrahedral Cobalt Coordination: The Missing Element to Understand Energy Storage and Conversion Applications in $BaCoO_{3-\delta}$-Based Materials. *J. Am. Chem. Soc.* **146**, 15027-15035 (2024).

[9] Mentré, O. *et al.*, $BaCoO_{2.22}$: the most oxygen-deficient certified cubic perovskite. *Dalton Trans.* **44**, 10728-10737 (2015).

[10] Takashima, Y. *et al.*, Layered cobalt oxide epitaxial films exhibiting thermoelectric *ZT* = 0.11 at room temperature. *J. Mater. Chem. A* **9**, 274-280 (2021).

[11] Cho, H. J. *et al.*, Anisotropic Heat Conduction in Ion-Substituted Layered Cobalt Oxides. *Adv. Mater. Interfaces* **7**, 1901816 (2020).

[12] Yang, H. *et al.*, Strontium ordering, structural modulation in layered hexagonal Sr_xCoO_2 and physical properties of $Sr_{0.35}CoO_2$. *Mater. Res. Bull.* **42**, 94-101 (2007).

[13] Sugiura, K. *et al.*, Structural transformation of Ca-arrangements and carrier transport properties in $Ca_{0.33}CoO_2$ epitaxial films. *Appl. Phys. Express* **2**, 035503 (2009).

[14] Wang, H. *et al.*, Impersonating a Superconductor: High-Pressure $BaCoO_3$, an Insulating Ferromagnet. *J. Am. Chem. Soc.* **145**, 21203-21206 (2023).

[15] McLachlan, D. S. *et al.*, Electrical resistivity of composites. *J. Am. Ceram. Soc.* **73**, 2187-2203 (1990).

[16] Vaney, J.-B. *et al.*, Effective medium theory based modeling of the thermoelectric properties of composites: comparison between predictions and experiments in the glass–crystal composite system $Si_{10}As_{15}Te_{75}$–$Bi_{0.4}Sb_{1.6}Te_3$. *J. Mater. Chem. C* **3**, 11090-11098 (2015).

[17] Stauffer, D. *et al.*, *Introduction to percolation theory*. Taylor & Francis: 2018.

[18] Rösch, A. G. *et al.*, Improved Electrical, Thermal, and Thermoelectric Properties Through Sample-to-Sample Fluctuations in Near-Percolation Threshold Composite Materials. *Adv. Theory Simul.* **4**, 2000284 (2021).

[19] Sonntag, J., Comment on “Effective medium theory based modeling of the thermoelectric properties of composites: comparison between predictions and experiments in the glass–crystal composite system $Si_{10}As_{15}Te_{75}$–$Bi_{0.4}Sb_{1.6}$ Te_3” by J.-B.

Vaney *et al*., *J. Mater. Chem. C*, 2015, 3, 11090. *J. Mater. Chem. C* **4**, 10973-10976 (2016).

[20] Bergman, D. J. *et al.*, Thermoelectric properties of a composite medium. *J. Appl. Phys.* **70**, 6821-6833 (1991).

[21] Gelbstein, Y., Thermoelectric power and structural properties in two-phase Sn/SnTe alloys. *J. Appl. Phys.* **105**, (2009).

[22] Yang, Q. *et al.*, Macroscopic visualization of fast electrochemical reaction of $SrCoO_x$ oxygen sponge. *Adv. Mater. Interfaces* **6**, 1901260 (2019).

[23] Zhao, Y. *et al.*, In situ electron energy loss spectroscopy study of metallic Co and Co oxides. *J. Appl. Phys.* **108**, (2010).

[24] Wang, Z. *et al.*, EELS analysis of cation valence states and oxygen vacancies in magnetic oxides. *Micron* **31**, 571-580 (2000).

[25] Shen, T.-H. *et al.*, Oxygen Evolution Reaction in $Ba_{0.5}Sr_{0.5}Co_{0.8}Fe_{0.2}O_{3-\delta}$ Aided by Intrinsic Co/Fe Spinel-Like Surface. *J. Am. Chem. Soc.* **142**, 15876-15883 (2020).

[26] De Groot, F. *et al.*, Oxygen 1s x-ray-absorption edges of transition-metal oxides. *Phys. Rev. B* **40**, 5715 (1989).

[27] Jeen, H. *et al.*, Reversible redox reactions in an epitaxially stabilized $SrCoO_x$ oxygen sponge. *Nat. Mater.* **12**, 1057-1063 (2013).

[28] Wu, Z. *et al.*, Characterization of iron oxides by x-ray absorption at the oxygen K edgeusing a full multiple-scattering approach. *Phys. Rev. B* **55**, 2570 (1997).

[29] Zhang, Y. *et al.*, Lithiation-Induced Vacancy Engineering of Co_3O_4 with Improved Faradic Reactivity for High-Performance Supercapacitor. *Adv. Funct. Mater.* **30**, 2004172 (2020).

Chapter 5. Summary

In this doctoral dissertation, the intrinsic thermoelectric transport properties and practical limitations of the layered cobalt oxide $Ba_{1/3}CoO_2$ (BCO) were systematically investigated, with the goal of clarifying the origin of its high thermoelectric performance and identifying key factors that hinder its application in bulk form. By integrating studies on substrate-free single-crystalline films and high-temperature structural evolution, this work establishes a coherent understanding of the relationship between crystal structure, electron transport mechanisms, and thermoelectric performance in BCO.

Freestanding single-crystalline BCO sheets were successfully fabricated by exfoliating epitaxial thin films from sacrificial substrates, enabling direct evaluation of intrinsic thermoelectric properties without substrate-induced suppression. The freestanding BCO sheets retained high electrical conductivity and large thermopower, demonstrating that the excellent thermoelectric performance reported for epitaxial BCO films originates from the intrinsic electronic structure of BCO itself. Reliable determination of in-plane thermal conductivity further allowed quantitative assessment of the intrinsic thermoelectric figure of merit.

To address the long-standing discrepancy between thin-film and bulk thermoelectric performance, the high-temperature structural stability of BCO was systematically

examined. Controlled annealing experiments revealed that BCO undergoes phase decomposition above approximately 700 °C, leading to the formation of $BaCoO_3$, $BaCoO_{2.6}$, and Co_3O_4. This structural evolution induces a transition in the dominant electron transport mechanism from metallic conduction to percolation conduction, resulting in a pronounced degradation of electrical conductivity and thermoelectric performance. These findings provide a direct physical explanation for the poor thermoelectric properties observed in bulk BCO ceramics fabricated via high-temperature sintering.

Through these investigations, this dissertation clarifies that the practical limitations of BCO thermoelectrics do not stem from a lack of intrinsic transport capability, but rather from structural instability during thermal processing required for bulk fabrication. The insights obtained in this study highlight the critical importance of controlling phase stability and microstructural evolution in layered cobalt oxides, and they offer fundamental guidelines for bridging the gap between high-performance thin films and scalable thermoelectric materials. More broadly, this work contributes to the understanding of oxide thermoelectrics and provides a conceptual framework for designing thermally robust, high-performance thermoelectric materials suitable for practical applications.

Acknowledgement

As I write this acknowledgement, I am filled with deep emotion. The long and eventful journey of my doctoral studies has finally come to an end, and a new chapter in my career awaits. Although there are moments I wish I could revisit, I devoted myself fully to my studies and research without regret.

My connection with Prof. Hiromichi Ohta began in 2018, when I was an undergraduate research student in the Prof. Jeen group at Pusan National University and he visited us as a seminar speaker. Later, during my master's program, I had the opportunity to continue this connection through collaborative research with Dr. Chen from his group. After completing my master's degree, I expressed my strong desire to join Prof. Ohta's group, and I am sincerely grateful that he kindly accepted me. This marked the beginning of my research life at Hokkaido University.

Prof. Ohta provided an outstanding research environment and offered continuous guidance, encouragement, and insightful advice throughout my doctoral studies. Thanks to his support, I was able to complete my Ph.D. successfully and gain invaluable experiences through international conferences and meaningful collaborative research. I would like to express my deepest gratitude to him.

I am also profoundly grateful to Prof. Jeen at Pusan National University, who continued to offer warm encouragement and thoughtful advice even after my master's graduation.

I would like to thank Prof. Terasaki and Assistant Prof. Nakano at Nagoya University for their generous support and valuable discussions during our collaborative research.

My sincere appreciation also goes to Prof. Matsuo and Asstant Prof. Endo for their assistance with TEM measurements. I am especially grateful to Prof. Ikuhara, Prof. Feng, Dr. Yang, and Dr. Yan at the University of Tokyo for their invaluable support with the challenging plan-view TEM experiments.

I would like to thank all the members of our laboratory who supported and encouraged me. I am particularly grateful to Associate Prof. Katayama for his kindness and for creating a comfortable research atmosphere, and to Assistant Prof. Magari for his thoughtful advice and guidance. I also deeply appreciate Asstant Prof. Jeong for her support and encouragement as a fellow Korean researcher.

I am thankful to Dr. Bian, my first Chinese friend in the group, who helped me adapt to the laboratory and shared many conversations and concerns with me. His diligence, sharp insight in research, and long-term vision for life have greatly inspired me. I am also deeply grateful to Yoshimura, my first Japanese friend, who accompanied me throughout my

doctoral journey and provided constant support. Her sincerity and dedication have been a great example to me. I would also like to thank Dr. Chen, Dr. Gong, Dr. Yang, Dr. Wu , Mr. Sadahira and Mr. Zhou for helping me adapt to both laboratory life and daily life in Japan. Dr. Prashant's passion for research consistently motivated me, and I am thankful to Mr. Kong for his positivity and support.

I would like to express my deepest gratitude to my parents in Korea for their unwavering support throughout my years abroad. Without their trust and encouragement, I would not have been able to complete this journey with peace of mind. I am also grateful for the financial support provided by the EXEX Doctoral Fellowship during my studies in Japan.

The doctoral journey was filled with challenges, excitement, and moments of uncertainty. These experiences have shaped me into a stronger person and broadened my perspective on both research and life.

Finally, I would like to extend my sincere appreciation to everyone who supported me throughout this doctoral journey.

Kungwan Kang

Sapporo, Japan

2026.03

List of Publications

Publications related to this thesis

[1] **K. Kang***, F. Kato, A. Nakano, I. Terasaki*, T. Endo, Y. Matsuo, H. Jeen*, and H. Ohta*, "Fabrication and Thermoelectric Properties of Freestanding $Ba_{1/3}CoO_2$ Single Crystalline Films", *ACS Appl. Electron. Mater.* **5**, 5749-5754 (2023).

[2] **K. Kang***, Y. Zhang, J. Yan, C. Yang, B. Feng, N. Shibata, Y. Ikuhara, A. Jeong, and H. Ohta*, "Decomposition Behavior of a Thermoelectric Oxide at High-Temperatures and Its Impact on the Thermoelectric Properties", *ACS Appl. Energy Mater.* **9**, 1883-1890 (2026).

Other publications

[1] Binjie Chen*, **Kungwan Kang**, Hyoungjeen Jeen, Yuqiao Zhang, Jinghuang Lin, Bin Feng, Yuichi Ikuhara, Sena Hoshino, Katsuyuki Matsunaga, and Hiromichi Ohta*, "Orthorhombic Distortion-induced Anatase-like Optoelectronic Properties of Rutile TiO2", *J. Appl. Phys.* **132**, 185301 (2022).

List of Presentations

[1] Kungwan Kang, Yuqiao Zhang, Jingyuan Yan, Chuchu Yang, Bin Feng, Naoya Shibata, Yuichi Ikuhara, Ahrong Jeong, and Hiromichi Ohta, “Origin of degradation in thermoelectric performance of $Ba_{1/3}CoO_2$ at high temperatures”, Japan–Taiwan–India Symposium on Materials & Information Science for Future Electronics Jointed with the 26th RIES‐HOKUDAI International Symposium “共”[kyou] & 5+2 Joint Symposium, Sapporo, November 26-27, 2025 (Poster)

[2] Kungwan Kang, Yuqiao Zhang, Chuchu Yang, Bin Feng, Yuichi Ikuhara, Ahrong Jeong, Takashi Endo, Yasutaka Matsuo, and Hiromichi Ohta, “Phase decomposition of thermoelectric $Ba_{1/3}CoO_2$ films at high temperatures”, 第 61 回 応用物理学会北海道支部学術講演会, 北海道大学, 札幌, 2025.11.1-2.

[3] Kungwan Kang, Yuqiao Zhang, Jingyuan Yan, Chuchu Yang, Bin Feng, Naoya Shibata, Yuichi Ikuhara, Ahrong Jeong, and Hiromichi Ohta, “Origin of degradation in thermoelectric performance of $Ba_{1/3}CoO_2$ at high temperatures”, 第 11 回 北大・部局横断シンポジウム, 北海道大学, 札幌, 2025 年 10 月 2 日 (Poster).

[4] Kungwan Kang, Yuqiao Zhang, Chuchu Yang, Bin Feng, Yuichi Ikuhara, Ahrong Jeong, Takashi Endo, Yasutaka Matsuo, and Hiromichi Ohta, “Phase decomposition of thermoelectric $Ba_{1/3}CoO_2$ films at high temperatures”, 第 86 回 応用物理学会秋季学術講演会, 名城大学天白キャンパス+オンライン, 2025.9.7-10.

[5] Kungwan Kang, Diwen Chen, Masato Imaizumi, Akitoshi Nakano, Chuchu Yang,

Yuqiao Zhang, Yusaku Magari, Takashi Endo, Bin Feng, Yasutaka Matsuo, Yuichi Ikuhara, Ichiro Terasaki, Hiromichi Ohta, "Difficulty of Bulk Ceramic Fabrication of $Ba_{1/3}CoO_2$ Showing High Thermoelectric *ZT* ", 2024 年 第 71 回 応用物理学会春季学術講演会, 東京都市大学 世田谷キャンパス,東京, 2024 年 3 月 22 日-25 日.

[6] Kungwan Kang, Fumiaki Kato, Akitoshi Nakano, Ichiro Terasaki, Hyoungjeen Jeen, and Hiromichi Ohta, "Fabrication and Thermoelectric Properties of Freestanding $Ba_{1/3}CoO_2$ Single Crystalline Films", 第 59 回 応用物理学会北海道支部 / 第 20 回 日本光学会北海道支部 合同学術講演会, 北海道大学, 札幌市, 2024.1.6 – 7.

[7] Kungwan Kang, Fumiaki Kato, Akitoshi Nakano, Ichiro Terasaki, Hyoungjeen Jeen, Hiromichi Ohta, "[B1-O301-01] Direct Measurement of In-Plane Thermal Conductivity for Freestanding $Ba_{1/3}CoO_2$ and $Sr_{1/3}CoO_2$ Films", MRM2023, Kyoto, Japan, December 11-16, 2023. (oral)

[8] Kungwan Kang, Fumiaki Kato, Akitoshi Nakano, Ichiro Terasaki, Takashi Endo, Yasutaka Matsuo, Hyoungjeen Jeen, Hiromichi Ohta, "Fabrication and Thermoelectric Properties of Freestanding $Ba_{1/3}CoO_2$ Single Crystalline Films", The 2023 RIES-CEFMS (Research Institute for Electronic Science – Center for Emergent Functional Matter Science) Joint International Symposium, Rusutsu Resort Hotel and Convention Center, Japan, December 7-8, 2023. (Poster)

[9] Kungwan Kang, Fumiaki Kato, Akitoshi Nakano, Ichiro Terasaki, Takashi Endo, Yasutaka Matsuo, Hyoungjeen Jeen, and Hiromichi Ohta, "Preparation and

Thermoelectric Properties of Freestanding $Ba_{1/3}CoO_2$ Single Crystalline Films", The 24th RIES-HOKUDAI International Symposium 開 [kai], Hokkaido University, Sapporo, Japan, December 6-7, 2023.

[10] Kungwan Kang, Fumiaki Kato, Akitoshi Nakano, Ichiro Terasaki, Takashi Endo, Yasutaka Matsuo, Hyougjeen Jeen, and Hiromichi Ohta, "Preparation and thermoelectric properties of freestanding $Ba_{1/3}CoO_2$ single crystalline films", The Mini-Workshop on Functional Materials Science (Organizers' meeting), Sapporo, Japan, December 1-2, 2023. (Poster)

[11] Kungwan Kang, Fumiaki Kato, Akitoshi Nakano, Ichiro Terasaki, Takashi Endo, Yasutaka Matsuo, Hyoungjeen Jeen, and Hiromichi Ohta, "Fabrication and thermoelectric properties of freestanding $Ba_{1/3}CoO_2$ single crystalline films", 第 49 回固体イオニクス討論会, 北海道大学フロンティア応用科学研究棟, 2023 年 11 月 15 日

[12] Kungwan Kang, Fumiaki Kato, Akitoshi Nakano, Ichiro Terasaki, Takashi Endo, Yasutaka Matsuo, Hyoungjeen Jeen, and Hiromichi Ohta, "Fabrication and Thermoelectric Properties of Freestanding $Ba_{1/3}CoO_2$ Single Crystalline Films", 14th ISAJ Annual Symposium (Integrated Science for a Sustainable Society), Hokkaido University, Sapporo, November 14, 2023

[13] Kungwan Kang, Fumiaki Kato, Akitoshi Nakano, Ichiro Terasaki, Hyoungjeen Jeen, and Hiromichi Ohta, "Direct Thermal Conductivity Measurement for Freestanding $Ba_{1/3}CoO_2$ and $Sr_{1/3}CoO_2$ Films in the In-plane direction", 29th International

Workshop on Oxide Electronics (iWOE29), Busan, Korea, October 15-18, 2023. (poster)

[14] Kungwan Kang, Fumiaki Kato, Akitoshi Nakano, Ichiro Terasaki, Hyoungjeen Jeen, Hiromichi Ohta, “Direct Measurement of In-Plane Thermal Conductivity for Freestanding Oxide Films”, 第 84 回応用物理学会秋季学術講演会「イオントロニクスにおける酸化物・カルコゲナイトの新機能」, 熊本城ホールほか 3 会場, 2023 年 9 月 19 日-23 日(ポスター)

[15] Kungwan Kang, Fumiaki Kato, Ichiro Terasaki, Hyoungjeen Jeen, and Hiromichi Ohta, “Direct measurement of in-plane thermal conductivity for freestanding $Ba_{1/3}CoO_2$ films”, The 4th Workshop on Functional Materials Science (FMS2023), Busan, South Korea, June 18-21, 2023. (poster)

List of Awards

[1] Best Presentation Award → Kungwan Kang, Fumiaki Kato, Akitoshi Nakano, Ichiro Terasaki, Hyoungjeen Jeen, and Hiromichi Ohta, "Direct Thermal Conductivity Measurement for Freestanding $Ba_{1/3}CoO2$ and $Sr_{1/3}CoO_2$ Films in the In-plane direction", 29th International Workshop on Oxide Electronics (iWOE29), Busan, Korea, October 15-18, 2023.

[2] Outstanding Presentation Award → Kungwan Kang, Fumiaki Kato, Ichiro Terasaki, Hyoungjeen Jeen, and Hiromichi Ohta, "Direct measurement of in-plane thermal conductivity for freestanding $Ba_{1/3}CoO_2$ films", The 4th Workshop on Functional Materials Science (FMS2023), Busan, South Korea, June 18-21, 2023.